Ab initio study of electronic surfaces states and plasmons of gold : role of the spin-orbit coupling and surface geometry.

Oleksandr Motornyi

To cite this version:

Oleksandr Motornyi. Ab initio study of electronic surfaces states and plasmons of gold : role of the spin-orbit coupling and surface geometry.. Materials Science [cond-mat.mtrl-sci]. Université Paris Saclay (COmUE), 2018. English. NNT : 2018SACLX116 . tel-03126631

HAL Id: tel-03126631
https://theses.hal.science/tel-03126631

NNT : 2018SACLX116

Ab initio study of electronic surface states and plasmons of gold: role of the spin-orbit coupling and surface geometry.

Thèse de doctorat de l'Université Paris-Saclay
préparée à École Polytechnique

Ecole doctorale n°573 École doctorale INTERFACES (INTERFACES)
Spécialité de doctorat : Physique

Thèse présentée et soutenue à Palaiseau, le 20 Decembre 2018, par

OLEKSANDR MOTORNYI

Composition du Jury :

Mario ROCCA Professeur, Università degli Studi di Genova	Président
Vyacheslav SILKIN Professeur, IKERBASQUE. Basque Foundation for Science	Rapporteur
Hans-Christian WEISSKER Chargé de recherche CNRS, Centre Interdisciplinaire de Nanoscience de Marseille	Rapporteur
Andrea DAL CORSO Professeur associé, Scuola Internazionale Superiore di Studi Avanzati	Examinateur
Alberto ZOBELLI Maître de conférence, Université Paris Sud	Examinateur
Nathalie VAST Chercheuse CEA, École Polytechnique	Directrice de thèse

Thèse de doctorat

Acknowledgements

First and foremost, I would like to thank my advisor, Nathalie Vast for giving me an opportunity to work on this challenging and exciting project, for her guidance, continuous support and motivation. During my PhD project I have learned a great deal about solid state physics and variety of powerful approaches used to solve problems that emerge in modern research. I would like also to thank Michele Raynaud for her guidance during the project, with whom I had many fruitful discussions.

I would like to thank Kees van der Beek, the former director of the Laboratoire des Solides Irradiés of the École Polytechnique, for having welcomed me at LSI. I thank Prof. Vyacheslav Silki and Dr. Hans-Christian Weissker for having accepted to review the manuscript and to participate in the jury of this thesis; Prof. Mario Rocca, for having accepted to chair the jury; Dr. Alberto Zobelli and Dr. Andrea Dal Corso for having accepted to be members of the jury of this thesis. Their feedback on my thesis and our insightful discussions were invaluable.

I am very grateful to my collaborator Andrea Dal Corso, for hospitality at SISSA, for plenty of interesting scientific discussions and help with implementation of new features in the EELS project. His assistance in understanding of electronic band structure of complex surfaces is greatly appreciated. I am also thankful to Stefano Baroni and Iurii Timrov for insightful discussions during my time in Trieste.

I would like to thank all members of the group “Théorie de la Science des Matériaux” including Mariya Romanova, Maksim Markov, Olivier Hardouin Duparc, Gaston Kané, Liang Liang, Zhangxuan Fan, Aminata Doucoure, Amrita Chakraborti, Romuald Bejaud. In particular I am very thankful to Jelena Sjakste with whom I shared the office all these years and to Giulina Barbarino with whom I shared the office during the first year. I am grateful for interesting discussions and their help and support throughout my time in LSI. I would like also to thank our system administrator, Andrea Cucca, for keeping the IT system working well and for his help with all kinds of computer issues as well as Andrea Sartirana for his help with LLR-LSI cluster. I am very grateful to all LSI members who created a great scientific environment at the lab.

I would like to thank my parents for their unending support and love throughout my PhD and my whole life. I am also grateful to my friend Hanna for all her help during last few months of my PhD, Sergei (Telnov), Sergey (Syaber), Andrej and my friends all over the world.

I would like to separately thank my beloved girlfriend, Anastasiia, for her endless love, support and enormous patience during these years.

Finally, I acknowledge the financial support from Université Paris-Saclay.

Résumé

Cette thèse de doctorat est dédiée à l'étude, avec des méthodes de calcul *ab initio*, des plasmons de surface et des états électronique de surface de surfaces d'or, plates ou comportant des marches (surfaces vicinales), par la simulation numérique de spectres de perte d'énergie électronique (EEL) au moyen de la théorie de la fonctionnelle de la densité (DFT) et de la théorie de perturbation de la fonctionnelle de la densité dépendant du temps (TDDFPT). L'influence du couplage spin-orbite (CSO) et celle de la géométrie de la surface ont été étudiées. Dans l'or cristallin, j'ai étudié l'effet des électrons de semicoeur sur les spectres EEL à moment transféré quasi-nul. J'ai montré en particulier que pour produire un spectre EEL sur une large gamme de fréquences, de 0 à 60 eV, il est nécessaire de tenir compte des électrons de semicoeur dans le pseudopotentiel, et qu'ils peuvent néanmoins être gelés dans le coeur pour l'étude de la partie basse en énergie du spectre EEL, pour des énergies inférieures à 15 eV. J'ai réalisé des développements méthodologiques pour la TDDFPT avec CSO couplée à l'emploi de pseudopotentiels ultradoux, qui ont permis l'implémentation pratique de cette approche dans les algorithmes de Liouville-Lanczos et de Sternheimer de Quantum ESPRESSO. J'ai utilisé avec succès ces approches qui m'ont permis de traiter des systèmes à plusieurs centaines d'atomes dans la cellule unitaire. J'ai examiné à nouveau le spectre EEL de l'or cristallin à moment transféré quasi-nul, montrant en particulier les traces d'un plasmon non-écranté $6s$ dans le spectre EEL calculé sans inclure les effets de CSO. J'ai ensuite montré que l'inclusion du CSO a un effet petit mais détectable sur le spectre EEL et le pic de plasmon, donnant un meilleur accord avec des résultats expérimentaux obtenus en utilisant la technique de réflexion EELS à $\mathbf{q} = 0$. Enfin, en utilisant la nouvelle implémentation de l'algorithme de Liouville-Lacnzos avec les pseudopotentiels ultradoux avec CSO, j'ai calculé le spectre EELS pour la surface d'or (111) afin de comprendre l'influence du CSO sur le plasmon de surface acoustique (PAS). Ce type de plasmon a une énergie qui varie linéairement en fonction du moment (dispersion linéaire), d'où le qualificatif d'"acoustique". J'ai trouvé que la dispersion du PAS de Au(111) est légèrement modifiée par le CSO, provenant du fait que la structure de bandes est elle-même modifiée par le dédoublement de Rashba de certains niveaux électroniques de surface, dédoublement induit par le CSO. Puis, pour étudier les effets de géométrie de la surface sur les états de surface électroniques et les plasmons de surface, j'ai étudié les surfaces vicinales (322), (455) et (788) de l'or. J'ai en particulier mené l'étude théorique des états électroniques de surface, et analysé l'évolution de l'état électronique de surface de Shockley entre la surface plate Au(111) et les surfaces ayant des marches dont les terrasses avaient différentes largeurs. J'ai montré la transition d'un état de surface résonant pour Au(322) à un état localisé pour Au(455) et pour Au(788), ainsi que le passage d'un état 2D étendu à travers la marche pour Au(322) à un état quasi-1D confiné dans la terrasse de la marche pour Au(455) et pour Au(788). Ces résultats sont en accord avec des résultats d'expériences de photoémission, et avec ceux d'un modèle de potentiel périodique de Kronig-Penney. J'ai calculé le spectre EELS pour la surface d'or (455) que j'ai modélisée par une tranche de 5 nm d'or séparée de ses voisines (répétées périodiquement) par 5 nm de vide. J'ai identifié la signature du plasmon acoustique de surface. J'ai montré que, pour un moment transféré perpendiculaire à la marche de la surface, la dispersion du PAS n'est pas modifiée par rapport à celle du

PAS de la surface plate Au(111) pour $q < 0.125$ Å^{-1}. Cependant, pour des valeurs plus grandes du moment transféré, le pic du PAS a une énergie plus basse que celle du PAS de Au(111), montrant la signature du confinement du PAS et suggérant que deux types de PAS peuvent se produire: un plasmon intra(sous)bande, similaire à celui de la surface Au(111), et un plasmon inter(sub)band, caractéristique de cette surface vicinale. Enfin, les perspectives de ce travail de thèse sont discutées.

Contents

Introduction

The birth of plasmonics took place at the very beginning of the twentieth century, when Wood [1] observed an unusual phenomenon during the study of light distribution in a diffraction grating spectrum. Lord Rayleigh attempted to explain this phenomenon, however it was not until 1941 when Fano [2] associated the so-called Wood anomalies with surface waves and suggested that they are linked to the dielectric properties of the material. Later on, Pines [3] and Ritchie [4] have developed the theory of plasma oscillations in solids and have suggested that careful investigation of the low energy losses in a single metal should be made. The first experimental evidence of plasma oscillations on an aluminum surface was demonstrated by Powell and Swan [5] a few years later. This phenomenon is called surface plasmon - a collective oscillation of the free electron density similar to plasma oscillations observed in ionized gases [6]. As collective phenomena, plasmons are driven by the Coulomb interaction between electrons in contrast with single-particle excitations that e.g. involve the dipolar transition of a single electron from an occupied to an unoccupied state. After this discovery, surface plasmons have been widely studied and characterized both experimentally and theoretically for various materials and systems. Nowadays, noble metals such as gold and silver are the most used materials for plasmonics applications as they have well defined plasmons and possess other useful properties, for instance gold is very stable and is not easily oxidized.

In order to understand all of the system properties as well as to explain and predict new effects, it is crucial to complement experiments with theory and numerical simulations. Theoretical descriptions of plasmons extend from the classical electrodynamical treatment and simple jellium model to the fully *ab initio* time-dependent density functional theory (TDDFT) approach [7, 8], depending on the needs of each particular problem. For instance, the classical electrodynamical approaches are fairly successful for structures that are larger than 10 nm [9] but start to fail for small-size structures, where quantum effects should be accounted for, like it was done, for instance, for the noble-metal nanoclusters in Ref. [10].

Over a decade ago, a new type of surface plasmons has been theoretically predicted [11] and experimentally reported [12], the so-called acoustic surface plasmon (ASP) that exhibits a behavior different from the behavior of conventional surface plasmon (CSP) and cannot be predicted with the classical electrodynamics. It is believed that the ASP results from the incomplete screening of the 2D electron gas of the Shockley surface state by the underlying 3D bulk electron system, and thus is considered as a modified 2D sheet plasmon. The ASP is a low energy excitation compared to the CSP and has a linear dispersion in contrast to the CSP with a parabolic dispersion. Their low energy may allow the ASP to participate in many dynamical processes involving electrons and phonons. Additionally, due to the sound-like dispersion (hence the name) a signal consisting of several ASP waves can propagate along the surface without distortion. Experimentally, ASP excitations were observed on various surfaces, namely the Be (0001) [12], Au(111) [13], Cu(111) [14, 15] surfaces as well as on the high Miller's index Au(788) surface [16]. The latter case of the vicinal Au(788) surface is of special interest from the viewpoint of applications, as the step-terrace structure of the surface provides the intrinsic grating of the surface on the atomic level allowing, potentially, to couple the ASP to the light. Theoretical models have been proposed to explain the origin and the behavior of ASPs in metals that support Shockley states [17] [18], however there are still some discrepancies and controversies between the model, experiment and *ab initio* calculations, as, for example, a simplified model used in Ref. [16] cannot fully reproduce the experimental ASP dispersion of Au(788) and it was suggested that fully *ab initio* study is required.

From the viewpoint of *ab initio* calculations, calculations of big periodic systems like high Miller's index surfaces are a very challenging or even unfeasible computational task for the traditional TDDFT methods that involve solving a Dyson-like equation [19, 20], and thus alternative approaches are required. In my thesis I use the recently developed time-dependent density functional perturbation theory (TDDFPT) Liouville-Lanczos approach [21, 22, 23, 24, 25, 26], that allow to significantly reduce the CPU time and memory required for the calculations. Using this method I can compute the electron energy-loss (EEL) spectra for an arbitrary transferred momentum $\mathbf{q}$ that can be compared to the results of EEL spectroscopy or inelastic X-Ray scattering (IXS) experiments. In the last Chapter I will show the results of TDDFPT simulations of 5 nm of gold separated by 5 nm of vacuum. Thus, I demonstrate that the computation of plasmonic properties on the quantum level at the linear order is within reach and can become a routine task in a near future.

One of the goals of my thesis was to make a further development and implementation of the Liouville-Lanczos approach that would allow to use full relativistic ultrasoft pseudopotentials in order to reduce even more the computational cost of the calculations. The next objective of the thesis was to use the newly implemented method in order to study the influence of the spin-orbit coupling (SOC) on the EEL spectra of the bulk and of the (111) surface of gold and specifically to study the influence of SOC on the ASP of the Au(111) surface. During the second year of my PhD the collaboration with Andrea Dal Corso from the Scuola Internazionale Superiore di Studi Avanzati (SISSA) of Trieste (Italy) has been established and I have taken benefit from three visits to SISSA financed in part by the MAX EU project from SISSA, from the Ecole Doctorale Interfaces of University Paris-Saclay and from my supervisor's contracts. The goal of the project was the methodological development and implementation of the Liouville-Lanczos algorithm for the full relativistic ultrasoft pseudopotentials.

The second major goal of the thesis was to perform an *ab initio* study of the three vicinal surfaces of Au(111): Au(332), Au(455) and Au(788). This study was twofold: the first part was aimed at understanding the behavior and evolution of the Shockley state of the Au(111) surface depending on the surface geometry. The second one, was to study the behavior of the ASP in one of these systems, in order to understand how the surface geometry might influence the properties of the ASP and, in perspective, to better understand the experiments on the Au(788) surface. As discussed in Chapter 8, the Au(322) surface was discarded from the possible numerical applications because the Shockley state, which is believed to give rise to the ASP excitation, is a linear combination of the 2D state and 3D bulk states (hence it is classified as a surface resonance) and is not expected to be observable as a distinct peak in the calculated EEL spectrum. Thus, the focus of the study was shifted to the ASP of the Au(455) surface.

In this work, calculations in a high performance computing (HPC) environment have been performed. Approximately 5 millions hours of CPU time have been spent in total. In particular, I have spent about 2 millions hours of CPU time in the Grand Équipement National de Calcul Intensif (GENCI): GENCI-CINES, GENCI-TGCC and GENCI-IDRIS (project 2210), 2 millions in the framework of the PRACE project (project number 2017174202) in the Jülich Supercomputing Centre (JSC) and about 1 million hours on the local LSI-LLR cluster.

thesis is organized in two part. In the first part I present the state-of-the-art methods and give a brief overview of the results of existing theoretical and experimental studies on EEL spectra and plasmons of gold. In the second part I present my results which consist of the theoretical, numerical and methodological developments and of a detailed study of surface states and plasmons of high Miller's index surfaces of gold.

The part I contains 3 chapters.

In Chapter 1 I will give an introduction to the linear response approach and TDDFPT used to solve the linear response problem. In particular I will focus on two approaches: the self-consistent Sternheimer approach and the recursive Liouville-Lanczos approach that are then compared and generalized to the full relativistic ultrasoft pseudopotential scheme in Chapter 4.

In Chapter 2 I will give a definition of surface states and resonances and will give an overview of the geometry of flat and vicinal surfaces of gold. I will then discuss shortly the results of some experimental works where these surfaces were studied using ARPES revealing that the Shockley state becomes confined in Au(788) and Au (23 23 21) surfaces. Later in the Chapter 5 I will compare the results of my *ab initio* calculations to these experiments.

In Chapter 3 I will give an introduction to plasmons with a specific focus on conventional and acoustic surface plasmons of noble metals. I will discuss results of some theoretical works where EEL spectra of Au have been studied using TDDFPT and I will point out the limitations of the most common exchange and correlation kernel approximations used in DFT. Finally I will discuss the ASP of noble metal surfaces and some controversies between different experimental and theoretical works.

The part II contains 5 chapters.

In Chapter 4 I will present the methodological developments aimed at the generalization to the full relativistic ultrasoft pseudopotential scheme of the Sternheimer and Liouville-Lanczos approaches presented in Chapter 1. I will show some results on the comparison of the performance of these two approaches and the results of benchmarking of the Liouville-Lanczos approach performance in the HPC environment.

In Chapter 5 I will present the results of the *ab initio* study of the surface states on vicinal Au(322), Au(455) and Au(788) surfaces. I will discuss how the refolding of the band structure of such surfaces significantly complicates the analysis of the DFT calculations and show that nevertheless valuable information about surface states can be obtained. I will show how the Shockley state evolve depending on the surface geometry and compare my results to the previous experimental data.

In Chapter 6 I will present the results of EEL spectrum calculations for bulk Au and discuss the magnitude of the spin-orbit coupling effect both for vanishing and finite transferred momentum. I will show how the inclusion of spin-orbit coupling brings the calculated EEL spectrum for vanishing momentum into better agreement with experiments and show how the effect of the spin-orbit coupling on the EEL spectra fade out for bigger momentum values.

In the Chapter 7 I will discuss the effect of spin-orbit coupling on the EEL spectrum and the ASP of the Au(111) surface. I show how the EEL spectrum of Au(111) is very similar to the EEL spectrum of bulk Au. I will also discuss the influence of SOC on the ASP dispersion of the Au(111) surface, showing that it is small but noticeable, and that there must be other factors that contribute to the discrepancies between the experimental and theoretical results.

In Chapter 8 I will discuss the EEL spectrum and the ASP of the Au(455) surface simulated as a gold slab with a thickness of 5 nm. I will show that the overall EEL spectrum of the Au(455) surface is modified for a vanishing transferred momentum compared to the spectrum of Au(111). I will also discuss the dispersion of the ASP of the Au(455) surface and compare it to that of the Au(111) surface, as well as to the experimental results on Au(788) from a qualitative viewpoint.

Finally, I will draw general conclusions and perspectives.

Part I

State of the art

Chapter 1

Time dependent density functional theory (TDDFT) for the calculation of dielectric properties of solids

This chapter aimed at providing an overview of the time dependent density functional theory (TDDFT) problem and its link to material properties that can be measured experimentally. The main goal of this chapter is to provide a starting point and outline the current state of the art for the methodological development presented in Chapter 4. First I discuss TDDFT within the linear response framework, the showing key equations and defining the main quantities. Then I will define the dielectric function and its link to the quantities measured in electron energy loss spectroscopy (EELS) experiments. Finally I will point out the advantages, drawbacks and limitations of the time dependent density functional perturbation theory (TDDFPT) through the Liouville-Lanczos and Sternheimer aprroaches. Finally, I will discuss possible improvements that can be done in future, some of which I discuss in the Chapter 4.

1.1 Linear response approach and dielectric function

1.1.1 Linear response theory

In the general case, the susceptibility of a system is defined through the first-order response of an observable $\hat{\mathcal{A}}$ to a time-dependent external field $f_{ext}(t)$:

$$\delta\mathcal{A}(t) = \int_{t_0}^{t} dt'\chi(t-t')f_{ext}(t'), \tag{1.1}$$

where $f_{ext}(t) = 0$ for $t < t_0$. In the linear response framework relevant to this work we assume that the external perturbation takes the form of a weak time-dependent potential:

$$V_{ext}(\mathbf{r},t) = V^0_{ext}(\mathbf{r}) + V'_{ext}(\mathbf{r},t), \tag{1.2}$$

where $V^0_{ext}(\mathbf{r})$ is the static external potential of the unperturbed system and $V'_{ext}(\mathbf{r},t)$ is the time-dependent perturbation. The density of the perturbed system in the linear response regime is given by

$$n(\mathbf{r},t) = n^0(\mathbf{r}) + n'(\mathbf{r},t), \tag{1.3}$$

where $n^0(\mathbf{r})$ is the density of the unperturbed system and $n'(\mathbf{r},t)$ is the first order density response of the system, that reads [20]:

$$n'(\mathbf{r},t) = \int_{-\infty}^{\infty} dt' \int d\mathbf{r}' \chi(\mathbf{r},\mathbf{r}',t-t') V'_{ext}(\mathbf{r}',t'). \tag{1.4}$$

where χ is the linear density response function defined as:

$$\chi(\mathbf{r},\mathbf{r}',t-t') = \left.\frac{\delta n(\mathbf{r},t)}{\delta V_{ext}(\mathbf{r}',t')}\right|_{V_{ext}(\mathbf{r}',t')=V^0_{ext}(\mathbf{r}')}. \tag{1.5}$$

One possible way to obtain the susceptibility of the system is to solve the Dyson-like screening equation [19]. However, I am not using this approach in my work and thus will not discuss it in the present chapter.

1.1.2 Dielectric function

A system under a weak external perturbation $V_{ext}(\mathbf{r},t)$ will be polarized and the total potential will be the sum of the external and induced potentials $V_{tot} = V_{ext} + V_{ind}$. At the linear response level we can define the microscopic dielectric function that relates the total potential V_{tot} to the applied potential V_{ext} as:

$$V_{tot}(\mathbf{r},t) = \int_{-\infty}^{\infty} dt' \int d\mathbf{r}'\, \epsilon^{-1}(\mathbf{r},\mathbf{r}',t-t')\, V_{ext}(\mathbf{r}',t'). \tag{1.6}$$

Let us Fourier-transform Eq. (1.4) and (1.6) to pass from the time- to frequency-domain:

$$n'(\mathbf{r},\omega) = \int d\mathbf{r}' \chi(\mathbf{r},\mathbf{r}',\omega) V'_{ext}(\mathbf{r}',\omega). \tag{1.7}$$

$$V_{tot}(\mathbf{r},\omega) = \int d\mathbf{r}'\, \epsilon^{-1}(\mathbf{r},\mathbf{r}',\omega)\, V_{ext}(\mathbf{r}',\omega). \tag{1.8}$$

Alternatively, we can write the total potential $V_{tot}(\mathbf{r},\omega)$ as:

$$V_{tot}(\mathbf{r},\omega) = V_{ext}(\mathbf{r},\omega) + \int d\mathbf{r}'\, \frac{e^2 n'(\mathbf{r},\omega)}{|\mathbf{r}-\mathbf{r}'|}, \tag{1.9}$$

where e is the electron charge. Together, Eqs. (1.7), (1.8) and (1.9) result in the following expression for the microscopic dielectric function:

$$\epsilon^{-1}(\mathbf{r},\mathbf{r}',\omega) = \delta(\mathbf{r}-\mathbf{r}') + e^2 \int d\mathbf{r}''\, \frac{\chi(\mathbf{r}'',\mathbf{r}',\omega)}{|\mathbf{r}-\mathbf{r}'|}. \tag{1.10}$$

For a periodic system one can also perform a Fourier transform from the real to the reciprocal space obtaining:

$$\epsilon^{-1}_{\mathbf{G},\mathbf{G}'}(\mathbf{q},\omega) = \delta_{\mathbf{G},\mathbf{G}'} + v_{\mathbf{G}}(\mathbf{q})\, \chi_{\mathbf{G},\mathbf{G}'}(\mathbf{q},\omega), \tag{1.11}$$

where $v_{\mathbf{G}}(\mathbf{q}) = 4\pi e^2/|\mathbf{q}+\mathbf{G}|^2$ is the Fourier transform of the Coulomb potential $e^2/|\mathbf{r}-\mathbf{r}'|$. Finally, the macroscopic dielectric function is defined for $\mathbf{G} = \mathbf{G}' = 0$ as:

$$\epsilon_{\mathrm{M}}(\mathbf{q},\omega) = \left[\frac{1}{\epsilon^{-1}_{\mathbf{G},\mathbf{G}}(\mathbf{q},\omega)}\right]_{\mathbf{G},\mathbf{G}'=0}, \tag{1.12}$$

where the wavevector $\mathbf{q}$ belongs to the first Brillouin zone. $\epsilon_{\mathrm{M}}(\mathbf{q},\omega)$ is a measurable quantity that can be related to different spectroscopies. Optical absorption or electron energy loss (EEL) spectrum at vanishing transferred momentum yield the macroscopic dielectric function or the loss function at $\mathbf{q} = \mathbf{0}$. EEL at finite momentum transfer or inelastic X-ray scattering (IXS) spectroscopy probes the loss function or the dynamical structure factor at finite $\mathbf{q}$. EELS is of specific interest for my work, as I compute EEL spectra and compare to some of the experimental results. In an EELS experiment, the inelastic scattering probability of an incoming electron by the electrons of the solid, given by the double-differential cross-section $d^2\sigma/(d\omega d\Omega)$ is measured, which is linked to the macroscopic dielectric function ϵ_M defined above:

$$\frac{d^2\sigma}{d\omega d\Omega} \sim Im[\frac{1}{\epsilon_M(\mathbf{q},\omega)}], \tag{1.13}$$

where $\mathbf{q}$ is the transferred momentum, ω is the measured electron energy loss, and $d\Omega$ is the elemental solid-angle in which the scattering occurs.

1.2 Time dependent density functional perturbation theory (TDDFPT) equations

In this section I present the framework of TDDFPT equations to solve the linear response problem. As I have mentioned in a previous section, one way to obtain a susceptibility χ (or a dielectric function ϵ) is to solve a Dyson-like screening equation. While this method is powerful and well established, in my work I have been using an alternative approach that comes from the density functional perturbation theory (DFPT) [27] and a Lanczos recursive algorithm that, together, allow to significantly reduce the computational cost of the calculation, and thus enables to compute the dielectric properties of very large systems that consist of hundreds of atoms.

1.2.1 The Sternheimer equations

The time-dependent Kohn-Sham equation [28] for an auxilary fictious system of non-interacting particles in the scalar relativistic (without spin-orbit coupling) case reads:

$$i\hbar\frac{\partial\psi_{n,\mathbf{k}}(\mathbf{r},t)}{\partial t} = \hat{H}_{KS}(\mathbf{r},t)\psi_{n,\mathbf{k}}(\mathbf{r},t), \tag{1.14}$$

where $\psi_{n,\mathbf{k}}(\mathbf{r},t)$ and $\hat{H}_{KS}(\mathbf{r},t)$ are the time-dependent Kohn-Sham wavefunction and Hamiltonian respectively. The density of such a system reads:

$$n(\mathbf{r},t) = \sum_{n}^{N} |\psi_n(\mathbf{r},t)|^2, \tag{1.15}$$

where N is the number of occupied states in insulators or semiconductors.[1]

In the linear response framework the external perturbation action on the system is assumed to be weak and thus can be given in the form of Eq. (1.2). In this case the Hamiltonian of Eq. (1.14) reads:

$$\hat{H}_{KS}(\mathbf{r},t) = \hat{H}^0(\mathbf{r}) + V'(\mathbf{r},t), \tag{1.16}$$

where $\hat{H}^0(\mathbf{r})$ is the Hamiltonian of the unperturbed system that, in the Kohn-Sham approach, reads:

$$\hat{H}^0(\mathbf{r}) = -\frac{\hbar^2}{2m_0}\nabla^2 + V^0_{ext}(\mathbf{r}) + V^0_{H\mathrm{xc}}(\mathbf{r}), \tag{1.17}$$

and the linearized self-consistent Kohn-Sham perturbation reads:

$$V'(\mathbf{r},t) = V'_{ext}(\mathbf{r},t) + V'_{H\mathrm{xc}}(\mathbf{r},t), \tag{1.18}$$

where $V'_{ext}(\mathbf{r},t)$ is the external time-dependent perturbation and $V'_{H\mathrm{xc}}(\mathbf{r},t)$ is the time-dependent Hartree-plus-XC potential induced due to the external perturbing potential $V'_{ext}(\mathbf{r},t)$.

The density of the perturbed system in the linear response regime is given by Eq. (1.3).

Finally, the Kohn-Sham wavefunctions in Eq. (1.14) $\psi_{n,\mathbf{k}}(\mathbf{r},t)$ can be decomposed into:

$$\psi_{n,\mathbf{k}}(\mathbf{r},t) = e^{-i\varepsilon_{n,\mathbf{k}}t/\hbar}\left[\psi^0_{n,\mathbf{k}}(\mathbf{r}) + \psi^{'}_{n,\mathbf{k}}(\mathbf{r},t)\right], \tag{1.19}$$

where $\psi^0_{n,\mathbf{k}}(\mathbf{r})$ and $\varepsilon_{n,\mathbf{k}}$ are the KS wavefunctions and energy of the unperturbed system and $\psi^{'}_{n,\mathbf{k}}(\mathbf{r},t)$ is its first order variation, or response wavefunction.

Equation (1.14) and its complex conjugate can be linearized taking into account only the first-order response and using the fact that due to the time-reversal symmetry $\hat{H}^{0*} = \hat{H}^0$, $V'^*_{ext}(\mathbf{r},t) = V'_{ext}(\mathbf{r},t)$, $V'^*_{Hxc}(\mathbf{r},t) = V^{'}_{Hxc}(\mathbf{r},t)$, $\psi^{0*}_{n,-\mathbf{k}} = \psi^0_{n,\mathbf{k}}$ and $\varepsilon^*_n = \varepsilon_n$:

$$i\hbar\frac{\partial\psi^{'}_{n,\mathbf{k}}(\mathbf{r},t)}{\partial t} = (\hat{H}^0 - \varepsilon^0_{n,\mathbf{k}})\psi^{'}_{n,\mathbf{k}}(\mathbf{r},t) + (V^{'}_{Hxc}(\mathbf{r},t) + (V^{'}_{ext}(\mathbf{r},t))\psi^0_{n,\mathbf{k}}(\mathbf{r}), \tag{1.20}$$

$$-i\hbar\frac{\partial\psi'^*_{n,\mathbf{k}}(\mathbf{r},t)}{\partial t} = (\hat{H}^0 - \varepsilon^0_{n,\mathbf{k}})\psi'^*_{n,\mathbf{k}}(\mathbf{r},t) + (V^{'}_{Hxc}(\mathbf{r},t) + (V^{'}_{ext}(\mathbf{r},t))\psi^{0*}_{n,\mathbf{k}}(\mathbf{r}), \tag{1.21}$$

Finally using the Fourier transformation and applying a projector onto the empty states $\hat{P}_c = 1 - \hat{P}_v$ where c stands for conduction band state and v stands for the valence band states, we obtain:

$$(\hat{H}^0 - \varepsilon^0_{n,\mathbf{k}} - \hbar\omega)\hat{P}_c\psi^{'}_{n,\mathbf{k}}(\mathbf{r},\omega) + \hat{P}_c V^{'}_{Hxc}(\mathbf{r},\omega)\psi^0_{n,\mathbf{k}}(\mathbf{r}) = -\hat{P}_c V^{'}_{ext}(\mathbf{r},\omega)\psi^0_{n,\mathbf{k}}(\mathbf{r}), \tag{1.22}$$

$$(\hat{H}^0 - \varepsilon^0_{n,-\mathbf{k}} + \hbar\omega)\hat{P}_c\psi'^*_{n,\mathbf{k}}(\mathbf{r},-\omega) + \hat{P}_c V'^*_{Hxc}(\mathbf{r},-\omega)\psi^0_{n,\mathbf{k}}(\mathbf{r}) = -\hat{P}_c V'^*_{ext}(\mathbf{r},-\omega)\psi^0_{n,\mathbf{k}}(\mathbf{r}), \tag{1.23}$$

where n now spans only the occupied state manifold.

---

[1] In a metal Eq.(1.15) reads $n(\mathbf{r},t) = \sum_n^N f_n|\psi_n(\mathbf{r},t)|^2$, where f_n is the equilibrium Fermi-Dirac electronic occupations.

Finally, using the wavefunctions in the form of Eq. (1.19) in (1.15) and its Fourier transformation one can obtain the first order density response $n'(\mathbf{r},\omega)$:

$$n'(\mathbf{r},\omega) = \sum_{\mathbf{k}}^{BZ}\sum_{n} \psi^{0*}_{n,\mathbf{k}}(\mathbf{r}) \left[\psi'^{*}_{n,\mathbf{k}}(\mathbf{r},-\omega) + \psi'_{n,\mathbf{k}}(\mathbf{r},\omega)\right] \tag{1.24}$$

The set of equations (1.22), (1.23) and the corresponding charge density response (1.24) is called the Sternheimer equations. This system can be solved self-consistently for each value of the frequency ω allowing to obtain the susceptibility χ of the system and thus the dielectric function of the system. I note that the use of a projector onto empty states $\hat{P}_c$ allows to avoid the calculation of the empty states [27] that is necessary in other approaches and thus enables the computation for systems with a large number of atoms.

1.2.2 The quantum Liouville equation

Equivalently, instead of Eq. (1.14) as a starting point, one can use the quantum Liouville equation [21, 22, 23, 24, 25, 26]:

$$i\hbar\frac{d\hat{\rho}(t)}{dt} = \left[\hat{H}_{KS}(t), \hat{\rho}(t)\right], \tag{1.25}$$

where $\hat{\rho}(t)$ is the reduced one-electron KS density-matrix whose kernel reads:

$$\rho(\mathbf{r},\mathbf{r}',t) = \sum \psi_v(\mathbf{r},t)\psi^*_v(\mathbf{r}',t), \tag{1.26}$$

where v runs over valence states and $n(\mathbf{r},t) = \rho(\mathbf{r},\mathbf{r},t)$. Equation (1.25) can be linearized in the same manner as eq. (1.14), leading to the linearized Liouvillian equation that is equivalent to the set of Sternheimer's equations (1.22), (1.23):

$$(\hbar\omega - \hat{\mathcal{L}}) \cdot \hat{\rho}'(\omega) = \left[\tilde{V}'_{ext}(\omega), \hat{\rho}^0\right]. \tag{1.27}$$

The action of the Liouvillian superoperator $\hat{\mathcal{L}}$ onto $\hat{\rho}$ is defined as:

$$\hat{\mathcal{L}} \cdot \hat{\rho}' = \left[\hat{H}^0, \hat{\rho}'\right] + \left[V'_{Hxc}[\hat{\rho}'], \hat{\rho}^0\right]. \tag{1.28}$$

Here $\hat{\rho}'(\mathbf{r},\omega) = \hat{\rho}(\mathbf{r},\omega) - \hat{\rho}^0(\mathbf{r})$ is the response density matrix and $\hat{\rho}^0(\mathbf{r})$ is the unperturbed density matrix, whereas V'_{Hxc} in (1.28) is:

$$V'_{H\mathrm{xc}}(\mathbf{r},\omega) = \int K_{H_{xc}}(\mathbf{r},\mathbf{r}')\, n'(\mathbf{r}',\omega)\, d\mathbf{r}', \tag{1.29}$$

where $K_{H_{xc}}(\mathbf{r},\mathbf{r}')$ is the sum of the Hartree and exchange and correlation kernels (Hartree-plus+XC kernel):

$$\kappa(\mathbf{r},\mathbf{r}') = \frac{e^2}{|\mathbf{r}-\mathbf{r}'|} + f_{\mathrm{xc}}(\mathbf{r},\mathbf{r}'), \tag{1.30}$$

and f_{xc} is the exchange-correlation kernel. Equation (1.27) can be solved using the Lanczos recursive scheme [21, 22, 23, 24, 25, 26] for all of the frequencies at once, resulting in the susceptibility χ.

1.2.3 TDDFPT in extended systems

So far, I have not specified the perturbation that acts on the system neither I used the fact that we are dealing with periodic systems. In an EELS experiment the weak external perturbation is one free electrons that can be described as a plane wave $e^{i(\mathbf{q}\cdot\mathbf{r}-\omega t)}$. The perturbing potential can be written as:

$$V'_{ext}(\mathbf{r},t) = \int\limits_{-\infty}^{\infty} \tilde{V}'_{ext}(\mathbf{r},\omega)\, e^{-i\omega t}\, d\omega = \int\limits_{0}^{\infty} \left[\tilde{V}'_{ext}(\mathbf{r},\omega)\, e^{-i\omega t} + c.c.\right] d\omega, \tag{1.31}$$

where $\tilde{V}'_{ext}(\mathbf{r},\omega)$ can be further decomposed into Fourier monochromatic $\mathbf{q}$ components:

$$\tilde{V}'_{ext}(\mathbf{r},\omega) = \sum_{\mathbf{q}}^{1\mathrm{BZ}} e^{i\mathbf{q}\cdot\mathbf{r}}\, \tilde{v}_{ext,\mathbf{q}}(\mathbf{r},\omega), \qquad \tilde{v}_{ext,\mathbf{q}}(\mathbf{r}+\mathbf{R},\omega) = \tilde{v}_{ext,\mathbf{q}}(\mathbf{r},\omega), \tag{1.32}$$

where $\tilde{v}_{ext,\mathbf{q}}(\mathbf{r},\omega) = 1$ in the case of free electrons, and $\mathbf{R}$ is the radius-vector of the primitive unit cell. The same decomposition can be done for the Hartree-plus-XC response potential in Eq. (1.18), yielding:

$$\tilde{V}'(\mathbf{r},\omega) = \sum_{\mathbf{q}}^{\mathrm{BZ}} e^{i\mathbf{q}\cdot\mathbf{r}}\, \tilde{v}_{\mathbf{q}}(\mathbf{r},\omega), \qquad \tilde{v}_{\mathbf{q}}(\mathbf{r},\omega) = \tilde{v}_{ext,\mathbf{q}}(\mathbf{r},\omega) + \tilde{v}_{H\mathrm{xc},\mathbf{q}}(\mathbf{r},\omega). \tag{1.33}$$

where $\tilde{v}_{H\mathrm{xc},\mathbf{q}}(\mathbf{r},\omega)$ is a lattice-periodic function.

According to the Bloch theorem, in a periodic system, the ground state Kohn-Sham wavefunction can be written as:

$$\psi^0_{n,\mathbf{k}}(\mathbf{r}) = e^{i\mathbf{k}\cdot\mathbf{r}}\, u^0_{n,\mathbf{k}}(\mathbf{r}), \qquad u^0_{n,\mathbf{k}}(\mathbf{r}+\mathbf{R}) = u^0_{n,\mathbf{k}}(\mathbf{r}), \tag{1.34}$$

where $u^0_{n,\mathbf{k}}(\mathbf{r})$ is the lattice periodic function. Let us now define the projector onto empty states in periodic systems:

$$\hat{P}_c = \sum_{n,\mathbf{k}}^{unocc} \psi^0_{n,\mathbf{k}}(\mathbf{r})\, \psi^{0\,*}_{n,\mathbf{k}}(\mathbf{r}') = \sum_{\mathbf{k}} e^{i\mathbf{k}\cdot\mathbf{r}}\, P^{\mathbf{k}}_c\, e^{-i\mathbf{k}\cdot\mathbf{r}'}, \tag{1.35}$$

where the summation runs over unoccupied states n, and $P^{\mathbf{k}'}_c$ is the projector onto empty states at point $\mathbf{k}$, which reads:

$$\hat{P}^{\mathbf{k}}_c = \sum_{n}^{unocc} u^0_{n',\mathbf{k}}(\mathbf{r})\, u^{0\,*}_{n,\mathbf{k}}(\mathbf{r}') = 1 - \sum_{n}^{occ} u^0_{n,\mathbf{k}}(\mathbf{r})\, u^{0\,*}_{n,\mathbf{k}}(\mathbf{r}'). \tag{1.36}$$

Finally, we can define the unperturbed Hamiltonian $\hat{H}^0_{\mathbf{k}}$ as:

$$\hat{H}^0_{\mathbf{k}} = e^{-i(\mathbf{k})\cdot\mathbf{r}}\, \hat{H}^0\, e^{i(\mathbf{k})\cdot\mathbf{r}}. \tag{1.37}$$

1.2.3.a The Sterheimer equations

Now we can write the Sternheimer equations (1.22), (1.23) only for the lattice-periodic part of the response wavefunctions and potential[2]:

$$(\hat{H}^0_{\mathbf{k}+\mathbf{q}} - \varepsilon_{n,\mathbf{k}} - \hbar\omega)\hat{P}_c^{\mathbf{k}+\mathbf{q}} u'_{n,\mathbf{k}+\mathbf{q}}(\mathbf{r},\omega) + \hat{P}_c^{\mathbf{k}+\mathbf{q}}\, v'_{H\mathrm{xc},\mathbf{q}}(\mathbf{r},\omega)\, u^0_{n,\mathbf{k}}(\mathbf{r}) = -\hat{P}_c^{\mathbf{k}+\mathbf{q}}\, \tilde{v}'_{ext,\mathbf{q}}(\mathbf{r},\omega)\, u^0_{n,\mathbf{k}}(\mathbf{r}), \tag{1.38}$$

$$(\hat{H}^0_{\mathbf{k}+\mathbf{q}} - \varepsilon_{n,\mathbf{k}} + \hbar\omega)\hat{P}_c^{\mathbf{k}+\mathbf{q}} u'^{*}_{n,-\mathbf{k}-\mathbf{q}}(\mathbf{r},-\omega) + \hat{P}_c^{\mathbf{k}+\mathbf{q}}\, \tilde{v}'_{H\mathrm{xc},\mathbf{q}}(\mathbf{r},\omega)\, u^0_{n,\mathbf{k}}(\mathbf{r}) = -\hat{P}_c^{\mathbf{k}+\mathbf{q}}\, \tilde{v}'_{ext,\mathbf{q}}(\mathbf{r},\omega)\, u^0_{n,\mathbf{k}}(\mathbf{r}). \tag{1.39}$$

where $u'_{n,\mathbf{k}+\mathbf{q}}(\mathbf{r},\omega)$ and $u'^{*}_{n,-\mathbf{k}-\mathbf{q}}(\mathbf{r},-\omega)$ are lattice periodic components of response wavefunctions $\psi'^{*}_{n,-\mathbf{k}}(\mathbf{r},-\omega)$ and $\psi'_{n,\mathbf{k}}(\mathbf{r},\omega)$. I have used the fact that due to the time-reversal symmetry the following relations hold for unperturbed wavefunctions $u^{0\,*}_{n,-\mathbf{k}}(\mathbf{r}) = u^0_{n,\mathbf{k}}(\mathbf{r})$ and for the potential $\tilde{v}'^{*}_{-\mathbf{q}}(\mathbf{r},-\omega) = \tilde{v}'_{\mathbf{q}}(\mathbf{r},\omega)$.

Finally, the response charge-density can also be decomposed into monochromatic $\mathbf{q}$ components:

$$n'(\mathbf{r},\omega) = \sum_{\mathbf{q}} e^{i\mathbf{q}\cdot\mathbf{r}}\, n'_{\mathbf{q}}(\mathbf{r},\omega), \tag{1.40}$$

where $n'_{\mathbf{q}}(\mathbf{r},\omega)$ is the lattice-periodic part which reads:

$$n'_{\mathbf{q}}(\mathbf{r},\omega) = 2\sum_{n,\mathbf{k}} u^{0\,*}_{n,\mathbf{k}}(\mathbf{r}) \left[\tilde{u}'_{n,\mathbf{k}+\mathbf{q}}(\mathbf{r},\omega) + \tilde{u}'^{*}_{n,-\mathbf{k}-\mathbf{q}}(\mathbf{r},-\omega)\right]. \tag{1.41}$$

1.2.3.b The quantum Liouville equation

Alternatively Sternheimer equations (1.38) and (1.39) can be rewritten into the quantum Liouville equation:

$$(\hbar\omega\hat{I} - \hat{\mathcal{L}}_{\mathbf{q}}) \cdot \hat{\rho}'_{\mathbf{q}}(\mathbf{r},\omega) = [\tilde{v}'_{ext,\mathbf{q}}(\mathbf{r},\omega), \hat{\rho}^0(\mathbf{r})], \tag{1.42}$$

with the response density matrix:

$$\rho'_{\mathbf{q}}(\mathbf{r},\mathbf{r}';\omega) = 2\sum_{n,\mathbf{k}} \left[u'_{n,\mathbf{k}+\mathbf{q}}(\mathbf{r},\omega)\, u^{0\,*}_{n,\mathbf{k}}(\mathbf{r}') + u'^{*}_{n,-\mathbf{k}-\mathbf{q}}(\mathbf{r}',-\omega)\, u^{0\,*}_{n,\mathbf{k}}(\mathbf{r})\right]. \tag{1.43}$$

I note that the susceptibility $\chi(\mathbf{q},\omega)$ in this formalism is given by:

$$\chi(\mathbf{q},\omega) = \left\langle \tilde{v}'_{ext,\mathbf{q}}(\mathbf{r},\omega) \middle| (\hbar\omega - \hat{\mathcal{L}})^{-1} \cdot [\tilde{v}'_{ext,\mathbf{q}}(\mathbf{r},\omega), \hat{\rho}^0(\mathbf{r})] \right\rangle. \tag{1.44}$$

It can be efficiently calculated using the Lanczos recursive scheme [24, 26].

1.2.4 Batch representation of TDDFPT equations

The response density (1.41) at any given frequency ω is determined by the two following sets of response orbitals also called batches [21, 24]:

$$\mathbf{x} = \{u'_{n,\mathbf{k}+\mathbf{q}}(\mathbf{r},\omega)\}, \tag{1.45}$$

---

[2] For notational convenience I have changed $\mathbf{k}$ to $-\mathbf{k}$ in the second equation

$$\mathbf{y} = \{u'^{*}_{n,-\mathbf{k}-\mathbf{q}}(\mathbf{r}, -\omega)\}. \tag{1.46}$$

It is convenient (in non-magentic systems [29] where the off-diagonal elements of the spin-polarized density matrix are zero) to perform a 45° rotation in the space of batches to pass to standard batch representation (SBR) defining $\mathbf{q} = \{q_{n,\mathbf{k}+\mathbf{q}}(\mathbf{r})\}$ and $\mathbf{p} = \{p_{n,\mathbf{k}+\mathbf{q}}(\mathbf{r})\}$, where

$$q_{n,\mathbf{k}+\mathbf{q}}(\mathbf{r}) = \frac{1}{2}\,[u'_{n,\mathbf{k}+\mathbf{q}}(\mathbf{r}, \omega) + u'^{*}_{n,-\mathbf{k}-\mathbf{q}}(\mathbf{r}, -\omega)], \tag{1.47}$$

$$p_{n,\mathbf{k}+\mathbf{q}}(\mathbf{r}) = \frac{1}{2}\,[u'_{n,\mathbf{k}+\mathbf{q}}(\mathbf{r}, \omega) - u'^{*}_{n,-\mathbf{k}-\mathbf{q}}(\mathbf{r}, -\omega)]. \tag{1.48}$$

In the SBR, the lattice-periodic monochromatic $\mathbf{q}$ component of the response charge-density reads [see Eq. (1.41)]:

$$n'_{\mathbf{q}}(\mathbf{r}, \omega) = 4\sum_{n,\mathbf{k}} u^{0\,*}_{n,\mathbf{k}}(\mathbf{r})\, q_{n,\mathbf{k}+\mathbf{q}}(\mathbf{r}). \tag{1.49}$$

In the SBR, the quantum Liouville equation (1.27), or equivalently the Sterheimer equations (1.22) and (1.23), can be written in the matrix form:

$$\begin{pmatrix} \hbar\omega & -\hat{\mathcal{D}}_{\mathbf{q}} \\ -\hat{\mathcal{D}}_{\mathbf{q}} - 2\hat{\mathcal{K}}_{\mathbf{q}} & \hbar\omega \end{pmatrix} \begin{pmatrix} \mathbf{q} \\ \mathbf{p} \end{pmatrix} = \begin{pmatrix} 0 \\ \{\hat{P}_c^{\mathbf{k}+\mathbf{q}}\, \tilde{v}'_{ext,\mathbf{q}}(\mathbf{r}, \omega)\, u^0_{n,\mathbf{k}}(\mathbf{r})\} \end{pmatrix}, \tag{1.50}$$

where the action of the $\hat{\mathcal{D}}_{\mathbf{q}}$ and $\hat{\mathcal{K}}_{\mathbf{q}}$ superoperators on the batches of orbitals is defined as:

$$\hat{\mathcal{D}}_{\mathbf{q}} \cdot q_{n,\mathbf{k}+\mathbf{q}}(\mathbf{r}) = (\hat{H}^0_{\mathbf{k}+\mathbf{q}} - \varepsilon_{n,\mathbf{k}})\, q_{n,\mathbf{k}+\mathbf{q}}(\mathbf{r}), \tag{1.51}$$

and

$$\hat{\mathcal{K}}_{\mathbf{q}} \cdot q_{n,\mathbf{k}+\mathbf{q}}(\mathbf{r}) = 2\hat{P}_c^{\mathbf{k}+\mathbf{q}} \sum_{n',\mathbf{k}'} \int K_{n\mathbf{k};n'\mathbf{k}'}(\mathbf{r}, \mathbf{r}')\, q_{n',\mathbf{k}'+\mathbf{q}}(\mathbf{r}')\, d\mathbf{r}', \tag{1.52}$$

where the kernel $K_{n\mathbf{k};n'\mathbf{k}'}(\mathbf{r}, \mathbf{r}')$ reads:

$$K_{n\mathbf{k};n'\mathbf{k}'}(\mathbf{r}, \mathbf{r}') = \kappa(\mathbf{r}, \mathbf{r}')\, u^0_{n,\mathbf{k}}(\mathbf{r})\, u^{0\,*}_{n',\mathbf{k}'}(\mathbf{r}'), \tag{1.53}$$

where $\kappa(\mathbf{r}, \mathbf{r}')$ is the Hartree-plus-XC kernel.

Let us write the susceptibility $\chi(\mathbf{q}, \omega)$ in the SBR. The components of the matrix elements of Eq. (1.44) in the SBR read:

$$\tilde{v}'_{ext,\mathbf{q}}(\mathbf{r}, \omega) \xrightarrow{\text{SBR}} \begin{pmatrix} \{\hat{P}_c^{\mathbf{k}+\mathbf{q}}\, \tilde{v}'_{ext,\mathbf{q}}(\mathbf{r}, \omega)\, u^0_{n,\mathbf{k}}(\mathbf{r})\} \\ 0 \end{pmatrix}, \tag{1.54}$$

and

$$[\,\tilde{v}'_{ext,\mathbf{q}}(\mathbf{r}, \omega), \hat{\rho}^0(\mathbf{r})\,] \xrightarrow{\text{SBR}} \begin{pmatrix} 0 \\ \{\hat{P}_c^{\mathbf{k}+\mathbf{q}}\, \tilde{v}'_{ext,\mathbf{q}}(\mathbf{r}, \omega)\, u^0_{n,\mathbf{k}}(\mathbf{r})\} \end{pmatrix}. \tag{1.55}$$

Hence, the susceptibility $\chi(\mathbf{q}, \omega)$ reads:

$$\chi(\mathbf{q}, \omega) = \left\langle (\{\hat{P}_c^{\mathbf{k}+\mathbf{q}}\, \tilde{v}'_{ext,\mathbf{q}}\, u^0_{n,\mathbf{k}}\}, 0) \middle| (\hbar\omega\hat{I} - \hat{\mathcal{L}}_{\mathbf{q}})^{-1} \cdot (0, \{\hat{P}_c^{\mathbf{k}+\mathbf{q}}\, \tilde{v}'_{ext,\mathbf{q}}\, u^0_{n,\mathbf{k}}\}) \right\rangle, \tag{1.56}$$

where

$$\hat{\mathcal{L}}_{\mathbf{q}} = \begin{pmatrix} 0 & \hat{\mathcal{D}}_{\mathbf{q}} \\ \hat{\mathcal{D}}_{\mathbf{q}} + 2\hat{\mathcal{K}}_{\mathbf{q}} & 0 \end{pmatrix}, \tag{1.57}$$

or, equivalently [see Eq. (1.50)],

$$\chi(\mathbf{q},\omega) = \left\langle (\{\hat{P}_c^{\mathbf{k}+\mathbf{q}}\, \tilde{v}'_{ext,\mathbf{q}}\, u^0_{n,\mathbf{k}}\}, 0) \middle| \begin{pmatrix} \hbar\omega & -\hat{\mathcal{D}}_{\mathbf{q}} \\ -\hat{\mathcal{D}}_{\mathbf{q}} - 2\hat{\mathcal{K}}_{\mathbf{q}} & \hbar\omega \end{pmatrix}^{-1} \begin{pmatrix} 0 \\ \{\hat{P}_c^{\mathbf{k}+\mathbf{q}}\, \tilde{v}'_{ext,\mathbf{q}}\, u^0_{n,\mathbf{k}}\} \end{pmatrix} \right\rangle. \tag{1.58}$$

If the exchange and correlation kernel is adiabatic (i.e. $\kappa(\mathbf{r},\mathbf{r}')$ does not have an explicit dependence on ω) the Liouvillian superoperator (1.57) is frequency independent and thus the susceptibility χ can be efficiently computed using the Lanczos recursive algorithm for any desired range and number of frequencies at the same computational cost. This is important in materials where semicore states need to be included in the valence region of the pseudopotential thus extending a frequency range where spectra can be computed.

1.2.5 Full relativistic TDDFT equations

For systems where spin-orbit coupling (SOC) should be accounted for, in principle, one has to start from the Dirac (or Dirac-Kohn-Sham) equation for a 4-component spinor under the action of an external quadri-potential. It has been shown, however that in DFT calculations relativistic corrections can be included via the pseudopotentials, allowing to solve Pauli-type Kohn-Sham equations for 2-component spinors [30]. In this case the all-electron, Dirac-like Kohn-Sham equations are solved for the isolated atom and then Pauli-like Kohn-Sham equations are solved, tayloring the effective potential to reproduce the solution of the FR atomic Dirac-like equations. The starting point of the FR treatment of the time-dependent problem is the generalization of Eq. (1.14):

(1.59)

where $\psi^{\sigma}_{\mathbf{k},v}(\mathbf{r},t)$ is the two-component spinor, H^{σ_1,σ_2} is the 2×2 Hamiltonian and σ is the spin index that takes two values: ↑ and ↓. The density is also a 2×2 matrix that contains also spin density, and reads:

$$n^{\sigma_1,\sigma_2}(\mathbf{r},t) = \sum_{\mathbf{k},v} \psi'^{*\sigma_1}_{\mathbf{k},v}(\mathbf{r},t)\psi'^{\sigma_2}_{\mathbf{k},v}(\mathbf{r},t), \tag{1.60}$$

and the electron density is the trace of density matrix $n^{\sigma_1,\sigma_2}(\mathbf{r},t)$:

$$n(\mathbf{r},t) = \sum_{\mathbf{k},v,\sigma} \psi'^{*\sigma}_{\mathbf{k},v}(\mathbf{r},t)\psi'^{\sigma}_{\mathbf{k},v}(\mathbf{r},t), \tag{1.61}$$

In Sec. 1.2.1 in order to obtain the second equation (1.21) (or (1.39) in Sec. 1.2.3) I could simply take the complex-conjugate of the Eq. (1.14) and linearize it. In the present case one has to apply the time-reversal operator $\hat{T}$ to Eq. (1.59):

$$\hat{T} = -i\sigma_y K, \tag{1.62}$$

where σ_y is the Pauli matrix and K is the complex conjugate operator. I note that, in fact, in the scalar relativistic case $\hat{T} = K$, so taking a complex-conjugate of the equation is equivalent to applying the time-reversal operator. Linearization of Eq. (1.59) and its time-reversed counterpart gives:

$$\sum_{\sigma_2} \left[H^{\sigma_1\sigma_2}_{\mathbf{k}+\mathbf{q}} - \varepsilon_{n,\mathbf{k}} - \hbar\omega) \right] \hat{P}^{\mathbf{k}+\mathbf{q}}_c \tilde{u}'^{\sigma_2}_{n,\mathbf{k}+\mathbf{q}}(\mathbf{r},\omega) = -\hat{P}^{\mathbf{k}+\mathbf{q}} \tilde{v}_{\mathbf{q}}(\mathbf{r},\omega) u^{0\sigma_1}_{n,\mathbf{k}}(\mathbf{r}) \tag{1.63}$$

$$\sum_{\sigma_2} \left[H^{\sigma_1\sigma_2}_{\mathbf{k}+\mathbf{q}} - \varepsilon_{n,-\mathbf{k}} + \hbar\omega) \right] \hat{T} \hat{P}^{\mathbf{k}+\mathbf{q}}_c \tilde{u}'^{\sigma_2}_{n,-\mathbf{k}-\mathbf{q}}(\mathbf{r},-\omega) = -\hat{P}^{\mathbf{k}+\mathbf{q}} \tilde{v}_{\mathbf{q}}(\mathbf{r},\omega) \hat{T} u^{0\sigma_1}_{n,-\mathbf{k}}(\mathbf{r}) \tag{1.64}$$

with the response density that reads:

$$n'_{\mathbf{q}}(\mathbf{r},\omega) = \sum_{\mathbf{k},v,\sigma} \left(u^{0\sigma*}_{n,\mathbf{k}}(\mathbf{r}) \tilde{u}'^{\sigma}_{n,\mathbf{k}+\mathbf{q}}(\mathbf{r},\omega) + \hat{T} u^{0\sigma*}_{n,-\mathbf{k}}(\mathbf{r}) \hat{T} \tilde{u}'^{\sigma}_{n,-\mathbf{k}-\mathbf{q}}(\mathbf{r},-\omega) \right) \tag{1.65}$$

I note that in this work I have assumed a non-magnetic system, which means that the Hamiltonian of the unperturbed system commutes with the time reversal operator. It allowed to use the same $H^{\sigma_1\sigma_2}_{\mathbf{k}+\mathbf{q}}$ in Eq. (1.64) as in Eq. (1.63). Finally due to the time-reversal symmetry of the unperturbed system one can replace $\hat{T} u^{0\sigma}_{n,-\mathbf{k}}(\mathbf{r})$ with $u^{0\sigma}_{n,\mathbf{k}}(\mathbf{r})$ and obtain the response density in the form similar to the Eq. (1.41):

$$n'_{\mathbf{q}}(\mathbf{r},\omega) = \sum_{\mathbf{k},v,\sigma} u^{0\sigma*}_{n,\mathbf{k}}(\mathbf{r}) \left(\tilde{u}'^{\sigma}_{n,\mathbf{k}+\mathbf{q}}(\mathbf{r},\omega) + \hat{T} \tilde{u}'^{\sigma}_{n,-\mathbf{k}-\mathbf{q}}(\mathbf{r},-\omega) \right) \tag{1.66}$$

For the systems where time-reversal symmetry does not hold, i.e. magentic systems, one has to consider also magentizations density (off diagonal elements of 2 × 2 density matrix in Eq. (1.60)) and keep the density in the form of Eq. (1.65) as it was done in Ref. [29].

1.3 Conclusions

In this chapter I gave an overview of the current state of the art for the TDDFPT approaches to the linear response problem. I have defined the susceptibility of the system in the linear response framework and shown the relation between the dielectric function of the material and susceptibility. I have presented two distinct TDDFPT approaches, namely the Sternheimer and the Liouville-Lanczos methods, that allow the *ab initio* calculation of the susceptibility of the system without the need of computing numerous empty states contrarily to the approaches that involve the solution of Dyson-like equation [19]. The price to pay for this advantage is that the information about the orbital origin of the excitation cannot be retrieved in TDDFPT. Between the Sternheimer and Liouville-Lanczos approaches, the former is more general as it does not require the Hatree-plus-XC kernel to be frequency independent, while the Liouville-Lanczos approach allows to calculate the electronic susceptibility χ for any number of frequencies at the same cost, significantly reducing the amount of CPU time needed to calculate the same spectrum. The formalism presented in this chapter has been developed for norm-conserving pseudopotentials and implemented in the TDDFPT branch [24, 25, 26] of the QUANTUM ESPRESSO suite [31, 32] prior to this work. The extension of the Liouville-Lanczos approach to the calculation of spin-fluctuation spectra in magnetic system has also been done recently [29]. Other possible extensions include the generalization and implementation of the presented formalism to full relativistic ultrasoft pseudopotentials, PAW scheme and higher order response. Chapter 4 of my thesis is devoted to the first direction: the generalization of TDDFPT to full relativistic ultrasoft pseudopotentials.

Chapter 2

Flat and vicinal Au(111) surfaces. Surface states and resonances.

Surfaces states in noble metals have been extensively studied both theoretically and experimentally in the past decades. Special attention has been paid to the L-gap Shockley state in Au, Ag, and Cu(111) surfaces, as it was predicted [11], [18], [17] to support an acoustic surface plasmon excitation that was later found in Be(0001) [12], Cu(111) [14] and Au(111) [13] surfaces. In this chapter I give an overview of the crystal structure and surface states on both flat and stepped Au(111) surfaces. First, I discuss the Shockley surface state on the flat Au(111) [33], [34] and its evolution in the case of stepped (111) Au surfaces [35]. Then I discuss the difference in the surface state behavior of various vicinal surfaces in two distinct cases: electron confinement within the step, for the case of wide terraces, and electron propagation across the step array for narrow terraces.

2.1 Crystal structure of bulk Au and flat Au(111) surface

Bulk gold has the face-centered cubic (FCC) crystal structure shown in Fig. 2.1(a), with an experimental lattice constant $a = 4.07$ Å at room temperature. Different surfaces can be obtained by a cut through the crystal in the direction of the desired plane. In Fig. 2.1(a) the (111) plane is shown, that results in the (111) surface shown in Fig. 2.1(b). The Au(111) surface has 3 types of inequivalent atomic planes depicted with different colors in Fig. 2.1(b). Atoms of the Au(111) surface form a close packed hexagonal lattice with a 3 fold symmetry.

The bulk Brillouin zone (BBZ) and surface Brillouin zone (SBZ) of Au and Au(111) with high symmetry points are reported in Fig. 2.2. As one can see in this figure, the SBZ is obtained by projecting the BBZ onto the desired direction, in this case (111).

I would like to point out that the flat Au(111) surface is not stable and does not have the structure of the ideally cut crystal shown in Fig. 2.1 - it undergoes a $22 \times \sqrt{3}$ herring-bone reconstruction [36]. I note, however, that this reconstruction can be usually neglected in the electronic structure calculations, as it has been shown to have a minimal

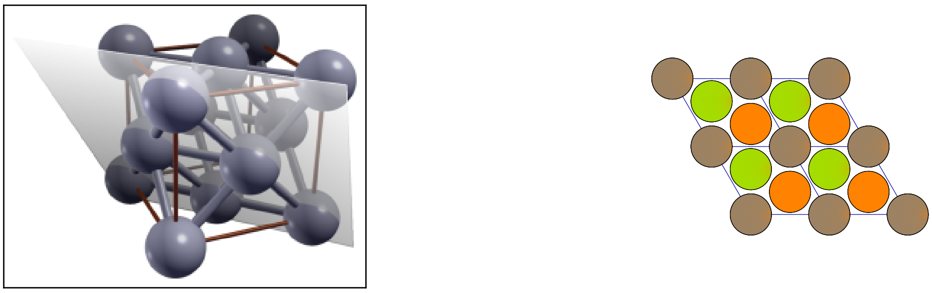

(a) (b)

Figure 2.1: Crystal structure of (a) bulk Au that shows a (111) plane and (b) top view of the Au(111) surface; Atoms colored as brown, green and orange are atoms that belong to the first, second and third layers respectively.

impact on the surface electronic structure [37].

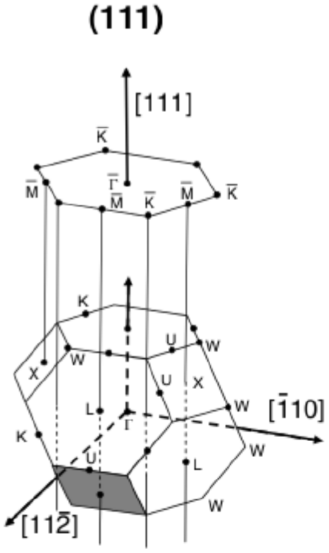

Figure 2.2: The bulk Brillouin zone (BBZ) and (111) surface Brillouin zone (SBZ) of gold. From Ref. [38].

2.2 Surface states of noble metals

2.2.1 Surface states

In an infinite crystal, orbitals of valence electrons overlap forming continuous electronic bands that extend over the whole crystal and are separated by gaps in some regions of the momentum space. In finite crystals the symmetry at the surface is broken and surface states can emerge in forbidden bulk energy gaps. Since these states lie in the gap of bulk states they cannot extend into the crystal and effectively form a quasi-2D gas at the surface. The wavefunction of the surface state is exponentially damped in the direction perpendicular to the surface. If one model a crystal as a semi-infinite chain of periodically arranged atoms and solve the Schrodinger equation for this system [39] one would obtain following solutions for the surface state wavefunction:

$$\psi(z) = A_i e^{-kz} cos(Gz/2 + \delta) \tag{2.1}$$

for the region inside (index i the crystal ($z < 0$) and

$$\psi(z) = A_o e^{-\lambda z} \tag{2.2}$$

for the region outside (index o) the crystal ($z > 0$). Here A_i and A_o are normalization constants, G is the reciprocal lattice vector along the z-direction, δ is a phase that goes from 0 to $\pi/2$, k and λ are the decay coefficients.

Surface states on noble metals are very sensitive to surface defects like adsorbates or steps and thus offer an ideal tool to study low dimensional electronic properties. Surface states can be studied using various experimental tools including scanning tunnel microscopy (STM) and angle-resolved photoemission spectroscopy (ARPES) as well as theoretically using *ab initio* methods like density functional theory (DFT) [40, 41].

2.2.2 Surface states of the flat Au(111) surface

The Au(111) surface band structure calculated in the scalar relativistic (SR) ultrasoft pseudopotential scheme is reported in Fig. 2.3. In this calculation the surface state is defined as a state for which $|\psi|^2 > 0.6$ on the first two layers of the surface. The Shockley surface stated associated with the zone-boundary hybridization at the L-point of the BBZ is located in the so-called the L-gap of projected bulk bands at the center of the SBZ, $\overline{\Gamma}$ 0.4 eV below the Fermi level and has a parabolic free-electron like dispersion away from $\overline{\Gamma}$ around the band minimum. This surface state has mainly a *sp* character and extends deep into the bulk of the metal, hence a thick slab is required in order to decouple the two surfaces in the slab-supercell geometry.

Inclusion of the spin-orbit coupling (SOC) leads to noteworthy changes in the surface band structure (shown in Fig. 2.4) that have been discussed in details in [34]. The most relevant effect of SOC for this work is the Rashba splitting of the Shockley surface state into two parabolic bands separated along $\mathbf{k}_{||}$ and slightly shifted downward compared to the SR calculation. However, except for this fact, the general behavior of the surface state remains the same in both SR and FR cases: it has a nearly free-electron like dispersion with the minimum around 0.4 eV below the Fermi level. I point out that in both cases (SR and FR) there is a well defined gap in the projected bulk band structure (PBS) at Γ point that is sometimes called the L-gap as the L symmetry point of the bulk Brillouin zone is projected onto the Γ point of the surface Brillouin zone.

2.2.3 Surface states and surface resonances

When speaking about surface states it is important to distinguish between the so-called "true" surface states and surface resonances. On the one hand "true" surface states are

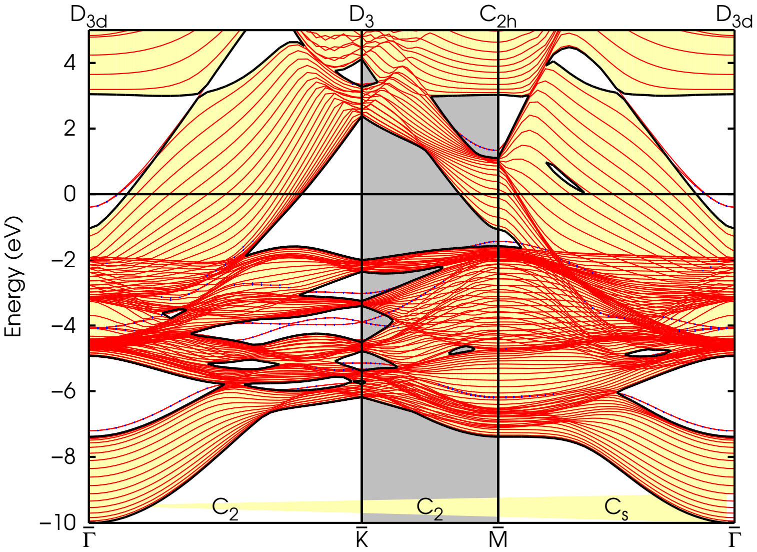

Figure 2.3: LDA scalar relativistic (SR) surface band structure of Au(111) simulated by a 21-layer slab. Reproduced after Ref. [34] using similar parameters. Zero of energy is rhe Fermi level.

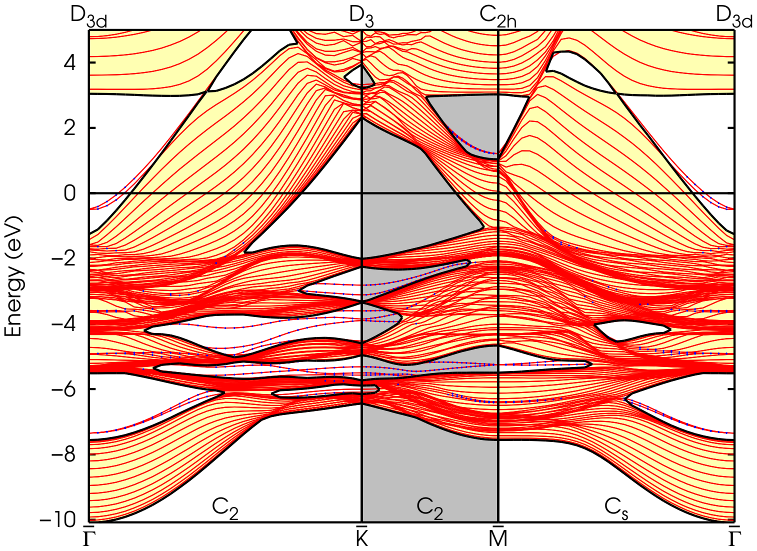

Figure 2.4: LDA full relativistic (FR) surface band structure of Au(111) simulated as 21-layer slab. Reproduced after Ref. [34] using similar parameters. Zero of energy is rhe Fermi level.

usually located in the gap of the projected bulk bands, thus these state are well localized at the surface and do not mix with bulk states. Alternatively, the surface state can exist within the continuum of bulk states if they are distinguished by the symmetry, making the coupling between surface and bulk bands symmetry forbidden.

Surface resonances, on the other hand, are states located within the projected bulk bands of the same symmetry, thus they can mix with bulk states forming somewhat

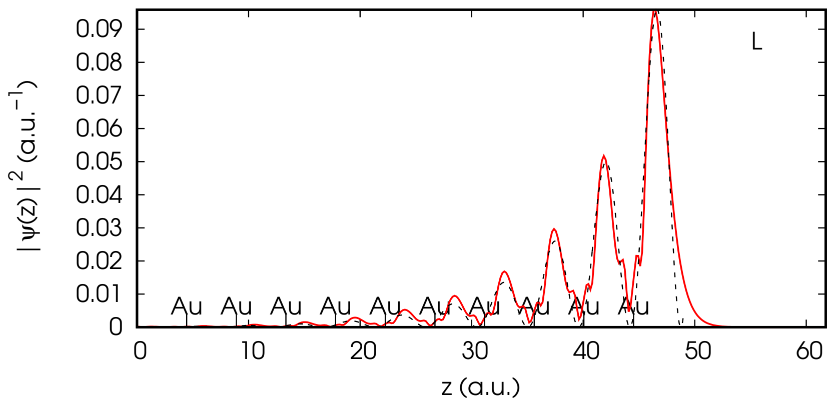

(a)

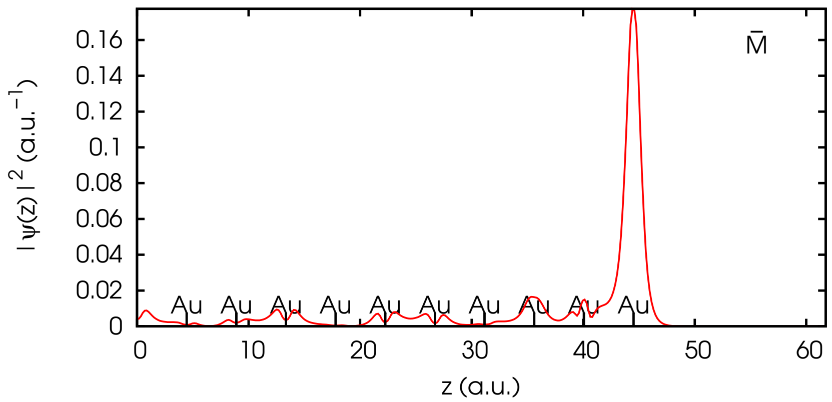

(b)

Figure 2.5: Au(111) surface planar averages of (a) the "true" (i.e. non-resonant) surface state of Au(111) at the $\overline{\Gamma}$ point (red line) and its fit with Eq. (2.1) using the following parameters: $A_i = 0.011$, $k = 0.0715$, $G/2 = 0.706$, $\delta = -3/2\pi$. (b) the surface resonance of Au(111) at the $\overline{M}$ point of Fig. 2.3 (SR calculation).

localized states that can extend deep into the bulk. In this case in equation (2.1) term e^{kz} will be replaced by $e^{kz} + B$ where B defines the part of the state that extends infinitely in the bulk of the surface.

In Fig. 2.5 I show the plots of the planar average of the charge density that correspond to surface state and surface resonance from the band structure in Fig. 2.3. In Fig. 2.5(a) the planar average for the L-gap Shockley state at $\overline{\Gamma}$ shows that while the state penetrates deep into the bulk it is still localized and can be described using Eq. (2.1) (black dashed line). The charge density planar average in Fig. 2.5(b) for state at about -6.5 eV at $\overline{M}$, on the other hand, shows that it has a bulk tail while been partially localized on the surface, hence it is identified as a surface resonance. I point out that in this particular case the surface resonance is quite well localized at the surface allowing an easy identification - in general it can have a more intense bulk tail, making the identification more difficult, as one will see in Chapter 5.

2.3 Vicinal Au(111) surfaces

2.3.1 Vicinal Au(111) surface geometry and projected bulk bands

Stepped Au(111) surfaces, also known as high Miller's index surfaces or vicinal surfaces are obtained by cutting the single crystal with a plane that deviated from the (111) plane by a small miscut angle. The resulting surface will consist of flat terraces of the (111) plane separated by monoatomic steps, characterized by the terrace width L, step array periodicity d, miscut angle α and the step height h. In this case, the regular array of steps form a periodic array of step potential barriers, with a barrier-to-barrier distance equal to d. The schematic side view of the vicinal surface is reported in Fig. 2.6. I point out that change of the geometry of the surface leads also to the change of the unit cell type and SBZ shape for the vicinal surface from the hexagonal to tho orthorhombic one (see Fig. 2.7). Contrarily to the Au(111) case shown in Fig. 2.2 where the L point of the BBZ in the [111] direction was projecting onto the $\overline{\Gamma}$ point of the SBZ pf the Au(111) surface, in the vicinal surface case, the L point projection will be shifted by π/d and will become the SBZ edge $\overline{Y}$. I also note that the Au(111) surface can be described using the orthorhombic unit cell, however it will not be the smallest possible unit cell. Hence I will refer to the hexagonal unit cell of the Au(111) surface as to the primitive cell.

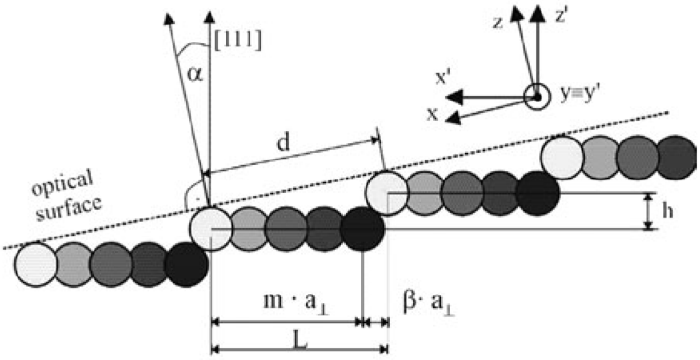

Figure 2.6: Side view of the vicinal surface structure. Adopted from the Ref. [42].

It is crucial to note that the gap at the Fermi level of the projected bulk bands at the $\overline{\Gamma}$ point (see Fig. 2.3) might no longer be supported on vicinal surfaces. In Fig. 2.8 I report the scheme from Ref [42] that shows the evolution of the gap in the PBS. In this scheme the circles describe the bulk Fermi surface in the first Brillouin zone with its characteristic necks. Dark shaded regions indicate the projection of bulk states from the two halves of the Fermi surface, whereas light shaded areas correspond to bulk states projected from one side of the Fermi surface. In the cases of Au(111) ($\alpha = 0°$) and Au(788) ($\alpha = 3.5°$) the projections of the two necks from the opposite sides of the Fermi surface overlap form a gap at $\overline{\Gamma}$. When increasing the miscut angle, the region where the projections of the two necks overlap will be getting small until a certain critical angle α_c, at which the gap at $\overline{\Gamma}$ will close ($\alpha_c = 10.2°$for Au(111) vicinal surfaces [35]). As one can see, for Au(788)

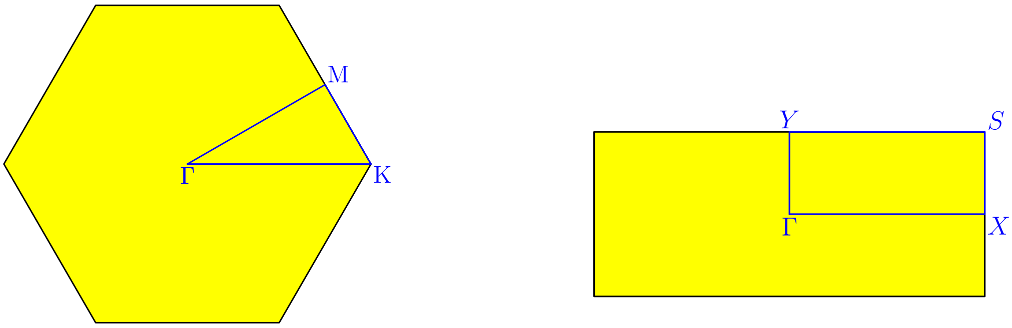

(a)

(b)

Figure 2.7: SBZ with high-symmetry point of (a) the hexagonal Au(111) surface and of (b) the orthorhombic Au(111) vicinal surface.

($\alpha = 3.5°$) the gap at the SBZ center that supports the L-neck state is present, while for Au(322) ($\alpha = 11°$) bulk states are projected over the whole SBZ and thus only surface resonance can exist.

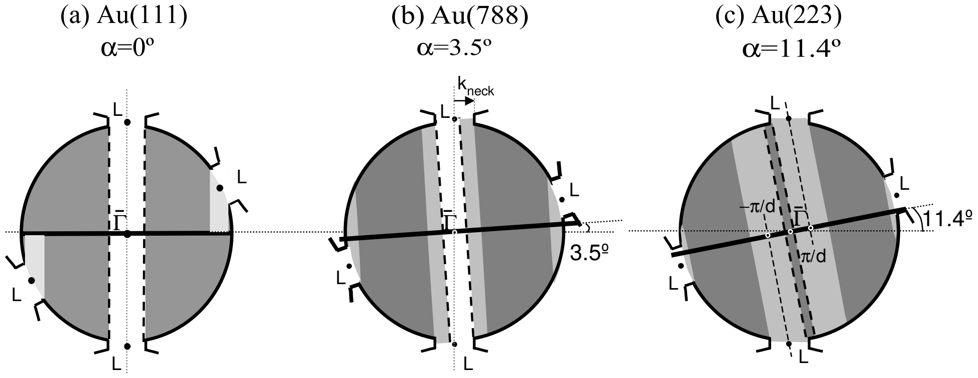
(a) Au(111)
α=0º

(b) Au(788)
α=3.5º

(c) Au(223)
α=11.4º

Figure 2.8: . Bulk band projection at $E = E_F$ onto vicinal surfaces with small and high miscut angles in the xz plane. Dark-grey zones are the regions where bands are projected from both sides of the BZ, whereas light-grey zones present projection only from half a side. From Ref. [42].

2.3.2 Vicinal Au(111) surface states

Stability, self organization and surface states for different vicinal surfaces of Au have been studied thoroughly in the past decades [43, 44, 45, 46, 35], revealing, in particular, that the L-gap Shockley state of the (111) Au surface is significantly modified between the flat Au(111) and vicinal surfaces with narrow or wide terraces [46, 35]. It has been shown using ARPES that on the vicinal surface with a narrow terrace, Au(322), the surface state becomes a surface resonance as due to the relatively big miscut angle (11.4°) the gap in the PBS at the Fermi level around Γ point vanishes (see Fig. 2.8). Thus, the

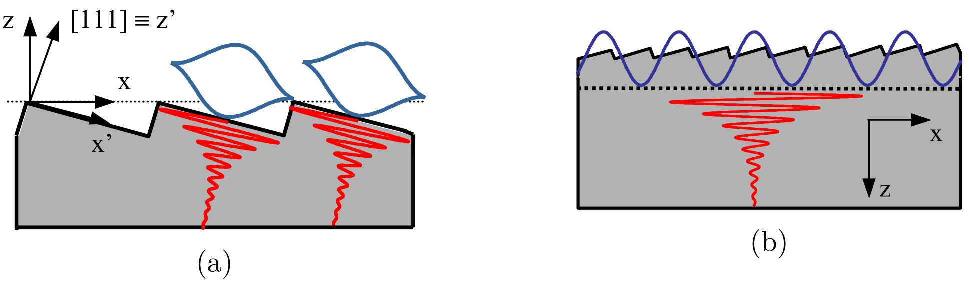

(a)
(b)

Figure 2.9: 2.9(a) Terrace modulated versus 2.9(b) Average surface modulated character of the surface state .

surface state overlaps with bulk states decreasing significantly the localization of the state near the surface. On the other hand, the terrace width is narrow enough to allow the electrons that belong to surface state to propagate across the surface plane in the direction perpendicular to the step. At variance, for the small miscut angles of Au(788) and Au(21 23 23), the gap in the PBS in maintained allowing to support a "true" Shokley surface state. The wide terraces of Au(788) and Au(21 23 23) surfaces lead to the confinement of the surface state within each terrace. In this case a surface state behaves like a quantum well state which, contrasting to the free electron surface state of Au(111) with parabolic dispersion, forms weakly dispersive subbands.

2.3.3 Surface state modulation

Finally, one should distinguish between the terrace modulated and average-surface modulated character of the surface state shown in Fig. 2.9. In the former case, that occurs for the well-confined 1D states, one can say that the 1D state does not 'see' the average, stepped surface. It means that the electron in this state is effectively in a 1D quantum well and its wavefunction will be decaying into the bulk in the direction perpendicular to the terrace, as shown in Fig. 2.9(a). In the latter case, however, the electrons of the 2D state can propagate across the whole surface as it shown in Fig. 2.9(b). In this case the electron moves in a superlattice and its wavefunction will be decaying into the bulk in the direction perpendicular to the average surface that differs from the terrace plane by the miscut angle.

2.3.4 The Kronig-Penney model for the surface state confinement

Simple analysis of the band structure for vicinal surfaces can be performed in the framework of the 1D Kronig-Penney model as the step lattice can be viewed as an array of potential barriers. For this purpose I will adapt the notation of [47, 42]. For the array of δ-Dirac potential barriers $U_0 b\delta(x)$ following quantities are defined: $q_0 = (m^*/\hbar^2)U_0 b$, $q = \sqrt{(2m^*/\hbar^2)(E - E_0)}$ where E_0 is the energy of the band bottom for the free electron case (infinite terrace width). Finally the transmission coefficient $T = |T|e^{i\phi}$ is defined as

$T = q/(q + iq_0)$. Then the dispersion relation for the electron takes the following form:

$$cos(qL + \phi) = |T|cos(k_x L), \tag{2.3}$$

or, in terms of energy

$$E(k_x) = \frac{\hbar^2}{2m^* L^2}[cos^{-1}(|T|cos\, k_x L) - \phi]^2. \tag{2.4}$$

This model contains only one adjustable parameter, the barrier strength $U_0 b$, that can be obtained from the fit of this equation onto the calculated or measured surface state bands, allowing the direct quantitative comparison of the obtained results. It has been already successfully used for the analysis of the ARPES results for vicinal surfaces of Au(111) and Cu(111) [35, 46, 42, 48]

2.4 Conclusions

In this chapter I have briefly reviewed the surface structure and surfaces states of the flat and some vicinal Au(111) surfaces. I have discussed the Shockley surface state on flat Au(111) surface pointing out that taking into account SOC is important to observe the two Rashba split Shockley surface states at the center of SBZ. Apart from the Rashba splitting, SOC is not crucial to observe the surface state in *ab initio* calculation as the latter is already seen at the scalar relativistic level. Then I have discussed the general structure of (111) vicinal surfaces and significant modifications of surface states due to the geometry change, such as the transition between surface state and surface resonance, terrace modulated versus average-surface modulated states.

Chapter 3

EEL spectrum and plasmon excitations of Au.

Electron energy loss (EEL) spectroscopy [49] is a powerful experimental method that allows one to measure the change in kinetic energy -the energy loss- of electrons after their interaction with a sample. This technique can be used to obtain structural and chemical information about a specimen -from the high-energy loss region of the spectrum- as well as information about valence electron excitations -from the low-energy loss region of the spectrum-. In particular, the valence region of the spectra contains information about the band structure and dielectric properties of the material: plasmons, surface plasmons and interband transitions. For some materials like aluminum, the valence EEL spectrum has a simple structure containing one single, well-defined, plasmon peak for which the Drude model is a pertinent approximation.

In materials where the behavior of valence electron is far from the (quasi) free electron model however, the EEL spectrum contains many peaks from single, to collective and to superposition of collective and single excitations, that make it difficult to analyze. Indeed, noble metals, such as Au, that is the main material I will be studying is one of these cases.

In this chapter I will give an overview of the existing experimental and theoretical EEL spectra for bulk and surfaces of gold focusing on the conventional bulk and surface plasmons as well as on acoustic surface plasmons. First, I will discuss the types of plasmonic excitations that can be observed in EELS experiments. Then I will discuss the recent *ab initio* calculations of EEL spectra for Au, their comparsion with experiments and will point out limitations of the conventional approximations.

3.1 Bulk and surface plasmons

3.1.1 The Drude model

In the Drude model [50] for the dielectric function of metals that assumes free (or nearly free) electrons, the dielectric function ϵ reads:

$$\epsilon(\omega) = 1 - \frac{\omega_p^2}{\omega(\omega + i\gamma)}, \tag{3.1}$$

where ω_p is the plasma frequency and γ is the damping time (or equivalently the inverse relaxation time $\tau = 1/\gamma$). Corresponding real and imaginary part of the dielectric funtction are:

$$Re[\epsilon] = 1 - \frac{\omega_p^2}{\omega^2 + \gamma^2} \qquad Im[\epsilon] = \frac{\gamma \omega_p^2}{\omega(\omega^2 + \gamma^2)} \tag{3.2}$$

The Drude model is a good approximation for free-electron metals like aluminum. For non-free-electron like materials (e.g. silver) the band structure effects should be taken into account.

3.1.2 Bulk plasmon

A bulk plasmon is a collective oscillation of the free electron density in the bulk of the material. For the case of $\mathbf{q} \to 0$ the condition of bulk plasmon excitation that can be obtained from the Drude model, is the following: $Re[\epsilon(\mathbf{q}, \omega)] = 0$ and $Im[\epsilon(\mathbf{q}, \omega)]$ should have a local minimum. In the free electron model, the frequency of the bulk plasmon at $\mathbf{q} \to 0$ is determined by the density of valence electrons:

$$\omega_{BP} = \sqrt{\frac{4\pi n e^2}{m_e}}, \tag{3.3}$$

where n is electron density, m_e is the mass of the electron and e is the electron charge. For the case of finite momentum transfer $\omega_{BP} \sim \mathbf{q}^2$. In real systems the actual value of ω_{BP} may deviate from the value that can be obtained from Eq. (3.3) due to the presence of an interband transition with a frequency lower than the free electron plasma frequency, that screens the bulk plasmon and pushes it down in frequency as explained with the help of a simple model given in Ref. [51] and the supplemental material (SM) of Ref. [52]. In that model a system consists of a free electron gas with a plasma frequency ω_{BP} that coexists with a bound Lorentz oscillator of frequency ω_1. Assuming that damping terms are small, the dielectric function is reduced to its real part:

$$\epsilon(\omega) = 1 - \frac{\omega_{BP}^2}{\omega^2} + \frac{f_1 \omega_{BP}^2}{\omega_1^2 - \omega^2}, \tag{3.4}$$

with f_1 being the oscillator strength for bound electrons. In this system collective oscillations will occur at the frequency where $\epsilon(\omega) = 0$. For the noble metals $\omega_{BP} \gg \omega_1$ and the dielectric function of Eq. (3.4) will become zero at two frequencies $\Omega_1 \approx \omega_1(1+f_1)^{-1/2}$ and $\Omega_1 \approx \omega_{BP}(1+f_1)^{1/2}$. If the imaginary part of dielectric function at one of this frequencies is small the plasmon excitation can develop.

3.1.3 Surface plasmons

While bulk plasmons appear in the bulk of the material and can be observed in most metals and semiconductors, surface plasmons occur at the interface between a material surface and a dielectric medium. A surface plasmon is a collective oscillation of the free electron density at the interface and forms a wave propagating along the interface. By contrast to the bulk plasmon that occurs when $Re[\epsilon(\mathbf{q}, \omega)] = 0$ the surface plasmon is excited when $Re[\epsilon(\mathbf{q},\omega)] = -1$ [53] (generally speaking $Re[\epsilon(\mathbf{q},\omega)] = -\epsilon_{dm}$, where ϵ_{dm} is the dielectric function on the media above the surface). One should also note that in bulk materials plasmons occur in any direction of the electron wave vector, while in the case of a surface the wavevector should have the component parallel to the surface (denoted as $\mathbf{q}_{||}$ further in text). In the free electron model, the frequency of the plasmon is once again governed by the electron density and, consequently, is proportional to the bulk plasmon frequency:

$$\omega_{SP} = \frac{\omega_{BP}}{\sqrt{2}}. \tag{3.5}$$

For the case of a finite momentum transfer $\omega_{SP} \sim \mathbf{q}_{||}^2$. Similarly to the case of bulk, ω_{SP} changes due to the presence of interband transitions in real systems. The surface plasmon can be coupled to the light, forming surface plasmon polariton that allows to confine light in the subwavelength region and propagate it along the surface. The non-linear dispersion has the consequence that the propagation of nonmonochromatic wavepackets becomes problematic and cannot occur without distortion.

3.1.4 Acoustic surface plasmons

For the case of a 2D electron gas it has been predicted [54] that surface plasmons will exhibit a square-root dispersion $\omega_{2D} \sim \sqrt{\mathbf{q}_{||}}$ and it was shown for the case of graphene that even better light confinement with respect to conventional surface plasmons (CSP) can be achieved. Although similar to the CSP, this kind of dispersion does not allow a distortionless propagation. A new type of 2D surface plasmon called acoustic surface plasmon has been predicted [11] to exist on a 3D metal surface when a partially occupied 2D Shockley surface state interacts with the underlying 3D electron gas and, as a result of this screening of the quasi-2D band, the dispersion of the 2D surface plasmon changes from a square-root like behavior to a linear one:

$$\omega_{ASP} = \alpha v_f^{2D} q, \tag{3.6}$$

where α is a coefficient close to the unity that depends on the separation between the quasi-2D electron gas formed by the Shockley state and the underlying 3D electrons as well as on its penetration character, v_f^{2D} is the 2D Fermi velocity and q is a in-plane wavector. Typical ASP energy lies in the range of 0.2-1.5 eV. On the one hand, the low excitation energy may allow ASP to participate in many dynamical processes involving electrons and phonons. On the other hand, due to the sound-like dispersion, a signal consisting of several ASP waves can propagate along the surface without distortion. They thus could be used to localize the electro-magnetic field near the surface and enhance it without distortion. ASP has been observed experimentally on Be (0001) [12], Au (111) [13], Cu (111) and Au (788) surfaces [16].

3.2 EEL spectra of bulk Au and Au surfaces. Bulk and surface plasmons in EELS

3.2.1 Bulk Au

Dielectric properties of bulk and surface of Au have been thoroughly studied theoretically in the past decades. Those studies include both the calculation of the dielectric function for $\mathbf{q}$=0 (optical case) and for finite value of $\mathbf{q}$. Notably, the role of localized d-bands, crystal local fields and exchange-correlation functional were investigated. In particular it has been shown [55] (see Fig. 3.1(a)) that d-bands are essential to reproduce the structure of the EEL spectra and to provide a polarizable background which significantly lowers the free electron plasma frequency and damps the bulk (and surface) plasmon peak. This effects, as well as the influence of the local fields, exchange-correlation functional have been studied further [52] with a special attention to the EEL spectra for E>10 eV. In particular, it has been shown (see Fig. 3.1(b) that local fields start to have an effect on the loss spectra from 10 eV and lead to more pronounced changes at higher energies, while the effect of the TDLDA kernel, compared to the RPA one, is quite small. As one can see in Fig. 3.1(b) agreement between the *ab initio* calculations and experimental results for EEL specta of Au is good except for the plasmon peak for reasons that I will discuss in the Chapter 6.

I would like to note also that in Ref. [52] other noble metals have been studied revealing similar trends in the behavior of the loss function for Cu and Ag.

3.2.2 Adequation and limitations of LDA/GGA for the prediction of plasmons

As I have pointed out in the previous section good agreement between theoretical and experimental loss function was observed in Ref. [52] with the notable exception of the bulk plasmon peak position that is severely damped in Au and is damped and shifted in Ag. This occurs as the energy of the 5d bands in Au (and 4d in Ag) are to high in the LDA or GGA leading to the underestimation of the 5d->6s interband transition onset and thus complete screening of the bulk plasmon in Au (see. Sec. 3.1.2 and SM of the Ref. [52]). It has been shown that by using the GW corrections or orbital-depend GLLBSC exchange-and-correlation functional it is possible to restore the correct interband transition energy and thus the plasmon peak in the EEL spectra. The same trend is observed for surfaces of Au and Ag: for the Au(111) surface the surface plasmon peak does not develop in LDA according to Ref. [58] and for the Ag(111) surface it appears less sharp and redshifted [58]. In both cases the use of GLLBSC potential allows to restore the correct position of the surface plasmon peak and to make it more sharp for Ag(111) surface. Improvements of the bulk and surface plasmons description is also expected from the GW or LDA+U approaches [59, 52]. Nonetheless, since gold as well as any other metal does not have a gap between the valence and conducting band LDA and GGA are usually considered pertinent approximations for the EEL spectrum simulations, contrarily to the semiconductors, where electron-hole interactions and excitonic effects should be properly

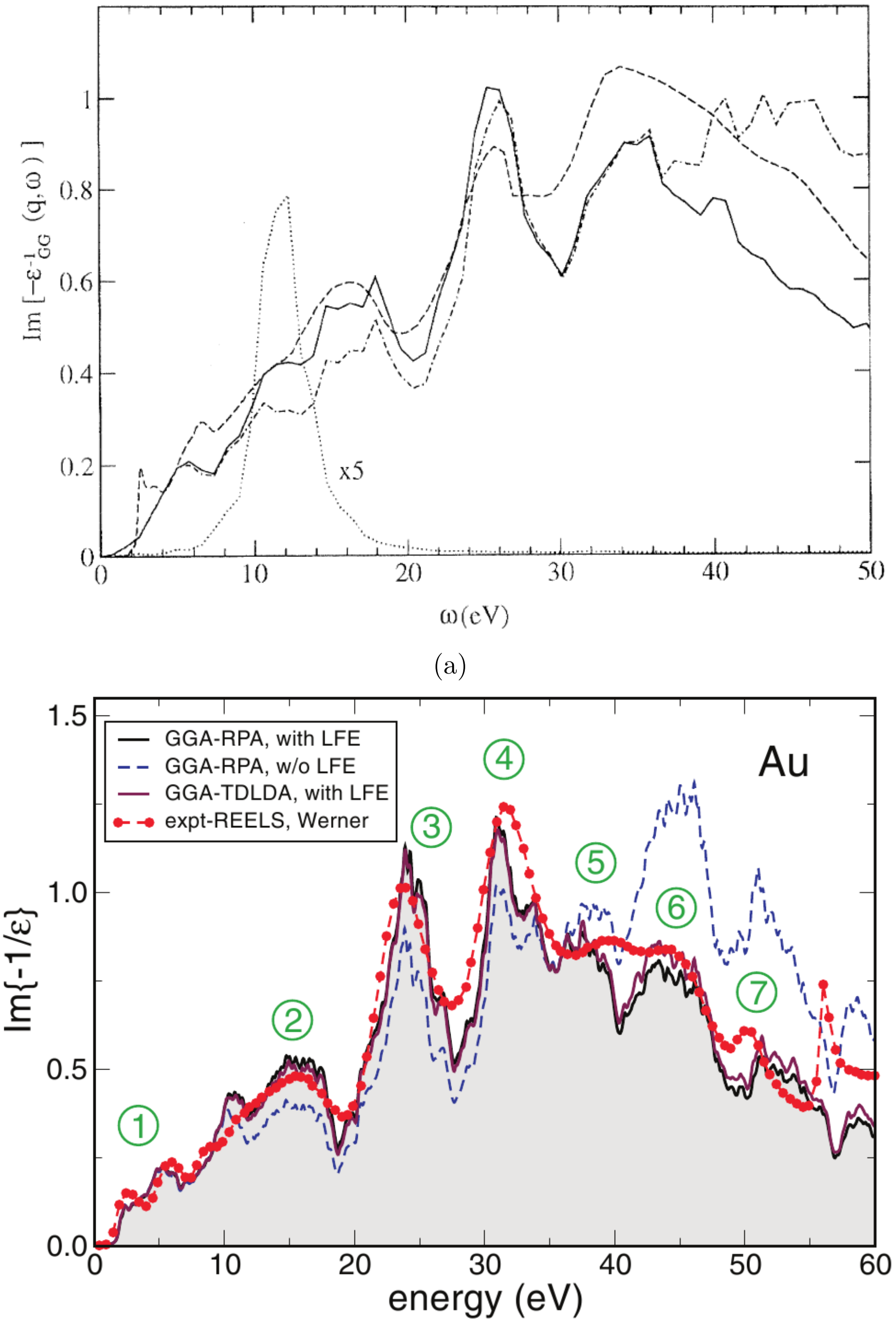

(a)

(b)

Figure 3.1: EEL spectra for bulk Au: (a)(a) The solid and dot-dashed lines represent the results of RPA calculation including and excluding local-field effects, the dotted line represents the result of assigning 5d electrons to the core and the dashed line is the experiment results of Ref. [56] (adopted from Ref. [55], (b)(b) Comparison of EEL spectrum calculations using different approximations with experimental REELS results of Ref. [57] (adopted from Ref. [52]).

accounted for using many-body approaches like GW or Bethe-Salpeter equation [19, 60].

3.2.3 Acoustic surface plasmon in EELS experiments and simulations

An acoustic surface plasmon (ASP) on gold surface has been first predicted to exist [11, 17, 18] and then found experimentally [61, 13] on the Au(111) surface as well as on the Cu(111) surface [14, 15]. In the first experiments [61] on Au(111) the reported ASP dispersion has been significantly larger than expected, raising a question of the understanding of the underlying physics. On the other hand, dispersion of the Au(111) ASP measured in more thorough experiments in Ref. [13] is in good agreement with *ab initio* calculation performed for Au(111) surface [58, 13] for ASP energies up to 0.6 eV. One of the key results of these studies was that $\alpha < 1$ in Eq.(3.6) contrarily to the theoretical predictions based on the 1D model. Indeed, the assumption that ASP results from the screening of the surface electron states by the majority of faster bulk electrons turns out to be inexact. A similar situation was observed for Cu(111): in the first experiments [14] it appeared that $\alpha > 1$ however later it has been demonstrated [15] that the fit of experimental peaks in Ref. [14] was not done correctly, and that the actual situation in Cu(111) resembles that of Au(111) surface with $\alpha < 1$. It is worth to note that *ab initio* dispersion of Ref. [58] agreed quite well with first experiments [14] but gives a too high slope compared to the most recent results [15].

3.2.4 Identification of ASP in the calculations

In the *ab initio* calculations of Refs. [58, 13] ASP was identified in different ways. In Refs. [12, 62, 13] the surface response function [63, 64] has been computed for the surface simulated as a slab for different values of $\mathbf{q}$. Maxima of this response function in low energy region of spectra that have linear dispersion with respect to $\mathbf{q}$ have been identified as ASP. In Ref. [58] a different way has been implemented. In addition to the calculation of the surface response function, the dielectric band structures of surfaces have been computed, where authors have identified a stand-out band that represent the surface mode that comes from the Shockley surface state and that is responsible for the ASP excitation.

3.3 Conclusions

In this Chapter I gave a brief overview of the types of plasmonic excitations that can exist in noble metals and of existing studies, both theoretical and experimental of EEL spectra and plasmons. Multiple theoretical studies have been performed on the EEL spectra of bulk Au and other noble metals in the past decades, focusing on different approximations and calculations aspects except influence of the spin-orbit coupling. It has been shown that good agreement between *ab initio* calculations with experiments is reached even for LDA exchange-correlation functional with the one prominent exception of the bulk plasmon that appears shifted and damped. This issue can be fixed by the use of more advanced approaches such as the GW method or the use of the orbital-dependent GLLBSC functional. While properties of bulk and conventional surface plasmons for noble metals seem to be well understood, there are certain contradictions when it comes to the acoustic surface plasmons on Au(111) and Cu(111) surfaces. Thus the goal of the present work is to perform the missing study of SOC influence on EEL spectra of Au bulk and (111) surface and then to study the ASP dispersion with SOC in an effort to bring more insight on its properties for Au(111) surface.

Part II

Theoretical results

Chapter 4

Methodological and software development

This chapter is devoted to the methodological and software development aimed at the generalization of the TDDFPT approach presented in Chapter 1 to the full-relativistic (FR) ultrasoft pseudopotentials (USPP). First I will present the TDDFPT equations in the scalar-relativistic USPP scheme, that has been implemented in the Quantum ESPRESSO suite before this work and is not yet published. Then I will show the way to generalize it to the FR case. Finally I will give the comparison of different TDDFPT implementations, namely the Sternheimer and the Liouville-Lanczos approaches and I will conclude with further perspectives of these development.

The work presented in this Chapter was done in close collaboration with Andrea Dal Corso. Most of the methodological development was done during my three week-long visits to SISSA (Trieste, Italy). The paper on the comparison of the Sternheimer and Liouville-Lanczos approaches has been accepted for publication [65] and the development part has not been published yet.

4.1 TDDFPT in the scalar relativistic USPP scheme

Ultrasoft pseudopotentials allow to significantly reduce the kinetic energy cutoff for wavefunctions in calculations with a plane wave basis set. In the past decades numerous developments have been done to generalize DFPT for lattice dynamics [66, 67], electric field perturbations [68] and TDDFPT for optical absorption of molecules [22] to the SR USPP scheme. Moreover, DFT [69] and DFPT for lattice dynamics [70] have been also generalized to the FR USPP scheme.

4.1.1 TDDFPT equation in the USPP scheme

In the USPP scheme [71] the electronic charge density is written as:

$$n(\mathbf{r},t) = \sum_{i,\mathbf{k}} \langle \psi_{i,\mathbf{k}} \,|\, K(\mathbf{r}) \,|\, \psi_{i,\mathbf{k}} \rangle \,, \tag{4.1}$$

where $K(\mathbf{r})$ contains an augmentation term:

$$K(\mathbf{r}) = |\mathbf{r}\rangle \langle \mathbf{r}| + \sum_{Inm} Q^I_{mn}(\mathbf{r}) |\beta^I_m\rangle \langle \beta^I_n| \tag{4.2}$$

where the augmentation functions $Q^I_{mn}(\mathbf{r})$ are localized in the core region of the atom I and calculated together with the PP. I note that by setting the augmentation term to zero one can recover the electronic density of the norm-conserving pseudopotential (NCPP) scheme. Projector functions $\beta^I_n(\mathbf{r}) \equiv \beta^I_n(\mathbf{r} - \mathbf{R}_I)$ are also defined and centered for each atom and are provided with PP, indices m and n run over the β functions that are equivalent to Kleinman-Bylander projectors in the NCPP scheme [72].

The basic TDDFPT equation in the USPP scheme remains similar [73] to the Eq. (1.14) for the NCPP scheme:

$$i\hbar\hat{S}\frac{\partial \psi_{i,\mathbf{k}}(\mathbf{r},t)}{\partial t} = \hat{H}_{KS}(\mathbf{r},t)\psi_{i,\mathbf{k}}(\mathbf{r},t), \tag{4.3}$$

where $\hat{S}$ is an overlap operator ensuring the generalized orthonormalization constraint in the USPP scheme:

$$\langle \psi_i|\hat{S}|\psi_j\rangle = \delta_{ij} \tag{4.4}$$

and $\hat{S}$ is defined as:

$$\hat{S} = 1 + \sum_{Inm} q_{mn} |\beta^I_n\rangle \langle \beta^I_m| , \tag{4.5}$$

or in the coordinate representation

$$S(\mathbf{r}_1, \mathbf{r}_2) = \delta(\mathbf{r}_1 - \mathbf{r}_2) + \sum_{Inm} q^I_{nm}\beta^I_n(\mathbf{r}_1 - \mathbf{R}_I)\beta^I_m(\mathbf{r}_2 - \mathbf{R}_I), \tag{4.6}$$

where coefficients $q^I_{nm} = \int d\mathbf{r} Q^I_{mn}(\mathbf{r})$ are the augmentation function integrals. Once again, if augmentation functions are zero we will retrieve the NCPP Kohn-Sham equation in the Kleinman-Bylander form [72] and a standard orthonormalization constraint. I note that in the USPP scheme the projector onto empty states is also modified:

$$\hat{P}_c = \sum_i^{unocc} |\psi_i\rangle \langle \psi_i| \hat{S} \tag{4.7}$$

and we also introduce its Hermitian conjugate form:

$$\hat{P}_c^\dagger = \sum_i^{unocc} \hat{S} |\psi_i\rangle \langle \psi_i| . \tag{4.8}$$

4.1.2 Response density in the USPP scheme

The linear term of the response charge density in the USPP scheme reads:

$$\begin{aligned} n'(\mathbf{r},\omega) = &\sum_{i,\mathbf{k}} \psi^{0*}_{i,\mathbf{k}}(\mathbf{r})\psi^{'}_{i,\mathbf{k}}(\mathbf{r},\omega) + \sum_{i,\mathbf{k}} \psi^{0}_{i,\mathbf{k}}(\mathbf{r})\psi^{'*}_{i,\mathbf{k}}(\mathbf{r},-\omega)+ \\ &\sum_{i,\mathbf{k}}\sum_{Inm} Q^I_{mn}(\mathbf{r}) \left[\langle \psi^{'}_{i,\mathbf{k}}(-\omega)|\beta^I_m\rangle \langle \beta^I_n|\psi^0_{i,\mathbf{k}}\rangle + \langle \psi^0_{i,\mathbf{k}}|\beta^I_m\rangle \langle \beta^I_n|\psi^{'}_{i,\mathbf{k}}(\omega)\rangle\right] \end{aligned} \tag{4.9}$$

Let us now find the expression for the lattice periodic part of the density response. We start with the scalar products of the β functions with unperturbed wavefunctions ψ^0:

$$\langle\beta_n^I|\psi_{i,\mathbf{k}}^0\rangle = \int d\mathbf{r}\beta_n^I(\mathbf{r}-\mathbf{R}_I)e^{i\mathbf{kr}}u_{i,\mathbf{k}}^0(\mathbf{r}). \tag{4.10}$$

To proceed further we change variables: $\mathbf{R}_I = \mathbf{R}_\mu + \mathbf{d}_s$ and $\mathbf{r} - \mathbf{R}_\mu = \mathbf{r}'$ where $\mathbf{R}_\mu$ now denotes the coordinate of the μ-th unit cell where the atom I is found, and $\mathbf{d}_s$ is the coordinate of atom s of the unit cell μ. Thus:

$$\langle\beta_n^I|\psi_{i,\mathbf{k}}^0\rangle = \int d\mathbf{r}\beta_n^s(\mathbf{r}'-\mathbf{d}_s)e^{i\mathbf{kr}'}e^{i\mathbf{kR}_\mu}u_{i,\mathbf{k}}^0(\mathbf{r}') = e^{i\mathbf{kR}_\mu}\langle\beta_n^s|\psi_{i,\mathbf{k}}^0\rangle, \tag{4.11}$$

and

$$\langle\psi_{i,\mathbf{k}}^0|\beta_m^I\rangle = e^{-i\mathbf{kR}_\mu}\langle\psi_{i,\mathbf{k}}^0|\beta_m^s\rangle. \tag{4.12}$$

Now we do the similar operation with the scalar products of the β functions with the response wavefunctions ψ' also expanding it into monochromatic $\mathbf{q}$ components:

$$\begin{aligned}\left\langle\psi_{i,\mathbf{k}}'(-\omega)\,\middle|\,\beta_m^I\right\rangle = \sum_{\mathbf{q}} e^{-i(\mathbf{k}+\mathbf{q})\mathbf{R}_\mu}\int d\mathbf{r}\beta_n^s(\mathbf{r}'-\mathbf{d}_s)e^{-i(\mathbf{k}+\mathbf{q})\mathbf{r}'}u_{i,\mathbf{k}}'^*(\mathbf{r}',-\omega) = \\ \sum_{\mathbf{q}} e^{-i(\mathbf{k}+\mathbf{q})\mathbf{R}_\mu}\left\langle u_{i,\mathbf{k}+\mathbf{q}}'(-\omega)\,\middle|\,e^{-i(\mathbf{k}+\mathbf{q})\mathbf{r}}\,\middle|\,\beta_n^s\right\rangle,\end{aligned} \tag{4.13}$$

and

$$\left\langle\beta_n^I\,\middle|\,\psi_{i,\mathbf{k}}'(\omega)\right\rangle = \sum_{\mathbf{q}} e^{i(\mathbf{k}+\mathbf{q})\mathbf{R}_\mu}\left\langle\beta_n^s\,\middle|\,e^{i(\mathbf{k}+\mathbf{q})\mathbf{r}}\,\middle|\,u_{i,\mathbf{k}+\mathbf{q}}'(\omega)\right\rangle. \tag{4.14}$$

Using these relations and time-reversal symmetry for the unperturbed wavefunction we obtain a final expression for the density response:

$$\begin{aligned}n'(\mathbf{r},\omega)^{\mathbf{q}} = \sum_{i,\mathbf{k}} u_{i,\mathbf{k}}^{(0)*}(\mathbf{r})\left[u_{i,-\mathbf{k}-\mathbf{q}}^*(\mathbf{r},-\omega) + u_{i,\mathbf{k}+\mathbf{q}}(\mathbf{r},\omega)\right] + \sum_{i,\mathbf{k}}\sum_{s,m,n}\widetilde{Q}_{m,n}^{s\mathbf{q}}(\mathbf{r}-\mathbf{d}_s)\times \\ \times\left[< u_{i,-\mathbf{k}-\mathbf{q}}'(-\omega)|e^{i(\mathbf{k}+\mathbf{q})\mathbf{r}}|\beta_m^s >< \beta_n^s|\psi_{i,-\mathbf{k}}^{(0)} > + < \psi_{i,\mathbf{k}}^{(0)}|\beta_m^s > \langle\beta_n^s|e^{i(\mathbf{k}+\mathbf{q})\mathbf{r}}|u_{i,\mathbf{k}+\mathbf{q}}'(\omega)\rangle\right],\end{aligned} \tag{4.15}$$

where

$$e^{i\mathbf{qr}}\widetilde{Q}_{m,n}^{s\mathbf{q}} = \sum_l e^{i\mathbf{qR_l}}Q_{m,n}^s(\mathbf{r}-\mathbf{R_l}-\mathbf{d_s}). \tag{4.16}$$

4.1.3 The Sternheimer equations in the USPP scheme

Making the same assumptions of weak perturbation and linear response approach used in Sec. 1.2.1 to obtain the TDDFT Sternheimer equations we obtain:

$$(\hat{H}^0 - (\varepsilon_{i,\mathbf{k}}^0 + \hbar\omega)\hat{S})\hat{P}_c\psi_{i,\mathbf{k}}'(\mathbf{r},\omega) = -\hat{P}_c^\dagger V'(\mathbf{r},\omega)\psi_{i,\mathbf{k}}^0(\mathbf{r}), \tag{4.17}$$

$$(\hat{H}^0 - (\varepsilon_{i,-\mathbf{k}}^0 - \hbar\omega)\hat{S})\hat{P}_c\psi_{i,\mathbf{k}}'^*(\mathbf{r},-\omega) = -\hat{P}_c^\dagger V'^*(\mathbf{r},-\omega)\psi_{i,\mathbf{k}}^0(\mathbf{r}). \tag{4.18}$$

As in Sec. 1.2.3 in the periodic systems we can write equations (4.17), (4.18) as:

$$(\hat{H}^0 - (\varepsilon^0_{i,\mathbf{k}} + \hbar\omega)\hat{S})\hat{P}_c \sum_{\mathbf{q}} e^{i(\mathbf{k}+\mathbf{q})\mathbf{r}} u'_{i,\mathbf{k}+\mathbf{q}}(\mathbf{r},\omega) = -\hat{P}^{\dagger}_c \sum_{\mathbf{q}} V'_{\mathbf{q}}(\mathbf{r},\omega) e^{i(\mathbf{k}+\mathbf{q})\mathbf{r}} u^0_{i,\mathbf{k}}(\mathbf{r}), \quad (4.19)$$

$$(\hat{H}^0 - (\varepsilon^0_{i,-\mathbf{k}} - \hbar\omega)\hat{S})\hat{P}_c \sum_{\mathbf{q}} e^{-i(-\mathbf{k}+\mathbf{q})\mathbf{r}} u'^{*}_{i,-\mathbf{k}+\mathbf{q}}(\mathbf{r},-\omega) = -\hat{P}^{\dagger}_c \sum_{\mathbf{q}} V'^{*}_{\mathbf{q}}(\mathbf{r},-\omega) e^{i(-\mathbf{k}+\mathbf{q})\mathbf{r}} u^0_{i,\mathbf{k}}(\mathbf{r}), \quad (4.20)$$

While these equation resemble Eq. (1.22), (1.23) the change to the potential $V'(\mathbf{r},\omega)$ on the right-hand side of the equations has more a complicated form [71, 67] because we have to account for the augmentation term:

$$V'_{\mathbf{q}}(\mathbf{r},\omega)e^{i\mathbf{q}\mathbf{r}} = \left[\int d\mathbf{r}' e^{i\mathbf{q}\mathbf{r}'} K(\mathbf{r}') + \int d\mathbf{r}' e^{i\mathbf{q}\mathbf{r}'} V'^{\mathbf{q}}_{H_{xc}}(\mathbf{r}',\omega) K(\mathbf{r}')\right]. \quad (4.21)$$

We start with the first term in parentheses [1] applied to the wavefunction $e^{i\mathbf{k}\mathbf{r}} u^0_{i,\mathbf{k}}(\mathbf{r})$:

$$\int d\mathbf{r}'' \int d\mathbf{r}' e^{i\mathbf{q}\mathbf{r}'} K(\mathbf{r}',\mathbf{r},\mathbf{r}'') e^{i\mathbf{k}\mathbf{r}''} u^0_{i,\mathbf{k}}(\mathbf{r}'') = e^{i\mathbf{q}\mathbf{r}} e^{i\mathbf{k}\mathbf{r}} u^0_{i,\mathbf{k}}(\mathbf{r}) + \sum_{Inm} \int d\mathbf{r}' e^{i\mathbf{q}\mathbf{r}'} Q^I_{m,n}(\mathbf{r}' - \mathbf{d}_s - \mathbf{R}_\mu) \beta^I_m(\mathbf{r} - \mathbf{d}_s - \mathbf{R}_\mu) \left\langle \beta^I_n \middle| \psi^0_{i,\mathbf{k}} \right\rangle. \quad (4.22)$$

Now let us once again pass from the indices I to (μ, s) and make the same variable change as for the charge density:

$$\int d\mathbf{r}'' \int d\mathbf{r}' e^{i\mathbf{q}\mathbf{r}'} K(\mathbf{r}',\mathbf{r},\mathbf{r}'') e^{i\mathbf{k}\mathbf{r}''} u^0_{i,\mathbf{k}}(\mathbf{r}'') = e^{i(\mathbf{k}+\mathbf{q})\mathbf{r}} u^0_{i,\mathbf{k}}(\mathbf{r}) + \sum_{\mu smn} e^{i\mathbf{q}\mathbf{R}_\mu} \int d\mathbf{r}'' e^{i\mathbf{q}\mathbf{r}''} Q^s_{m,n}(\mathbf{r}'' - \mathbf{d}_s) \beta^s_m(\mathbf{r} - \mathbf{d}_s - \mathbf{R}_\mu) e^{i\mathbf{k}\mathbf{R}_\mu} \left\langle \beta^s_n \middle| \psi^0_{i,\mathbf{k}} \right\rangle. \quad (4.23)$$

Note that we can expand $\beta^s_m(\mathbf{r} - \mathbf{d}_s - \mathbf{R}_\mu)$ in Fourier series and reduce the summation over μ to a summation over the reciprocal lattice vectors $\mathbf{G}$:

$$\sum_{\mu} e^{i(\mathbf{q}+\mathbf{k})\mathbf{R}_\mu} \beta^s_m(\mathbf{r} - \mathbf{d}_s - \mathbf{R}_\mu) = e^{i(\mathbf{q}+\mathbf{k})\mathbf{r}} \sum_{\mathbf{G}} \beta^s_m(\mathbf{k} + \mathbf{q} + \mathbf{G}) e^{i\mathbf{G}\mathbf{r}} e^{-i(\mathbf{k}+\mathbf{q}+\mathbf{G})\mathbf{d}_s}. \quad (4.24)$$

Finally, the first term in Eq. (4.21) reads:

$$\int d\mathbf{r}'' \int d\mathbf{r}' e^{i\mathbf{q}\mathbf{r}'} K(\mathbf{r}',\mathbf{r},\mathbf{r}'') e^{i\mathbf{k}\mathbf{r}''} u^0_{i,\mathbf{k}}(\mathbf{r}'') = e^{i(\mathbf{k}+\mathbf{q})\mathbf{r}} u^0_{i,\mathbf{k}}(\mathbf{r}) + \sum_{smn} e^{i\mathbf{q}\mathbf{R}_\mu} I^{(0)s,\mathbf{q}}_{m,n} e^{i(\mathbf{q}+\mathbf{k})\mathbf{r}} \sum_{\mathbf{G}} \beta^s_m(\mathbf{k} + \mathbf{q} + \mathbf{G}) e^{i\mathbf{G}\mathbf{r}} e^{-i(\mathbf{k}+\mathbf{q}+\mathbf{G})\mathbf{d}_s} \left\langle \beta^s_n \middle| \psi^0_{i,\mathbf{k}} \right\rangle, \quad (4.25)$$

where we define $I^{(0)s,\mathbf{q}}_{m,n}$ as:

$$I^{(0)s,\mathbf{q}}_{m,n} = \int e^{i\mathbf{q}\mathbf{r}} Q^s_{m,n}(\mathbf{r} - \mathbf{d}_s) d\mathbf{r}. \quad (4.26)$$

---

[1] Here I am using the coordinate representation of $K(\mathbf{r})$ from Eq. (4.2):$K(\mathbf{r}',\mathbf{r},\mathbf{r}'') = \delta(\mathbf{r} - \mathbf{r}')\delta(\mathbf{r} - \mathbf{r}'') + \sum_{Inm} Q^I_{mn}(\mathbf{r} - \mathbf{R}_I)\beta^I_m(\mathbf{r}' - \mathbf{R}_I)\beta^{I*}_n(\mathbf{r}'' - \mathbf{R}_I)$

The second term in Eq. (4.21) gives the same expression as Eq. (4.25) but with $I^{(0)s,\mathbf{q}}_{m,n}$ replaced by $I^{(3)s,\mathbf{q}}_{m,n}$:

$$I^{(3)s,\mathbf{q}}_{m,n} = \int e^{i\mathbf{qr}} V'^{\mathbf{q}}_{H_{xc}}(\mathbf{r},\omega) Q^s_{m,n}(\mathbf{r}-\mathbf{d}_s) d\mathbf{r}. \tag{4.27}$$

Finally, the TDDFPT Sternheimer equations in the USPP scheme for the lattice periodic components of the response wavefunction take the following form:

$$\begin{aligned}\left[H^{(0)}_{\mathbf{k+q}} - (\varepsilon_{i,\mathbf{k}} + \hbar\omega) S_{\mathbf{k+q}}\right] P_c^{\mathbf{k+q}} u'_{i,\mathbf{k+q}}(\mathbf{r},\omega) = -P_c^{\dagger\mathbf{k+q}} u^{(0)}_{i,\mathbf{k}}(\mathbf{r}) - P_c^{\dagger\mathbf{k+q}} \sum_{s,m,n} (I^{(0)s,\mathbf{q}}_{m,n} + I^{(3)s,\mathbf{q}}_{m,n}) \times \\ \times \sum_{\mathbf{G}} \beta^s_m(\mathbf{k+q+G}) e^{-i(\mathbf{k+q+G})\mathbf{d}_s} e^{i\mathbf{Gr}} < \beta^s_m | \psi^{(0)}_{i,\mathbf{k}} >,\end{aligned} \tag{4.28}$$

$$\begin{aligned}\left[H^{(0)}_{\mathbf{k+q}} - (\varepsilon_{i,\mathbf{k}} - \hbar\omega) S_{\mathbf{k+q}}\right] P_c^{\mathbf{k+q}} u'^{*}_{i,-\mathbf{k}-\mathbf{q}}(\mathbf{r},-\omega) = -P_c^{\dagger\mathbf{k+q}} u^{(0)}_{i,\mathbf{k}}(\mathbf{r}) - P_c^{\dagger\mathbf{k+q}} \sum_{s,m,n} (I^{(0)s,\mathbf{q}}_{m,n} + I^{(3)s,\mathbf{q}}_{m,n}) \times \\ \times \sum_{\mathbf{G}} \beta^s_m(\mathbf{k+q+G}) e^{-i(\mathbf{k+q+G})\mathbf{d}_s} e^{i\mathbf{Gr}} < \beta^s_m | \psi^{(0)}_{i,\mathbf{k}} >,\end{aligned} \tag{4.29}$$

The set of equations (4.28) and (4.29) can be solved self-consistently for each separate value of the frequency ω in order to obtain the electronic susceptibility χ of the system. The use of the USPP scheme introduces additional complexity into the formalism and calculations (i.e. terms that were not present in the NCPP scheme should be computed), however allows to gain performance as a lower value of the kinetic energy cutoff is required.

4.1.4 The quantum Liouville equation in the USPP scheme

I would like to point out that the general form of the quantum Liouville equation in the standard batch representation presented in Sec. 1.2.4 for the NCPP scheme (see Eq. (1.50)) remains similar in the USPP scheme:

$$\begin{pmatrix} \omega & -\hat{\mathcal{D}}^{US}_{\mathbf{q}} \\ -\hat{\mathcal{D}}^{US}_{\mathbf{q}} - 2\hat{\mathcal{K}}^{US}_{\mathbf{q}} & \omega \end{pmatrix} \begin{pmatrix} q_{\mathbf{q}} \\ p_{\mathbf{p}} \end{pmatrix} = \begin{pmatrix} 0 \\ y_{\mathbf{q}} \end{pmatrix}, \tag{4.30}$$

where the action of the operators $\hat{\mathcal{D}}^{US}_{\mathbf{q}}$ and $\hat{\mathcal{K}}^{US}_{\mathbf{q}}$ on the batches are defined as:

$$\hat{\mathcal{D}}^{US}_{\mathbf{q}} \cdot q_{\mathbf{q}} = \left\{ (S^{-1}_{\mathbf{k+q}} \hat{H}^0_{\mathbf{k+q}} - \varepsilon_{i,\mathbf{k}}) \, |q_{i,\mathbf{k+q}}\rangle \right\}, \tag{4.31}$$

and

$$\hat{\mathcal{K}}^{US}_{\mathbf{q}} \cdot q_{\mathbf{q}} = \left\{ S^{-1}_{\mathbf{k+q}} \hat{P}_c^{\dagger\mathbf{k+q}} \left[V'_{Hxc,\mathbf{q}}(\omega) |u^0_{i,\mathbf{k}}\rangle + \sum_{s,mn} I^{(3)s,\mathbf{q}}_{mn}(\omega) \; |\beta^{s,\mathbf{k+q}}_m\rangle\langle\beta^s_m|\psi^0_{i,\mathbf{k}}\rangle \right] \right\} \tag{4.32}$$

while $y_{\mathbf{q}}$ is

$$y_{\mathbf{q}} = \left\{ S^{-1}_{\mathbf{k+q}} \hat{P}_c^{\dagger\mathbf{k+q}} \left[|u^0_{i,\mathbf{k}}\rangle + \sum_{s,mn} I^{(0)s,\mathbf{q}}_{mn} \; |\beta^{s,\mathbf{k+q}}_m\rangle\langle\beta^s_m|\psi^0_{i,\mathbf{k}}\rangle \right] \right\}. \tag{4.33}$$

where the inverse overlap operator $\hat{S}^{-1}$ can be obtained from the condition $\hat{S}\hat{S}^{-1} = 1$ [22].

4.1.5 The fully relativistic case

Finally, I will generalize TDDFPT in the USPP scheme to the fully relativistic (FR) ultrasoft pseudopotentials. The notations I use in this section are largely based on Refs. [69, 70] where DFT and DFPT have been extended to the FR-USPP scheme. Density matrix in this framework becomes the combination of Eqs. (4.1) and (1.60):

$$n^{\sigma,\sigma'}(\mathbf{r},t) = \sum_{i,\mathbf{k},\sigma_1,\sigma_2} \left\langle \psi_{i,\mathbf{k},\sigma_1} \middle| K^{\sigma,\sigma'}_{\sigma_1,\sigma_2}(\mathbf{r}) \middle| \psi_{i,\mathbf{k},\sigma_2} \right\rangle, \tag{4.34}$$

where now the operator $K^{\sigma,\sigma'}_{\sigma_1,\sigma_2}(\mathbf{r})$ is defined through the augmentation functions Q^I_{mn} and projector functions β^I_n as in the SR case, and spin dependent factors $f^{\sigma,\sigma'}_{l,j,m_l;l,j,m'_l}$ are used to write spin-angle functions with spherical harmonics [69]:

$$K^{\sigma,\sigma'}_{\sigma_1,\sigma_2}(\mathbf{r},\mathbf{r}_1,\mathbf{r}_2) = \delta(\mathbf{r}-\mathbf{r}')\delta(\mathbf{r}-\mathbf{r}'')\delta_{\sigma,\sigma_1}\delta_{\sigma,'\sigma_2} + \sum_{Inm}\sum_{In_1m_1} Q^I_{mn}(\mathbf{r}-\mathbf{R}_I) f^{\sigma_1,\sigma}_{m_1,m}\beta^I_{m_1}(\mathbf{r}'-\mathbf{R}_I) f^{\sigma',\sigma_2}_{n_1,n}\beta^{I*}_{n_1}(\mathbf{r}''-\mathbf{R}_I). \tag{4.35}$$

Similarly, the overlap operator $\hat{S}$ becomes spin dependent:

$$S^{\sigma,\sigma'}(\mathbf{r}_1,\mathbf{r}_2) = \sum_{\sigma_1} \int d\mathbf{r} K^{\sigma_1,\sigma_1}_{\sigma,\sigma'}(\mathbf{r},\mathbf{r}_1,\mathbf{r}_2). \tag{4.36}$$

Let us now write the first Sternheimer equation (4.17) for the FR case:

$$\sum_{\sigma'} \left[\hat{H}^{0,\sigma,\sigma'} - (\varepsilon^0_{i,\mathbf{k}} + \hbar\omega)\hat{S}^{\sigma,\sigma'}\right] \hat{P}_c \psi'_{i,\mathbf{k},\sigma'}(\mathbf{r},\omega) = -\hat{P}^\dagger_c \sum_{\sigma'} V'^{\sigma,\sigma'}(\mathbf{r},\omega)\psi^0_{i,\mathbf{k},\sigma'}(\mathbf{r}).,\tag{4.37}$$

Let us make some additional definitions before rewriting this equation:

$$\hat{P}^{\dagger,\sigma_1,\sigma_2}_c = \sum^{unocc}_{i,\mathbf{k}',\sigma_3} \hat{S}^{\sigma_1,\sigma_3} \left|\psi_{i,\mathbf{k}',\sigma_3}\right\rangle \left\langle\psi_{i,\mathbf{k}',\sigma_2}\right|, \tag{4.38}$$

and $\hat{\Pi}_c = T\hat{P}_cT^\dagger$:

$$\hat{\Pi}^{\sigma_1,\sigma_2}_c = \sum^{unocc}_{i,\mathbf{k}',\sigma_3} \hat{S}^{\sigma_1,\sigma_3} \left|T\psi_{i,\mathbf{k}',\sigma_3}\right\rangle \left\langle T\psi_{i,\mathbf{k}',\sigma_2}\right|, \tag{4.39}$$

where T is the time reversal operator as in Eq. (1.62). Now, using this definitions we can write Eq. (4.37) and its time-reversal counterpart as:

$$\sum_{\sigma'} \left[\hat{H}^{0,\sigma,\sigma'} - (\varepsilon^0_{i,\mathbf{k}} + \hbar\omega)\hat{S}^{\sigma,\sigma'}\right] \left(\hat{P}_c\psi'_{i,\mathbf{k}}(\mathbf{r},\omega)\right)_{\sigma'} = -\sum_{\sigma_2,\sigma'} \hat{P}^{\dagger,\sigma,\sigma_2}_c V'^{\sigma_2,\sigma'}(\mathbf{r},\omega)\psi^0_{i,\mathbf{k},\sigma'}(\mathbf{r}), \tag{4.40}$$

$$\sum_{\sigma'} \left[\hat{H}^{0,\sigma,\sigma'} - (\varepsilon^0_{i,\mathbf{k}} - \hbar\omega)\hat{S}^{\sigma,\sigma'}\right] \left(\hat{\Pi}_c T\psi'_{i,\mathbf{k}}(\mathbf{r},-\omega)\right)_{\sigma'} = -\sum_{\sigma_2,\sigma'} \hat{\Pi}^{\dagger,\sigma,\sigma_2}_c \left(TV'^{\sigma_2,\sigma'}(\mathbf{r},-\omega)\psi^0_{i,\mathbf{k}}(\mathbf{r})\right)_{\sigma'}, \tag{4.41}$$

and the electron density response reads:

$$n'(\mathbf{r},\omega) = \sum_{i,\mathbf{k},\sigma,\sigma_1,\sigma_2} \left[\left\langle \left(T\psi^0_{i,\mathbf{k}}\right)_{\sigma_1} \middle| K^{\sigma,\sigma}_{\sigma_1,\sigma_2}(\mathbf{r}) \middle| \left(\hat{\Pi}_c T\psi'_{i,\mathbf{k}}(-\omega)\right)_{\sigma_2} \right\rangle + \left\langle \psi^0_{i,\mathbf{k},\sigma_1} \middle| K^{\sigma,\sigma}_{\sigma_1,\sigma_2}(\mathbf{r}) \middle| \hat{P}_c\psi'_{i,\mathbf{k},\sigma_2}(\omega) \right\rangle\right]. \tag{4.42}$$

Now, we can rewrite these equations only for lattice periodic parts of the response wavefunctions and density, defining as in Sec. 1.2.3 $\mathbf{k}+\mathbf{q}$ components of all operators starting with the density:

$$n'(\mathbf{r},\omega)^{\mathbf{q}} = \sum_{i,\mathbf{k},\sigma,\sigma_1,\sigma_2} \Bigg[\left\langle \left(Tu^0_{i,-\mathbf{k}}\right)_{\sigma_1} \middle| e^{-i\mathbf{k}\mathbf{r_1}} K^{\sigma,\sigma}_{\sigma_1,\sigma_2}(\mathbf{r}) e^{i(\mathbf{k}+\mathbf{q})\mathbf{r_2}} \middle| \left(\hat{\Pi}_c^{-\mathbf{k}-\mathbf{q}} T u'_{i,-\mathbf{k}-\mathbf{q}}(-\omega)\right)_{\sigma_2} \right\rangle \\ + \left\langle u^0_{i,\mathbf{k},\sigma_1} \middle| e^{-i\mathbf{k}\mathbf{r_1}} K^{\sigma,\sigma}_{\sigma_1,\sigma_2}(\mathbf{r}) e^{i(\mathbf{k}+\mathbf{q})\mathbf{r_2}} \middle| \hat{P}_c^{\mathbf{k}+\mathbf{q}} u'_{i,\mathbf{k}+\mathbf{q},\sigma_2}(\omega) \right\rangle \Bigg], \quad (4.43)$$

or, if we recall the time-reversal symmetry for the unperturbed wavefunctions:

$$n'(\mathbf{r},\omega)^{\mathbf{q}} = \sum_{i,\mathbf{k},\sigma,\sigma_1,\sigma_2} \left\langle u^0_{i,\mathbf{k},\sigma_1} \right| e^{-i\mathbf{k}\mathbf{r_1}} K^{\sigma,\sigma}_{\sigma_1,\sigma_2}(\mathbf{r}) e^{i(\mathbf{k}+\mathbf{q})\mathbf{r_2}} \\ \left| \left(\hat{\Pi}_c^{-\mathbf{k}-\mathbf{q}} T u'_{i,-\mathbf{k}-\mathbf{q}}(-\omega)\right)_{\sigma_2} + \hat{P}_c^{\mathbf{k}+\mathbf{q}} u'_{i,\mathbf{k}+\mathbf{q},\sigma_2}(\omega) \right\rangle. \quad (4.44)$$

Finally, we can write the Sternheimer equations as:

$$\sum_{\sigma'} \left[\hat{H}^{0,\sigma,\sigma'}_{\mathbf{k}+\mathbf{q}} - (\varepsilon^0_{i,\mathbf{k}} + \hbar\omega)\hat{S}^{\sigma,\sigma'}_{\mathbf{k}+\mathbf{q}}\right] \left(\hat{P}_c^{\mathbf{k}+\mathbf{q}} u'_{i,\mathbf{k}+\mathbf{q}}(\mathbf{r},\omega)\right)_{\sigma'} = \\ - \sum_{\sigma_2,\sigma'} \hat{P}_c^{\dagger,\sigma,\sigma_2,\mathbf{k}+\mathbf{q}} e^{-i(\mathbf{k}+\mathbf{q})\mathbf{r}} V'^{\sigma_2,\sigma'}(\mathbf{r},\omega) e^{i\mathbf{k}\mathbf{r}} u^0_{i,\mathbf{k},\sigma'}(\mathbf{r}), \quad (4.45)$$

$$\sum_{\sigma'} \left[\hat{H}^{0,\sigma,\sigma'}_{\mathbf{k}+\mathbf{q}} - (\varepsilon^0_{i,-\mathbf{k}} - \hbar\omega)\hat{S}^{\sigma,\sigma'}_{\mathbf{k}+\mathbf{q}}\right] \left(\hat{\Pi}_c^{-\mathbf{k}-\mathbf{q}} T u'_{i,-\mathbf{k}-\mathbf{q}}(\mathbf{r},-\omega)\right)_{\sigma'} = \\ - \sum_{\sigma_2,\sigma'} \hat{\Pi}_c^{\dagger,\sigma,\sigma_2,-\mathbf{k}-\mathbf{q}} e^{-i(\mathbf{k}+\mathbf{q})\mathbf{r}} V'^{\sigma_2,\sigma'}(\mathbf{r},\omega) e^{i\mathbf{k}\mathbf{r}} \left(Tu^0_{i,-\mathbf{k}}(\mathbf{r})\right)_{\sigma'}. \quad (4.46)$$

We can transform Eqs. (4.45) and (4.46) into the final set of equations using time-reversal symmetry:

$$\sum_{\sigma'} \left[\hat{H}^{0,\sigma,\sigma'}_{\mathbf{k}+\mathbf{q}} - (\varepsilon^0_{i,\mathbf{k}} + \hbar\omega)\hat{S}^{\sigma,\sigma'}_{\mathbf{k}+\mathbf{q}}\right] \left(\hat{P}_c^{\mathbf{k}+\mathbf{q}} u'_{i,\mathbf{k}+\mathbf{q}}(\mathbf{r},\omega)\right)_{\sigma'} = \\ - \sum_{\sigma_2,\sigma'} \hat{P}_c^{\dagger,\sigma,\sigma_2,\mathbf{k}+\mathbf{q}} e^{-i(\mathbf{k}+\mathbf{q})\mathbf{r}} V'^{\sigma_2,\sigma'}(\mathbf{r},\omega) e^{i\mathbf{k}\mathbf{r}} u^0_{i,\mathbf{k},\sigma'}(\mathbf{r}), \quad (4.47)$$

$$\sum_{\sigma'} \left[\hat{H}^{0,\sigma,\sigma'}_{\mathbf{k}+\mathbf{q}} - (\varepsilon^0_{i,\mathbf{k}} - \hbar\omega)\hat{S}^{\sigma,\sigma'}_{\mathbf{k}+\mathbf{q}}\right] \left(\hat{P}_c^{\mathbf{k}+\mathbf{q}} T u'_{i,-\mathbf{k}-\mathbf{q}}(\mathbf{r},-\omega)\right)_{\sigma'} = \\ - \sum_{\sigma_2,\sigma'} \hat{P}_c^{\dagger,\sigma,\sigma_2,\mathbf{k}+\mathbf{q}} e^{-i(\mathbf{k}+\mathbf{q})\mathbf{r}} V'^{\sigma_2,\sigma'}(\mathbf{r},\omega) e^{i\mathbf{k}\mathbf{r}} u^0_{i,\mathbf{k},\sigma'}(\mathbf{r}), \quad (4.48)$$

In order to compute the response potential $V'^{\sigma_2,\sigma'}(\mathbf{r},\omega)$ on the right hand side of these equations the same strategy is used as in Sec. 4.1.1 for Eq. (4.21) for each spin index pair σ_2,σ'. I note that these equations can be reduced to the equations of the NCPP scheme by taking the augmentation part equal to zero. Similarly one can also reduce them to the scalar relativistic case.

Like before, the set of the Sternheimer equations (4.47) and (4.48) can be solved self-consistently for each value of the frequency ω in order to obtain the susceptibility χ. They also can be rewritten in the form of the quantum Liouville equation (see Sec. 4.1.4) in a straightforward way. I note, however, that in the FR USPP scheme, the inverse of the overlap operator $\hat{S}^{-1}$ in Eq. (4.31) and (4.31) becomes also spin dependent, adding more complexity to its evaluation. The full derivation of the $\hat{S}^{-1}$ operator in the FR case will be given elsewhere in future publications.

4.2 Comparison of the Sternheimer and Liouville-Lanczos approaches

The Liouville-Lanczos recursive scheme has been implemented in the *turboEELS* code of the TDDFPT branch of the Quantum ESPRESSO suite [21, 22, 23, 24, 25, 26] prior to this work for FR and SR NCPP schemes (see Chapter 1) and for SR USPP scheme (see Sec. 4.1.1, 4.1.4 of this chapter). However, the latter was not working efficiently: I have made several modifications that allowed to (1) fix a problem that would have led to incorrect results for unit cells containing more than two atoms and (2) gain overall performance by removing some redundant operations.

4.2.1 Comparison of EEL spectra calculated with *turboEELS* and *thermo_pw* codes

In this section I would like to present a performance comparison for EEL spectrum calculations using Sternheimer (as implemented in *thermo_pw* code version 0.6.0) and Liouville-Lanczos (as implemented in *turboEELS* code of Quantum ESPRESSO version 6.0) approaches. The codes were tested for bulk bismuth because previous calculations are available [74] and for bulk gold for which numerous studies are available (see Chapter 3) and which I have studied in Chapter 6.

In figure 4.1, I report EEL spectra for bulk Bi obtained both with the *thermo_pw* code, and with *turboEELS*: results are in perfect agreement with each other and with previous calculations [74], both with and without SOC. We point out that the TDDFPT calculations were performed with, as input, data coming from the same (DFT) ground state self-consistent calculation.

Figure 4.2 shows the comparison of the EEL spectra for bulk Au obtained by *thermo_pw* and *turboEELS* codes. Obtained results are in agreement with previous ab initio calculations of the EELS for Au [52]. In figure 4.2 one can see a severely damped plasmon peak around 2.5 eV and numerous interband transition at higher energies. Spectrum for Au will be discussed in Chapter 6. In this section I focus solely on the performance.

Figure 4.3 shows the relative difference between EEL spectra computed with the *thermo_pw* and *turboEELS* codes. Beyond 2 eV the agreement is perfect and the two codes agree within 1%. Below 2 eV, the loss function is tending to 0 and the magnitude of the relative difference becomes higher as the loss function does not tend to 0 in the same way. Indeed, oscillations that are intrinsic to the Lanczos approach are magnified in the difference at low energy. As in the case of Bi, agreement is perfect, that indicates that both codes are well-suited to handle either semimetallic or metallic materials.

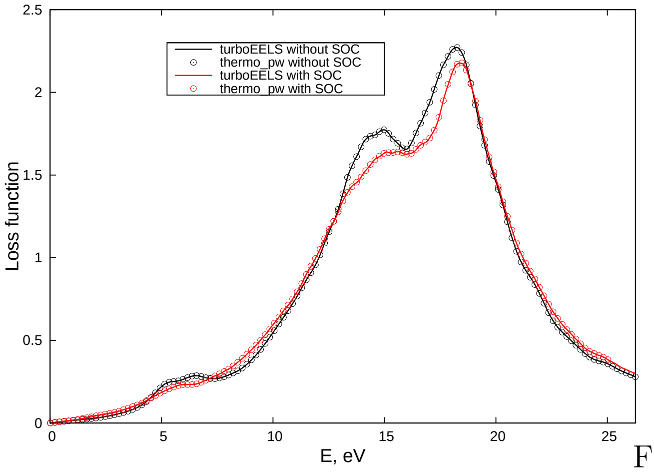

Figure 4.1: Bulk Bi. Loss function for a transferred momentum $\mathbf{q} = 0.013\ \text{Å}^{-1}$ in the z-direction obtained using: *turboEELS* code withoutand with spin-orbit coupling (SOC), and *thermo_pw* code without and with SOC.

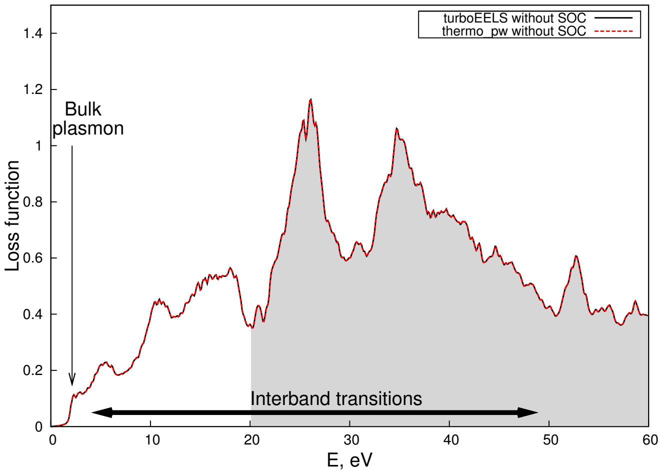

Figure 4.2: Bulk Au. Loss function for a vanishing transferred momentum is the x-direction, calculated with the *turboEELS* code and *thermo_pw* code. Shaded area marks the energy region where our pseudopotential is less accurate and arrows indicate the position of the bulk plasmon and the region on interband transitions.

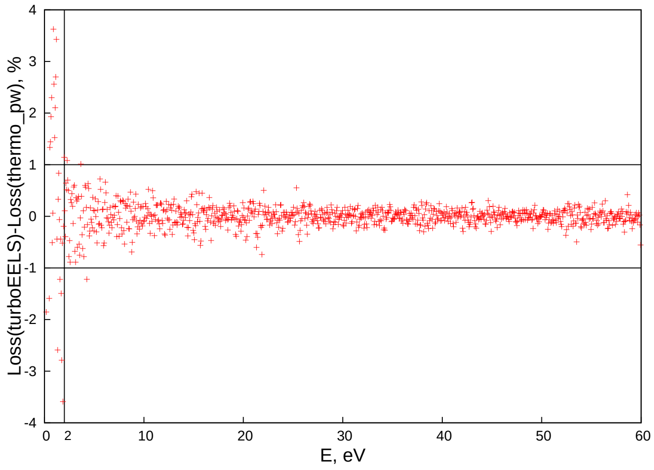

Figure 4.3: Bulk Au. Relative difference between the loss functions computed for a vanishing transferred momentum is the x-direction, calculated with the *turboEELS* and *thermo_pw* codes.

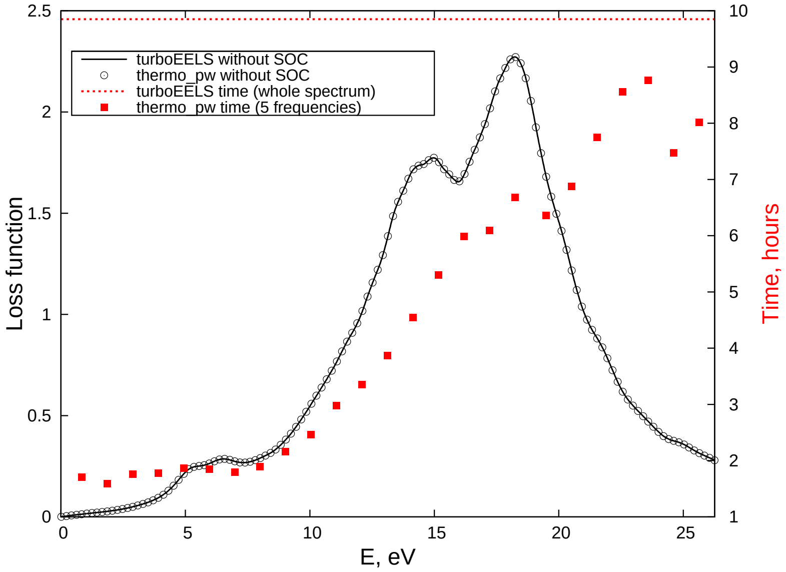

Figure 4.4: Bulk Bi. Performance comparison of *turboEELS* and *thermo_pw* codes without spin-orbit coupling. Loss functions obtained with *turboEELS* and *thermo_pw* codes are shown (left-hand side abscissa). Time required for *turboEELS* to compute the whole spectrum and for *thermo_pw* to compute the loss function for five frequencies in the corresponding frequency range is shown (right-hand side ordinate).

4.2.2 Performance comparison

In figure 4.4, we show the comparison of the performance of both codes in terms of CPU time for bulk Bi without SOC. One can see that the *turboEELS* code is more efficient than the *thermo_pw* code on a wide frequency range. We note that calculations in a low frequency region (0-10 eV) are considerably faster, by a factor of 2-3, than in the middle and high frequency region (10-30 eV).

In table 4.1, we show the amount of time, number of CPU cores and number of frequencies used to obtain curves in fig. 4.2 and 4.4. In the last column of table 4.1, the number of frequency is given, showing on average how many frequencies can be calculated with *thermo_pw* when consuming the same amount of CPU time needed for *turboEELS* to calculate the whole spectra. We point out that the *ratio* may however depend on the selected frequency range.

Performance comparison for the calculation with SOC is not shown in the present work. Taking SOC into account roughly increases the required CPU time by a factor of 4 for both codes, without influencing their relative performance.

I have done a comparison between results and performance of the codes and of the corresponding methods that allow us to calculate EEL spectra. It has been found that results obtained using the Sternheimer equation and the Liouville-Lanczos approach are in perfect agreement with each other for semiconducting (not shown), semimetallic and metallic samples. However, as anticipated, the performance of the Liouville-Lanczos method as implemented in the *turboEELS* code is significantly better when the range of frequencies is wide. In principle it is possible to calculate EEL spectra on a 0-250 eV range at the

Table 4.1: Performance comparison of the *turboEELS* and *thermo_pw* codes for bulk Bi and Au.

System	# of CPU cores	# of frequencies (ω)	Time (h)	average # of ω for *thermo_pw* match *turboEELS* CPU time
Bi *turboEELS*	72	any	10	
Bi *thermo_pw*	72	130	118	11
Au *turboEELS*	240	any	0.75	
Au *thermo_pw*	240	600	16	28

same computational cost as on the 0-25 eV interval, although it might be necessary to include core electrons in the pseudopotential in order to describe high-energy excitations correctly. One can see that it is convenient to use the *thermo_pw* code for a precise calculation of the susceptibility in a narrow frequency range. I note that after obtaining the results reported in this section additional level of the parallelization of the Sternheimer approach calculation was implemented by Andrea Dal Corso that allowed to enhance its performance (not shown in this work).

4.2.3 Testing of the Liouville-Lanczos algorithm in a high performance computing environment

During the second year of the PhD I have been doing extensive performance and scaling testing of the *turboEELS* in the preparation of a PRACE project submission. In this paragraph I will give a brief summary of these results. Tests were performed on the CURIE machine of the CEA-TGCC in the frame of the PRACE preparatory access project.

4.2.3.a Strong scaling

First I have tested the strong scaling of the code that defines how the solution time varies with the number of processors for a fixed total problem size. The strong scaling properties of the turboEELS code were tested on a 16 layer slab of the (111) Au surface with a 8-nm-size vacuum. Calculation have been performed using 102 $\mathbf{k}$-points to sample the Brillouin zone in the self-consistent field (SCF) calculation, to obtain the ground state total energy, density and self-consistent Kohn-Sham potential. The $\mathbf{k}$-point grid was unfolded with symmetry operation for the non self-consistent (NSCF) calculation, in which properties are computed both for $\mathbf{k}$ and $\mathbf{k}+\mathbf{q}$ points. The number of $\mathbf{k}$ (and $\mathbf{k}+\mathbf{q}$) amounted to 1056 points in the NSCF calculations. The turboEELS code was then ran with the 1056 points, and its performance is presented in the Table 4.2 and Fig. 4.5. Calculations were parallelized on the $\mathbf{k}$ points and on the plane-waves. The fast-Fourier transform (FFT) used to go back and forth from real space to the reciprocal (dual) space, was performed on the same number of cores (10 cores for each pool of k-points). As one can see in the table, the code scales rather well up to 1020 cores, even though the examined system was a rather small one, and consisted in 16 atoms in a unit cell. Such a behavior is general for *turboEELS*.

# of cores	absolute timing (s)	speedup
170	3060	1
340	1626	1.88
510	1149	2.66
1020	660	4.63

Table 4.2: Strong scaling properties of the *turboEELS* code.

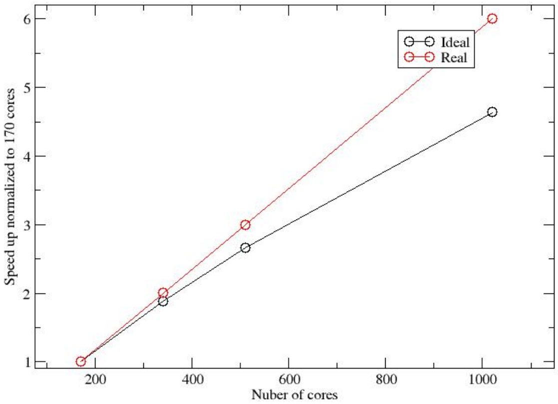

Figure 4.5: Strong scaling properties of the *turboEELS* code. Black line shows the real scaling and red line shows the ideal linear scaling.

4.2.3.b Weak scaling

The following table and figure show the weak scaling of the *turboEELS* code. In this test the size of the system was increased (in this case the number of layers and thus number of electrons and size of the supercell) along with the number of cores on which calculations were performed, keeping the workload of a single core practically the same. When adding electrons to the system, the time required to perform the calculation in proportional to $N_v * N_{pw} * ln(N_{pw})$, where N_v is the number of bands and N_{pw} is the number of plane-waves.

In the Table 4.3 the column "theoretical core # ratio " shows the theoretical multiplicator of the number of cores used for 3 layers that should be use to keep the core workload the same while increasing the number of layers. Due to the code specificity this number cannot be fulfilled exactly, thus the closest possible numbers were selected (column "real ratio") and final timing has been renormalized with respect to the real and theoretical ration. From the Table 4.3 and Figure 4.6 one can see that the *turboEELS* code is very efficient in terms of strong scaling. In fact, one can see that the performance on the bigger systems is better than on the smallest one. This arises from the fact that performing FFT on 10 cores is more efficient for big systems, while for small systems this number should be decreased. It the present tests this number was fixed in order to keep the results as coherent as possible.

# of layers	N_{pw}	*turboEELS* timing, s	# of cores	theoretical core # ratio	real ratio	renormalized timing
3	2071	1284	20	1.00	1.0	1284
6	4141	1037	90	4.36	4.5	1070
12	8281	1158	400	18.9	20	1226

Table 4.3: Weak scaling properties of the *turboEELS* code.

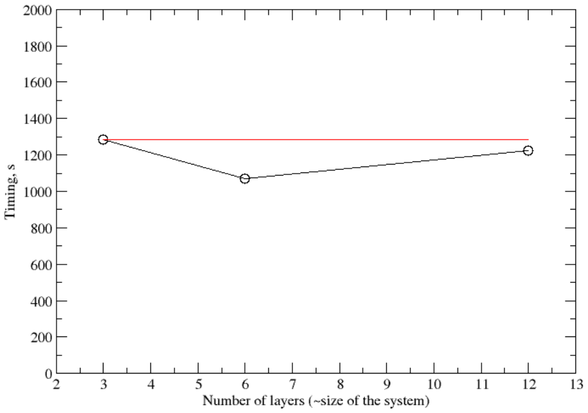

Figure 4.6: Weak scaling properties of the *turboEELS* code. Black line shows the real scaling and red line shows the ideal linear scaling.

4.2.4 Implementation

On view of the good results of this section the Liouville-Lanczos approach was implemented in the *thermo_pw* code by Andrea Dal Corso. Then also the generalization of TDDFPT to the FR USPP scheme (Sec. 4.1.5) has been implemented by Andrea Dal Corso for both Liouville-Lanczos recursive and Sternheimer self-consistent approaches. I have thoroughly tested this implementation and made modifications that allowed to restart the Liouville-Lanczos calculation if it was interrupted from the save point or from the successful calculation in order to perform more iterations. Other modification allows to perform the response calculation in a random-phase approximation (RPA) without crystal local field effects. As the Liouville-Lanczos approach implementation in *thermo_pw* has proven to be more about 20-25% faster than its implementation in *turboEELS* code I have been using it during the last year of my PhD.

4.3 Conclusions

In this chapter I have presented the TDDFPT in scalar relativistic ultrasoft pseudopotential scheme and, for the first time, the generalization of TDDFPT to the fully relativistic ultrasoft pseudopotential scheme. The methodological development of Sec. 4.1.5 led to the very efficient implementations of both the Sternheimer and Liouville-Lanczos approaches to the solution of the linear response problem and thus computation of the susceptibility of the systems where spin-orbit coupling should be accounted for and high kinetic energy cutoffs might not be affordable, like surfaces. In perspective this can be generalized further to the magnetic excitations in the FR USPP scheme to allow magnon calculations. Other directions include the generalization to PAW scheme and going beyond the linear response framework in order to include non-linear effects. Finally, the development and implementation of TDDFPT+U approach [75] should prove useful for the application to materials where LDA/GGA gives a poor description of strongly correlated localized electron states.

Last but not least, I have studied the performance of the Liouville-Lanczos and the Sternheimer approaches and scaling of the Liouville-Lanczos approach in a HPC environment. I have shown that their Liouville-Lanczos approach is indeed fast compared to the Sternheimer approach and is perfectly suited for the simulation of large system in a HPC environment judging from its scaling properties. Together it makes the Liouville-Lanczos approach the best available method for the simulations of EEL spectra for periodic systems containing hundreds of atoms like vicinal Au surfaces for which I have obtained 15 million core hours on the JUWELS cluster (Jülich Supercomputing Centre, Germany) in the framework of 16-th PRACE project access call “Acoustic surface plasmon in vicinal Au surfaces from first principle electron energy loss spectra simulations” .

Chapter 5

Ab initio calculations of the surface band structure and of the surface states of vicinal Au(111)

In this chapter I show the results of *ab initio* calculations of the surface band structure and the surface states for stepped Au(111) surfaces: Au(322), Au(455) and Au(788). First, I discuss the phenomenon of the band gap closure at the $\overline{\Gamma}$-point, at the Fermi level, depending on the miscut angle and I show, through the calculation of the band structure for bulk Au, the evolution of the gap at the $\overline{\Gamma}$-point for the stepped surface. Then I discuss and explain the refolding of the band structure for stepped surfaces through the refolding of the band structure for the supercell of Au(111) and difficulties that arise from the refolding. Finally, I show the results of the surface state calculations for Au(322), Au(455) and Au(788) and discuss the evolution of the surface states as a function of the terrace width and miscut angle.

5.1 Methodology for the study of surface states of vicinal surfaces

In Sec. 2.2.2 I have shown how the surface states look like for the Au(111) surface: it consists of the surface band structure on top of the projected bulk band structure (PBS) and states that meet a given localization criterion for the square modulus of the Kohn-Sham wavefunctions $|\psi|^2 > 0.6$ on the two topmost surface layers. This procedure can be tentatively separated into three steps:

1. Obtain the PBS of the surface and its band structure.

2. In the band structure, identify states that meet the selected localization criterion.

3. Locate the position of the localized states with respect to the gaps in the PBS in order to make a surface state/surface resonance assignment.

This procedure is straightforward for Au(111) or similar simple surfaces. In fact this procedure is well automatized in the thermo_pw module [76] for the Quantum ESPRESSO suite [31, 32].

Unfortunately, this procedure is not as straightforward for the vicinal surfaces due to the refolding of the band structure of the vicinal surfaces that complicates the obtainment of the PBS and band structure as well as the precise location of the localized states in the PBS gaps. In this Section I will discuss the possible solutions and workarounds for this problem.

5.1.1 Band structure refolding for supercells and superlattices of Au(111) vicinal surfaces

As I have introduced in Section 2.3, vicinal surfaces of Au(111) form a kind of superlattice with an orthorombic unit cell. The unit cell consists of a certain number (m) of Au(111) rows along the x-direction and of a monoatomic step along the y-direction. From the viewpoint of the unit cell and Brillouin zone geometry it looks similar to the supercell of the Au(111) surface in the orthorhombic geometry elongated along y, like it is shown in Fig. 5.1. This will have a twofold influence of the SBZ: first, it will have a rectangular form instead of the hexagonal form of the standard unit cell of Au(111) and second, the dimension of the SBZ in the y direction will be approximately m times smaller than the dimension in the x direction or than the dimensions of the SBZ of the hexagonal primitive cell of Au(111).

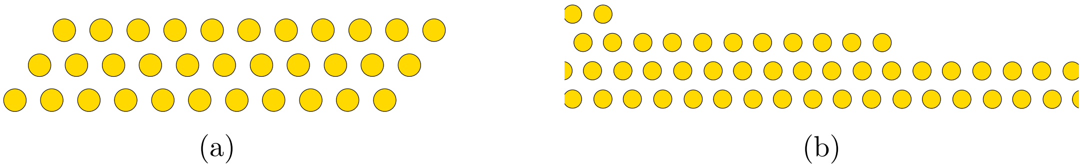
(a) (b)

Figure 5.1: Side view of the surface structure of (a) the Au(111) surface and (b) the Au(455) surface.

Obtaining the *ab initio* band structure of the vicinal surface similar to the band structure of the Au(111) surface shown in Fig. 2.3 is not straightforward: first, the shape of the SBZ is different, thus it is not possible to calculate band structure along the same path. Second, the narrowing of the SBZ leads to the refolding of the bands of the primitive cell SBZ into the smaller SBZ of the supercell. In Fig. 5.2 I show three different SBZ plotted on the same scale: the hexagon is the SBZ of hexagonal primitive cell of Au(111) (see also Sec. 2.1), the big rectangle is the SBZ of Au(111) in the orthorhombic geometry and the smaller rectangle is the SBZ of the Au(455) surface. Let us first consider the simplest case of the band structure of Au(111) in the supercell with the orthorhombic geometry. In this case the length of the $\overline{\Gamma}-\overline{M'}$ path in the SBZ of the primitive cell is twice the length of the $\overline{\Gamma}-\overline{Y}$ path in the SBZ of the supercell - as a result the band structure calculated in the supercell along the $\overline{\Gamma}-\overline{Y}$ path will be twice folded along the $\overline{\Gamma}-\overline{M'}$ path and the $\overline{M'}$ point refolded at the $\overline{\Gamma}$ point of the supercell SBZ. Similarly, supercell band structure calculated along the $\overline{\Gamma}-\overline{X}$ path will contain bands along the $\overline{\Gamma}-\overline{M}$ path in the SBZ of the primitive cell and along the $\overline{M'} - \overline{K'}$ path that will refold along this direction in the SBZ of the supercell. A similar reasoning can be applied to other paths and points in SBZ of supercell and primitive cell. Analogically, when one increases the length of the supercell along x, the width of the rectangular SBZ will decrease, leading to the increase of the band structure refolding factor[1]. For the above discussed Au(111) supercell in the orthorhombic geometry the refolding factor is equal to 2 as the length of the $\overline{\Gamma} - \overline{M'}$ path in the SBZ of the primitive cell is twice the length of the $\overline{\Gamma} - \overline{Y}$ path in the SBZ of the supercell (Fig 5.2).

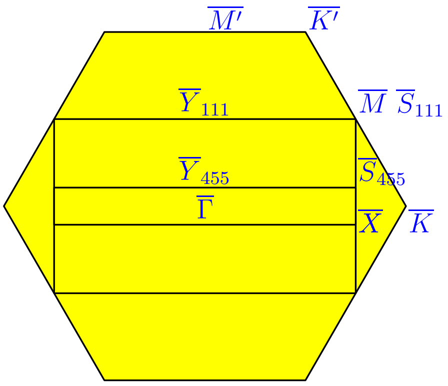

Figure 5.2: SBZ of the hexagonal primitive cell and orthorhombic supercell of Au(111) and Au(455).

Result of the direct band structure calculation for Au(111) in the supercell with the orthorhombic geometry is shown in Fig. 5.3. Here one can readily observe the results of the refolding of the band structure: for instance at the $\overline{\Gamma}$ point of the SBZ of the primitive cell there is a wide gap spanning between -1.1 eV $< E <$ 3.1 eV (see Fig. 2.3) - instead in Fig. 5.3 we see at the Fermi level some bands that used to be at the $\overline{M}$ point of the primitive cell SBZ in Fig. 2.3. In the present case the exact supercell of Au(111) was used thus allowing to perform unfolding of the band structure using the state-of-the-art bandUP code [77, 78]. Result of the band structure calculation performed along the special path in the supercell SBZ and unfolded along the $\overline{K} - \overline{\Gamma} - \overline{M}$ path in the SBZ of the primitive cell is shown in Fig. 5.4. I point out that despite the refolding of the band structure it is still possible to identify the surface states from the direct band structure calculation for the supercell, as it is shown in Fig. 5.3 with blue dots.

Now, let us consider vicinal surfaces of Au(111) and the corresponding *ab initio* band structure calculations. As I have already discussed in the Chapter 2 a vicinal surface of Au(111) consists of flat (111) terraces separated with monoatomic steps and has the orthorombic unit cell with the rectangular SBZ shown in Fig. 5.2. Consequently, the band structure of such a surface will be refolded in a way similar to the refolding of the bands for Au(111) in the orthorhombic geometry with a refolding factor that will depend on the terrace width. Unfortunately, the straightforward unfolding of the bands

---

[1] The refolding factor is defined as the ratio between the primitive cell SBZ dimension and the supercell SBZ dimension.

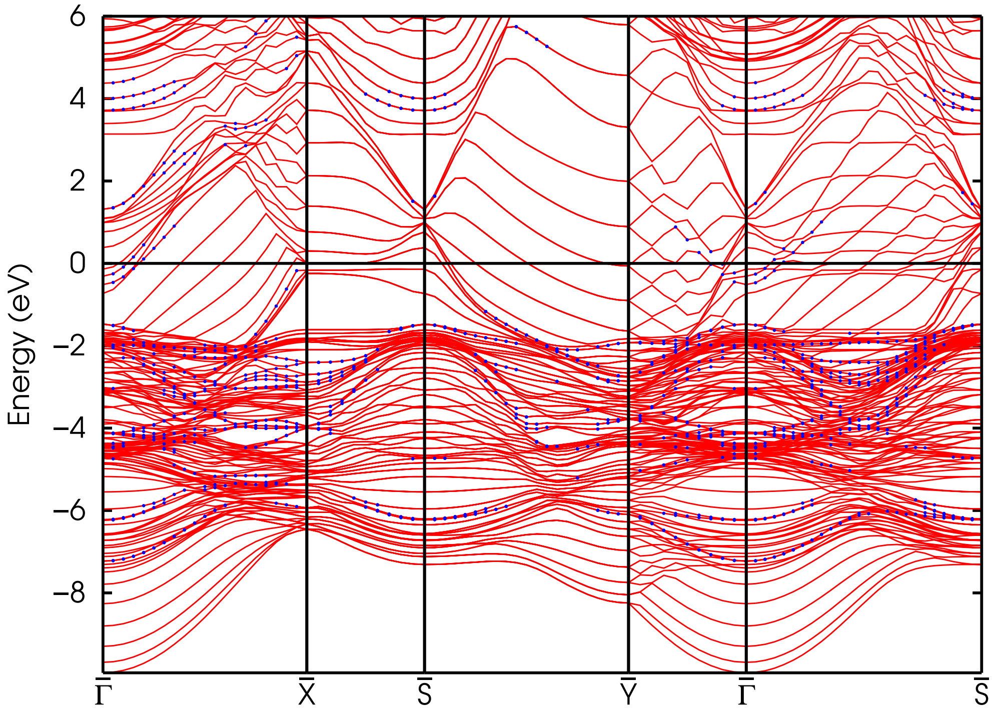

Figure 5.3: Band structure of 10 layers of Au(111) in the orthorhombic geometry calculated without SOC. Blue dots are surface states identified with the localization criterion of $|\psi|^2 > 0.6$ on the two topmost surface layers.

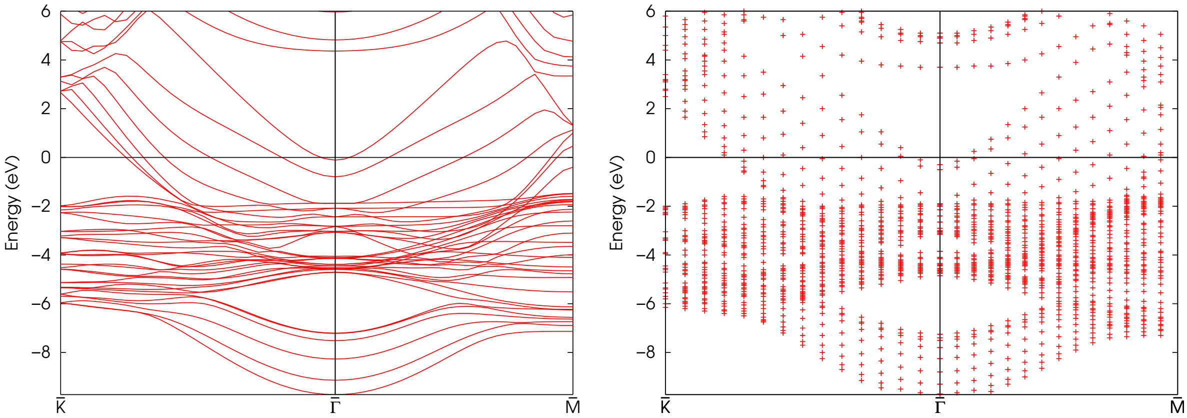

(a) (b)

Figure 5.4: (a) Band structure of 10 layers Au(111) calculated along the $\overline{K}-\overline{\Gamma}-\overline{M}$ path (b) band structure of 10 layers Au(111) in the orthorhombic supercell geometry calculated along the special path in the SBZ of the supercell and unfolded on the $\overline{K}-\overline{\Gamma}-\overline{M}$ path of the SBZ of the primitive cell. Unfolding was performed using the bandUP code [77, 78].

for vicinal surfaces in the way it has been done for the Au(111) supercell, is not possible. In order to utilize the unfolding procedure performed for the supercell of Au(111) it is required that the supercell is commensurate with the primitive cell - a requirement that cannot be fulfilled due to the non-zero miscut angle between the vicinal and (111) surfaces. Nevertheless, analysis of the band structure refolding for the Au(111) supercell gives a general idea of the character of the band structure refolding that will apply as well for the vicinal surfaces, as its unit cell and SBZ have the same shape as the Au(111) supercell. In Fig. 5.5 I show the results of the band structure calculation for the Au(455) surface. One can see that it indeed resembles the band structure for the Au(111) supercell shown in Fig. 5.3 - for instance, there is a band gap below the Fermi level around $\overline{X}$ and $\overline{S}$ special points in both band structures. However, due to the refolding factor that is about 9 for Au(455) compared to 2 for Au(111), a more detailed band structure analysis is impossible without the unfolding. On the other hand, my main interest lies in the L-gap derived surface state that can be identified and studied from the refolded band structure calculation, complemented with the bulk band structure calculations that allow the identification of the band gap at the Fermi level of the vicinal surface.

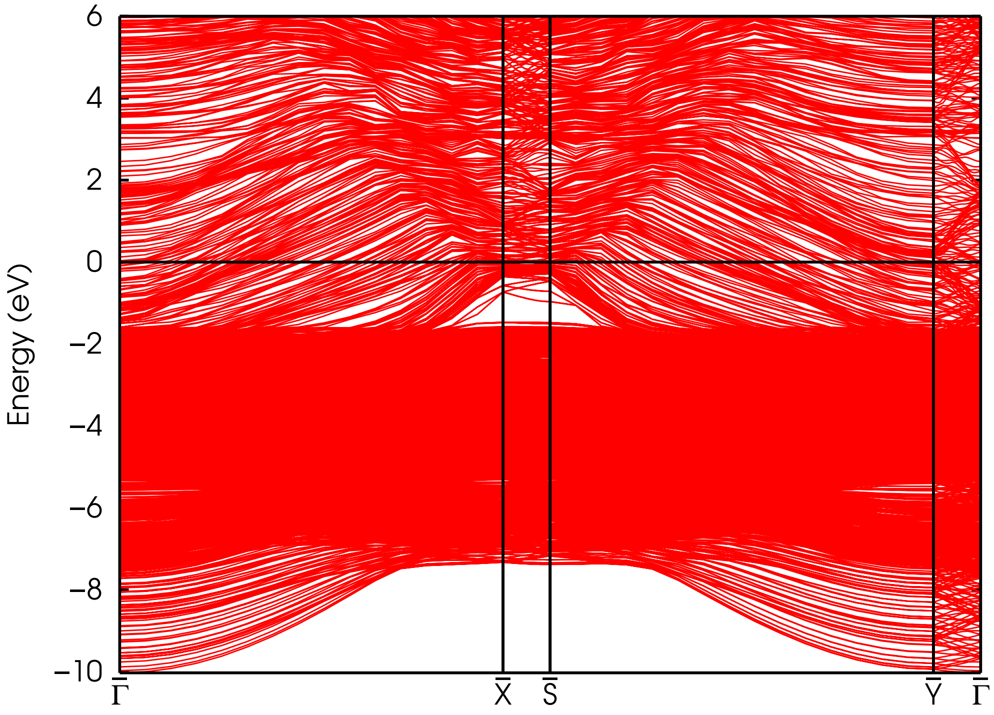

Figure 5.5: Band structure of the Au(455) surface. Direct calculation.

5.1.2 Gap in the projected bulk band structure for flat and stepped Au(111)

In Sections 2.2.2 and 2.3 I have already discussed briefly the gap in the projected bulk band structure (PBS) at the Fermi level of the surface Brillouin zone (SBZ) center, for both flat and stepped Au(111) surfaces. In the present section I discuss the gap in the PBS as a function of the miscut angle α. Due to the refolding of the band structure discussed in the previous section, the PBS of the vicinal surface cannot be routinely obtained in the manner it was done for the Au(111) surface in Fig. 2.3 using the thermo_pw code, however it is still possible to analyze it for the selected point in the SBZ.

In order to understand how the PBS looks like at a given point in the SBZ, one has to calculate the band structure of the bulk along the line in the bulk Brillouin zone that passes through this point parallel to the surface orientation direction: PBS of the surface at this point of the SBZ will contain all the points of the bulk band structure along this line. This is illustrated in Fig. 5.6 for the $\overline{\Gamma}$ point of the Au(111) surface and $\overline{\Gamma}$ point of the Au(322) surface. For instance, in Fig. 5.7, the PBS of the Au(111) surface is shown along with the bulk band structure along the $\Gamma - L$ line that is projected onto the $\overline{\Gamma}$ point of the SBZ. Indeed, one can see that there are two gaps in Fig. 5.7(b): the first one between -7.3 eV $< E <$ -4.9 eV and the second one between -1.1 eV $< E <$ 3.1 eV that results in the corresponding gap at the $\overline{\Gamma}$ point of the PBS in Fig. 5.7(a).

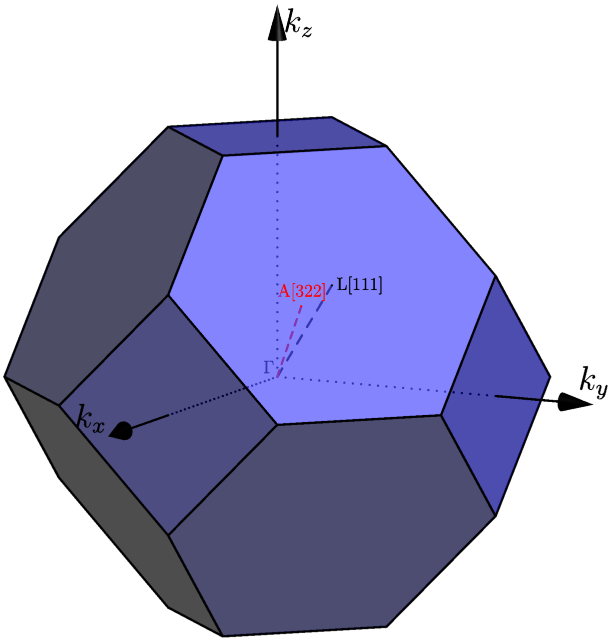

Figure 5.6: Bulk Brillouin zone of Au. Blue dashed line corresponds to the [111] direction ($\Gamma - L$ line) and red dashed line to the [322] direction ($\Gamma - A$ line)

In a similar way one can also study the PBS of any surface including the Au(322), (455) and (788) vicinal surfaces that I have aimed to study in my project. One has to calculate a band structure of bulk Au along the line that passes through the Γ point and the intersection point A of the corresponding direction ([322], [455] or [788]) with the hexagonal face of the bulk Brillouin zone. The line $\Gamma - A$ for the Au(322) surface is shown in Fig. 5.6 with the red dashed line. In Fig. 5.8 I report band structures of bulk Au that correspond to the gap of Au(322), (455) and (788) surfaces. One can see that for the case of the Au(322) surface reported in Fig. 5.8(a) the band gap at $\overline{\Gamma}$ of the SBZ shrinks from the value of 4.2 eV for the Au(111) surface (Fig. 5.7(b)) to the value of 2.6 eV and is no longer present at the Fermi level. At variance, for the cases of Au(455) and Au(788) shown in Fig. 5.8(c) and Fig. 5.8(b), the band gap is smaller (3.5 eV for Au(455) and 3.9

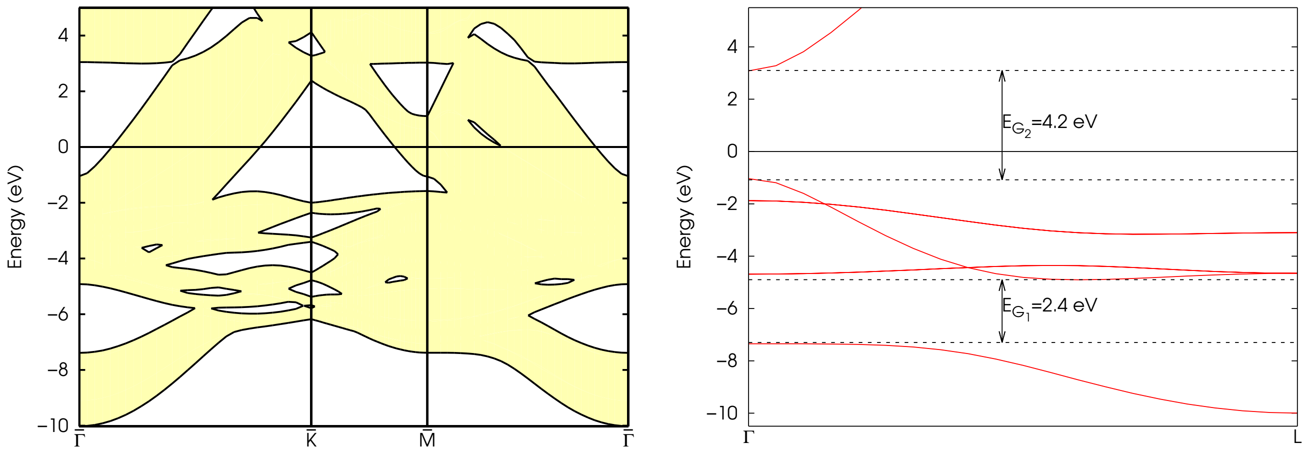

(a) (b)

Figure 5.7: (a) PBS of Au(111) (yellow shaded regions) and (b) bulk band structure of Au plotted along the $\Gamma - L$ line that illustrates how the PBS of Au(111) at $\bar{\Gamma}$ is formed.

eV for Au(788)) than the one for the Au(111) surface shown in Fig. 5.7 but is still present at the Fermi level. From the viewpoint of band structure of such surfaces the shrinking of the band gap at the Fermi level is a significant change. As I have already discussed in the Section 2.2 a "true" (i.e., non-resonant) surface state can be supported only within the gap of the PBS or when outside the gap of the PBS if its bulk band has a symmetry different from the symmetry of the surface state. This means that the Shockley surface state briefly discussed in Section 2.2.2 cannot be supported in Au(322) where, instead, only surface resonances can be observed, while it can exist in Au(455) and Au(788).

5.1.3 Assignment of the surface state

In this Section I have demonstrated how the band structure of vicinal surfaces is refolded and how it leads to the complication of the surface state study procedure outlined in the beginning of the Section. I have shown how, using the calculations for bulk Au, one can nevertheless understand the formation of the PBS and that even from the refolded band structure one can still extract and identify the surface state. In order to obtain the final confirmation that surface states identified in my calculations are indeed derived from the Shockley surface state of the Au(111) surface I also calculate the projections of the surface state wavefunctions onto the atomic orbitals: since the Shockley state of the Au(111) surface projects mainly on p atomic orbitals so should the surface states derived from it.

5.1.4 Surface state modulation

In the Section 2.3.3 I gave the definition of the surface state modulated by the average surface and by the terrace. In order to distinguish the terrace modulated states from the

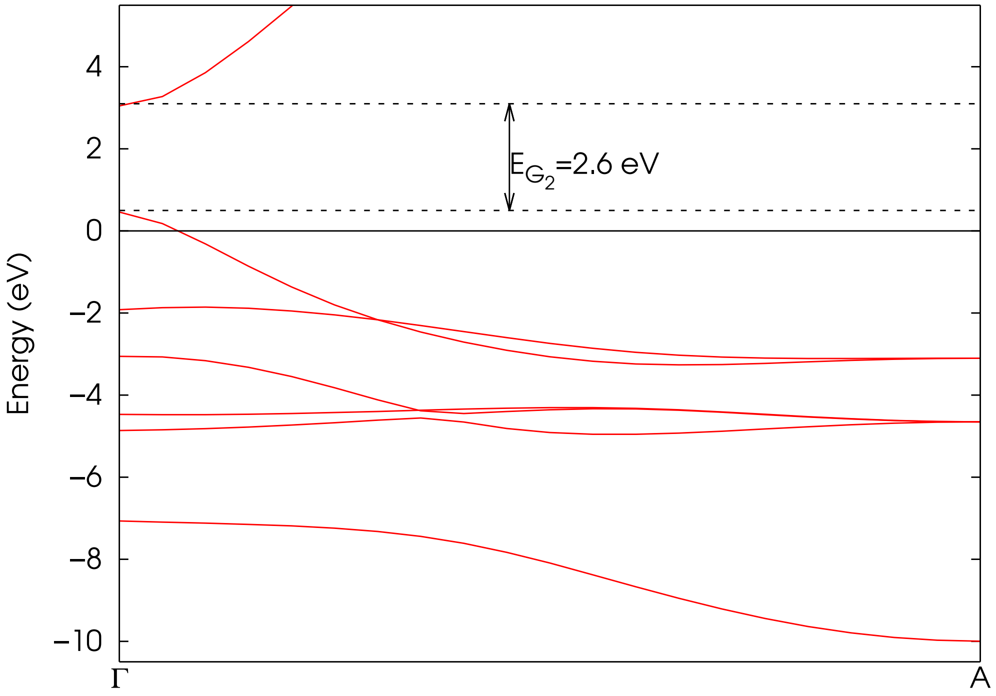

(a)

Figure 5.8: Bulk bands of Au(111) that project onto the $\overline{\Gamma}$ point in the SBZ of (a) Au(322), (b) Au(788) and (c) Au(455) surfaces.

average-surface modulated states or intermediate states I use the modified Eq. (2.1):

$$\psi(z) = A_i e^{kz} cos(G_m z/2 + \delta). \tag{5.1}$$

Here G_m should be equal to $2\pi/a\ cos(\alpha)$ (a is the distance between the consequent (111) layers) for the terrace modulated state and will be smaller than $2\pi/a\ cos(\alpha)$ for the intermediate or average surface modulated state. For the Au(111) surface $a = 4.45\ a.u.$, and since it is a flat surface $G_m/2 = G = 0.706\ a.u.^{-1}$. The values for the $G_m/2$ of the vicinal surfaces *assuming* the terrace modulated state are summarized in the last column of Table 5.1.

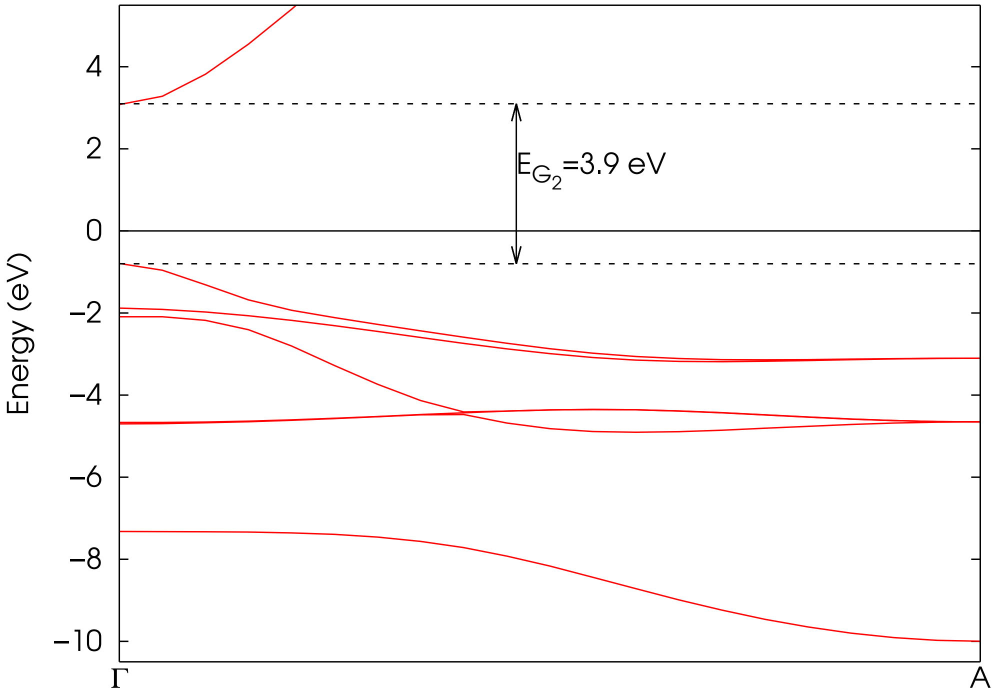

(b)

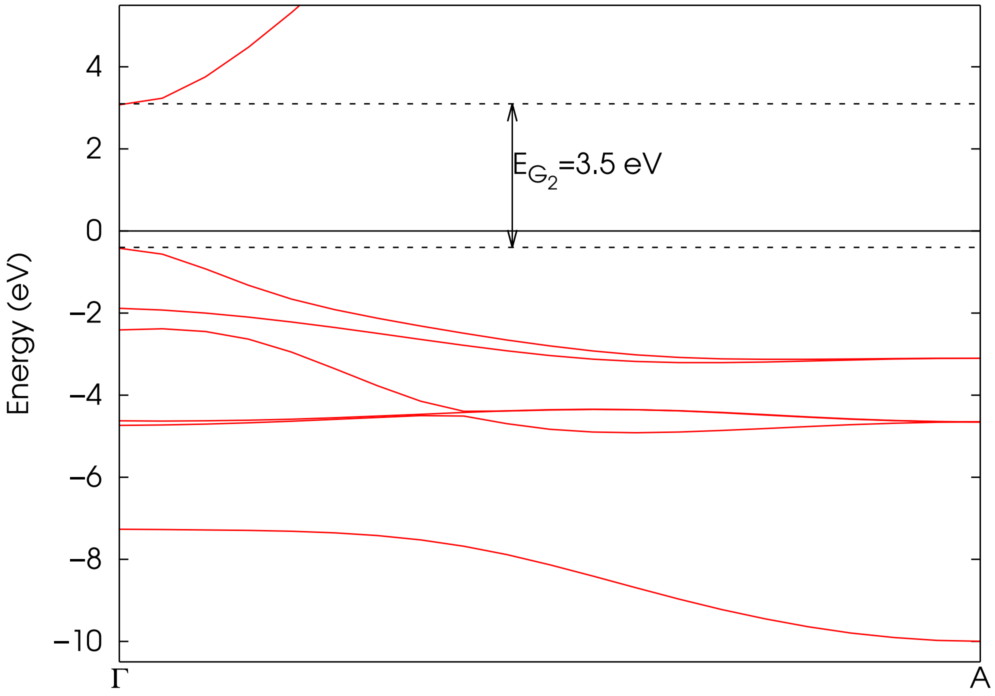

(c)

Figure 5.8: (continued) Bulk bands of Au(111) that project onto the $\overline{\Gamma}$ point in the SBZ of (a) Au(322), (b) Au(788) and (c) Au(455) surfaces.

5.2 The surface states of the vicinal Au(111) surfaces

Let us now concentrate on the *ab initio* study of the surface state on three vicinal Au(111) surfaces: Au(322), Au(455) and Au(788). As I have discussed in the Chapter 2.3, experimentally using ARPES technique, a surface resonance has been observed on Au(322) and a "true" surface state has been observed on Au(788) and Au(23 23 21). In the first case, Au(322) surface, as shown in Fig. 5.8(a), the band gap at the Fermi level is closed (see also Section 5.1.2) due to a relatively big miscut angle and only a surface resonance exists in this case. Also, as terraces are quite narrow (12 Å), electrons that belong to the surface state can propagate from terrace to terrace across the step, forming a 2D resonant surface state. On the other hand, the Au(455) and Au(788) surfaces support a gap at the Fermi level (see Fig. 5.8(b), 5.8(c)) allowing the "true" surface state to exist. In contrast with Au(322), it has been shown experimentally [46, 35] that the electrons of the surface state of Au(788) do not propagate across the step, forming a confined quasi-1D quantum well-like state. The Au(455) surface presents an intermediate case of the surface state in the PBS gap that will be partially confined within the terrace. Table 5.2 summarizes the projections of the surface states for the Au(111), Au(322) Au(455) and Au(788) surfaces onto atomic orbitals that will be discussed later. Table 5.3 summarizes the parameters of the KP model used to fit the surface states.

Surface	miscut angle	Terrace width, Å	Gap at E_F	$G_m/2$, $a.u.^{-1}$
Au(111)	0°	∞	Yes	0.706
Au(322)	11.4°	12	No	0.692
Au(455)	5.76°	23.3	Yes	0.702
Au(788)	3.51°	38.3	Yes	0.7045

Table 5.1: Summary of the key parameters of the vicinal surfaces studied in the present work.

5.2.1 Calculations details

All calculations in this section have been performed at the scalar relativistic LDA level using the ultrasoft pseudoptential with the kinetic energy cut-off for wavefunctions E_{cut} = 30 Ry and 300 Ry for the electronic density. In all cases the experimental bulk lattice parameter was used to generate the slab. Sampling of the Brillouin zone was performed using Monkhorst -Pack **k**-point mesh of 4x12x1, 2x26x1 and 2x16 for Au(322), Au(788) and Au(455) respectively. Surface slab supercells were constructed in a way that the vicinal surface plane is perpendicular to z direction with a vacuum of 30 a.u. along z in order to decouple slabs in the neighboring supercells. Surface states and resonances were identified as those where the sum of the $|\psi|^2$ on the outer layers was more than 0.4-0.6.

Surface	Point	N_a	$N_L(111)$	s	p	d
Au(111)	$\overline{\Gamma}$	2	2	0.15	0.54	0.04
Au(111)(whole)	$\overline{\Gamma}$	21	21	0.18	0.73	0.06
Au(322)	$\overline{Y}$	20	4	0.1	0.37	0.13
Au(322)(whole)	$\overline{Y}$	105	21	0.15	0.54	0.3
Au(455)	$\overline{\Gamma}$	22	2	0.1	0.45	0.08
Au(455)(whole)	$\overline{\Gamma}$	253	23	0.13	0.67	0.17
Au(455)	$\overline{Y}$	44	4	0.12	0.45	0.11
Au(455)(whole)	$\overline{Y}$	253	23	0.15	0.59	0.24
Au(788)	$\overline{\Gamma}$	34	2	0.13	0.48	0.08
Au(788)(whole)	$\overline{\Gamma}$	255	17	0.16	0.65	0.16
Au(788)	$\overline{Y}$	51	3	0.13	0.44	0.09
Au(788)(whole)	$\overline{Y}$	255	17	0.15	0.59	0.23

Table 5.2: Orbital decomposition of the surface states and resonances. N_a is the number of atoms on which the wavefunctions were projected and N_L is the equivalent number of (111) layers. Every second row shows the orbital decomposition of the state over the whole slab.

	Au(322)	Au(322) [35, 42]	Au(788)	Au(788) [35, 42]	Au(455)
$U_0 b$ eVÅ	1.1	1.1	2.1	2.2	1.8
m_x^*,m_e	0.257	0.28(0.27)	0.25	0.255	0.25
ΔE, eV	0.11	0.1	0.04	0.03	0.08

Table 5.3: Summary of the parameters of the Kronig-Penney (KP) model used to fit the surface state and surface resonance parameters obtained through *ab initio* calculations and KP model parameters used to fit the experimental data (when available) from Ref. [35, 42]

5.2.2 The surface state of Au(322)

I start with the Au(322) surface with the miscut angle $\alpha = 11.4°$. In Fig. 5.9 I show the part of the band structure of Au(322) where blue dots mark the states that are partially localized on the surface, green and golden dots mark the experimental results from Ref. [35] shifted upwards. For convenience refolded bands or bands that belong to the PBS are not shown. Partially localized states were identified as states for which $|\psi|^2 > 0.6$ for the 20 surface-atoms ($\sim$ 4 layers of Au(111)).

In this band structure one can observe several localized states around -0.2 eV close to the $\overline{Y}$ point of the SBZ that have parabolic like dispersion in the $\overline{Y} - \overline{\Gamma}$ direction. I point out that as a surface resonance is mixed with bulk states in the band structure calculation it can be represented by an energy window and not by a single state, unlike "true" surface states. In Fig. 5.9 one can indeed see that there are multiple partially localized states that span from -0.3 eV to -0.1 eV close to the minimum at the $\overline{Y}$ point. Tentative edges of the energy window for this surface resonance are marked with blue dashed lines. To enable easier comparison between the calculated surface band dispersion for Au(322) with the experimental surface band dispersion for Au(322) obtained using ARPES [35] the latter is

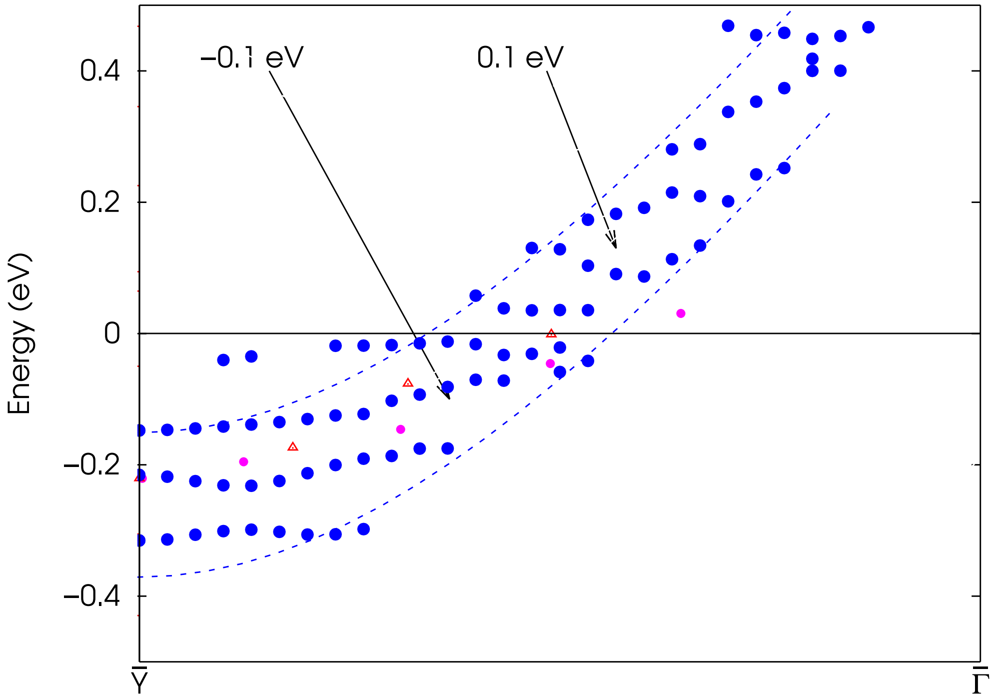

Figure 5.9: The dispersion of the Au(322) surface state. Blue dots mark the states identified as partially localized, purple and red symbols mark the experimental results [35] shifted up by 0.14 eV. Arrows mark the surface states for which planar averages are shown in Fig. 5.10. The Au(322) surface was modeled with a 105 atom slab (∼ 50 Å thickness).

shifted up in energy by 0.14 eV to match band minimum. From this result we can see that the shape, and thus the effective mass, of the calculated dispersion of the Au(322) surface resonance is in good agreement with the dispersion measured experimentally, however it is shifted upwards in energy with respect to experimental dispersion. There are a few possible reasons for such a discrepancy: first, the calculation for Au(322) might not be fully converged and, second, the shift can be due to the spin-orbit coupling that was neglected in this calculation while it is know to shift the Shockley state of Au(111) down by approximately 0.1 eV [34].

Now let us concentrate on the character of this surface resonance, specifically on the planar averages of the charge density and charge density distribution with respect to the step. In Fig. 5.10 I show the planar averages for three states at $\overline{Y}$ from -0.3 eV to -0.1 eV and at two other points close to the Fermi level (marked with arrows in Fig. 5.9). These states show a behavior typical of a surface resonance: they are partially localized within 10 a.u. around the surface and they extend infinitely into the bulk. I also point out that this surface resonance projects mainly onto the p atomic orbitals of the topmost surface layers, similarly to the Shockley surface state of Au(111) as one can see from the Table 5.2: 60% of the surface state wavefunction at $\overline{Y}$ projects onto the four topmost layers, while for the Shockley state of the Au(111) surface, 70% of its wavefunction projects onto the two topmost layers. I also note the higher overall contribution from the d states.

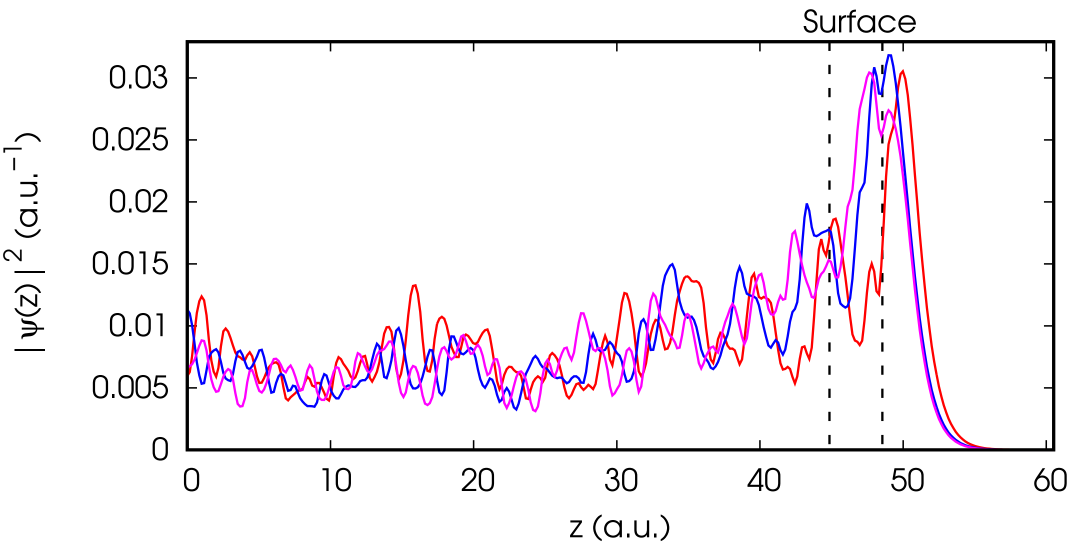

(a)

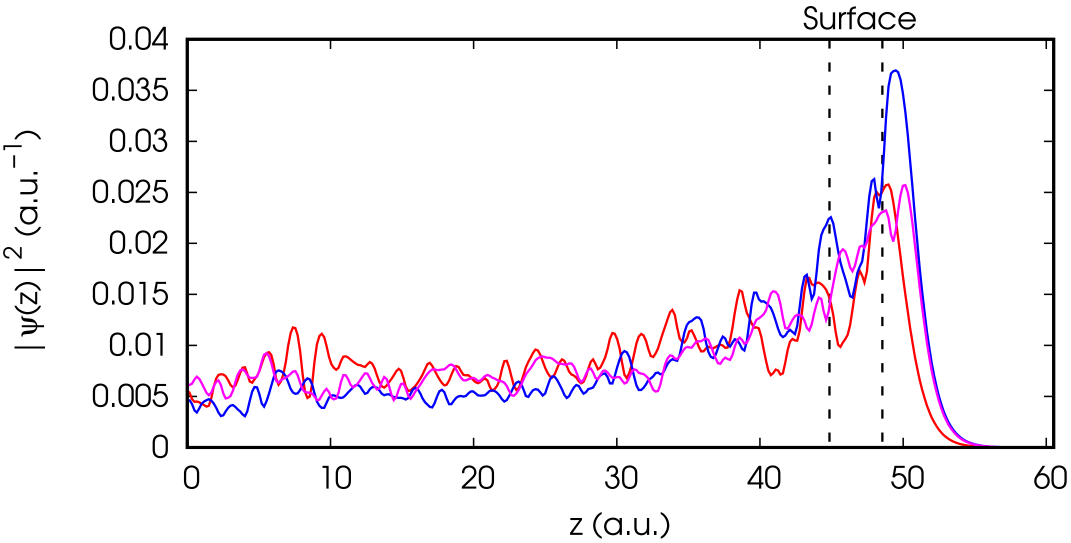

(b)

Figure 5.10: Planar averages of the surface resonance states of Au(322) at (a) the $\overline{Y}$ point, (b) and (c) points where the surface resonance is around -0.1 eV (below) and around 0.1 eV (above the Fermi level) marked with arrow in Fig. 5.9. Vertical dashed lines indicate the position of the surface. Different colors correspond to wavefunctions with different eigenvalues identified as surface resonances at the same **k**-point.

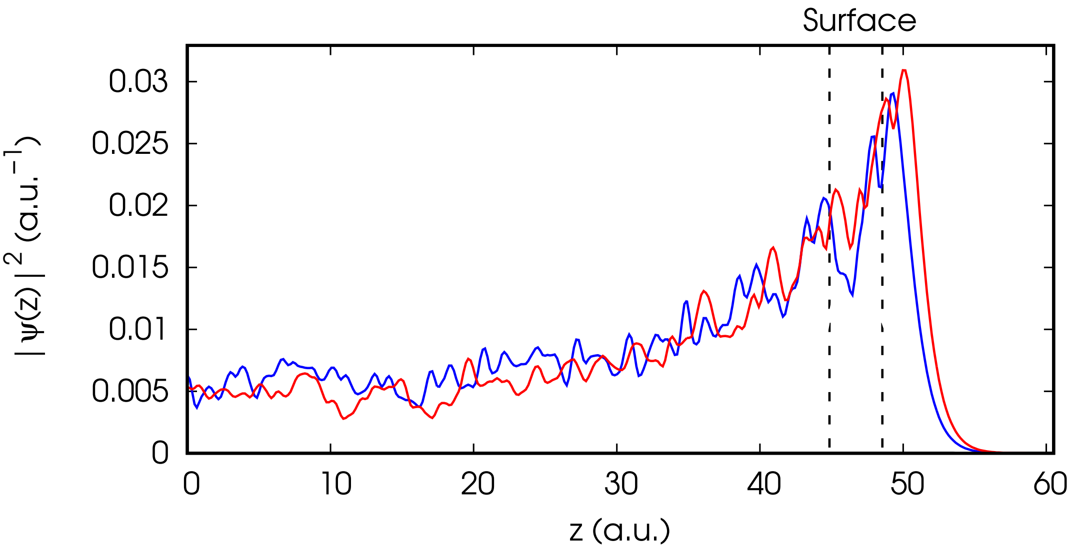

(c)

Figure 5.10: (continued) Planar averages of the surface resonance states of Au(322) at (a) the $\overline{Y}$ point, (b) and (c) points where the surface resonance is around -0.1 eV (below) and around 0.1 eV (above the Fermi level) marked with arrow in Fig. 5.9. Vertical dashed lines indicate the position of the surface. Different colors correspond to wavefunctions with different eigenvalues identified as surface resonances at the same **k**-point.

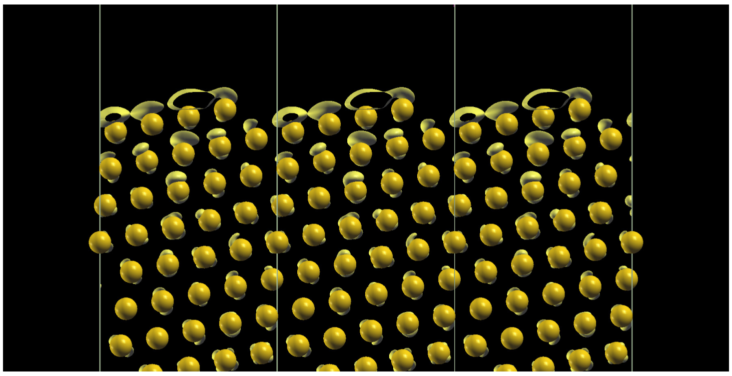

Figure 5.11: Sideview of the Au(322) isosurface of the charge density distribution for the surface resonance at the bottom of the band at $\overline{Y}$ point (Fig 5.10(a)).

Planar averages allow us to distinguish between bulk states, "true" surface states and surface resonances, however they do not give any information regarding the propagation character of the surface electrons. In order to determine whether the electrons of the surface state propagate across the step or is confined within the terrace one has to look at the distribution of the charge density at the surface. In Fig. 5.11 I show the isosurface of the combined charge density for the surface resonance shown in Fig. 5.10 at the $\overline{Y}$ point. One can see here that indeed this surface resonance is not confined within the surface and has a 2D average-surface character as the charge density (and thus the wavefunction) decays in the direction perpendicular to the (322) plane. This state is not a terrace modulate state. It is also confirmed with the equation (5.1) applied to the surface state planar average: the parameter $G_m = 0.6315\ a.u.^{-1}$ while it would be $G_m = 0.691\ a.u.^{-1}$ for the terrace modulated state (Table 5.1).

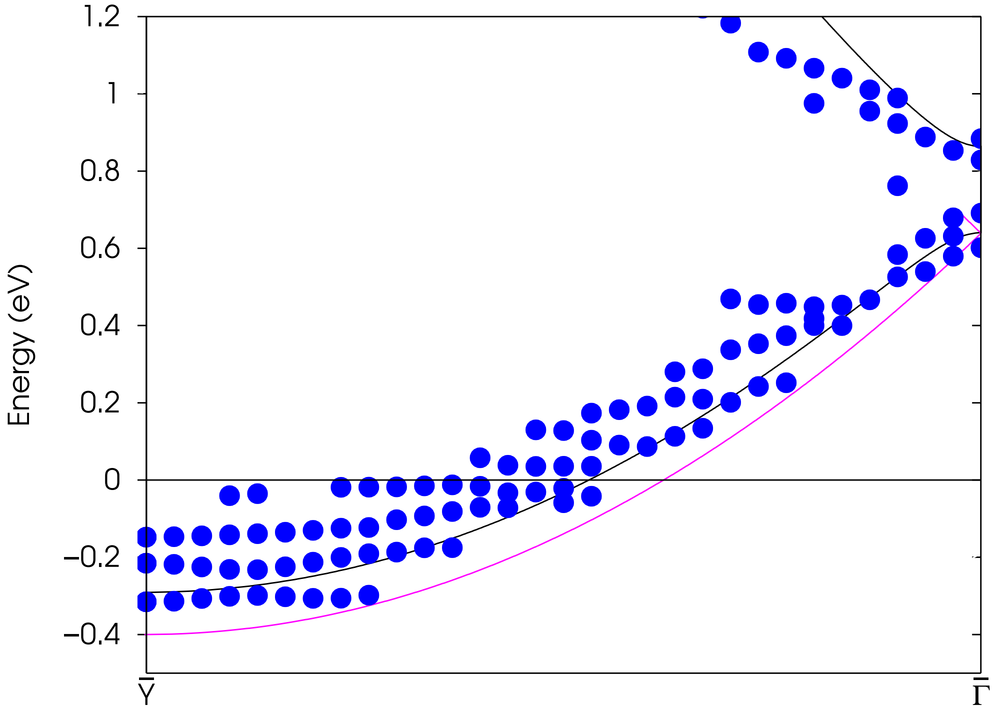

Figure 5.12: The dispersion of the surface state of the Au(322) surface is shown as blue dots. The solid black line shows the results of the band dispersion obtained with the 1D KP model.

Following Refs. [35, 42] using the 1D Kronig-Penney (KP) model it is possible to fit the KP bands on the *ab initio* calculation and to estimate the step barrier strength from the shift of the surface resonance band minimum with respect to the minimum of the surface state on the flat Au(111). Using the equation (2.4) with $E_0 = -0.4$ eV as a reference surface state energy for flat Au(111). I have calculated the dispersion of the bands in the 1D periodic potential shown in Fig. 5.12 with black line using the barrier strength $U_0 b = 1.1$ eV and the effective mass $m^* = 0.257 m_e$ obtained from the parabolic fit of the bands in the y direction (along the $\overline{Y} - \overline{S}$ path). *Ab initio* surface bands are shown as blue dots, and the magenta curve shows the free electron dispersion. One can see that the bands obtained using the KP model are in good agreement with my *ab inito* calculations. These results are consistent with results obtained in Ref. [42] as it can be seen from the Table 5.3. I point out that in Ref. [35] the effective mass m^*_x obtained with a parabolic fit of the surface band dispersion is slightly higher than the effective mass m^*_y in the y direction or in Au(111) - this can be readily explained with the KP model, as the m^* at the band bottom will always be higher than that of the free-electron. Also, unlike the ARPES experiments [35, 42], in *ab initio* calculations it is easier to access to the unoccupied states, allowing the better assessment of the KP model calculation accuracy. In this case, in Fig. 5.12 one can see that the small gap is opened at 0.6 eV above the Fermi level between the top of the first subband and the bottom of the second one. The size of the gap obtained from the 1D KP model agrees with the gap observed in my *ab initio* surface state band structure.

5.2.3 The surface state of Au(788)

Let us now concentrate on the Au(788) vicinal surface with the miscut angle $\alpha = 3.5°$ where it has been observed [35, 42, 48] that the surface state displays weakly dispersing bands typical of a 1D quantum well. In Fig. 5.13 I show the part of the *ab initio* band structure that contains the surface band dispersion along the $\overline{Y} - \overline{\Gamma}$ path marked as blue dots and experimental data extracted from Ref. [48] marked with red point and line. The experimental data is shifted upwards by 0.1 eV to enable an easier comparison between the experimental and *ab initio* results. Like in Ref. [48] I observed several dispersive subbands that are characteristic of the quantum well. Again as in the case for Au(322), the agreement between calculations and experiments is quite good provided that experimental bands are shifted upwards by 0.1 eV. Such a shift can arise from the spin-orbit coupling that was neglected in this calculation and is known to shift the Shockley surface state by approximately 0.1 eV.

Let me start with the surface state localization at various SBZ points and its character. First, I show the planar average in Fig. 5.14 for the first subband bottom at $\overline{Y}$ and maximum at $\overline{\Gamma}$ and for the second subband maximum at $\overline{Y}$. At the first subband bottom at $\overline{Y}$ in Fig. 5.14 one can see that the surface state, while being well localized at the surface, has nonetheless a bulk tail typical of a surface resonance, as, close to the edge of the SBZ surface the state can mix with bulk states. However, at the center of the SBZ, where there is a well defined gap in the PBS, the surface state charge density planar average behaves much alike the charge density planar average of the surface state of the Au(111) surface that was shown in Fig. 2.5(a). Like in the previous cases of Au(111) and Au(322) this surface state projects mainly onto the p atomic orbitals of the surface atoms as one can see in Table 5.2. I note that for the Shockley states at $\overline{\Gamma}$, 69% of the surface state projects onto the two topmost surface layers, much like the Shockley state of the Au(111) surface. At variance, the surface resonance at $\overline{Y}$ is only partially localized, with 65% projecting onto the three topmost surface layers. Next, I show the isosurfaces of the charge density of the surface state at these points. Unlike the case of the Au(322) surface presented in the Section 5.2.2, the charge density distribution of the Au(788) surface state

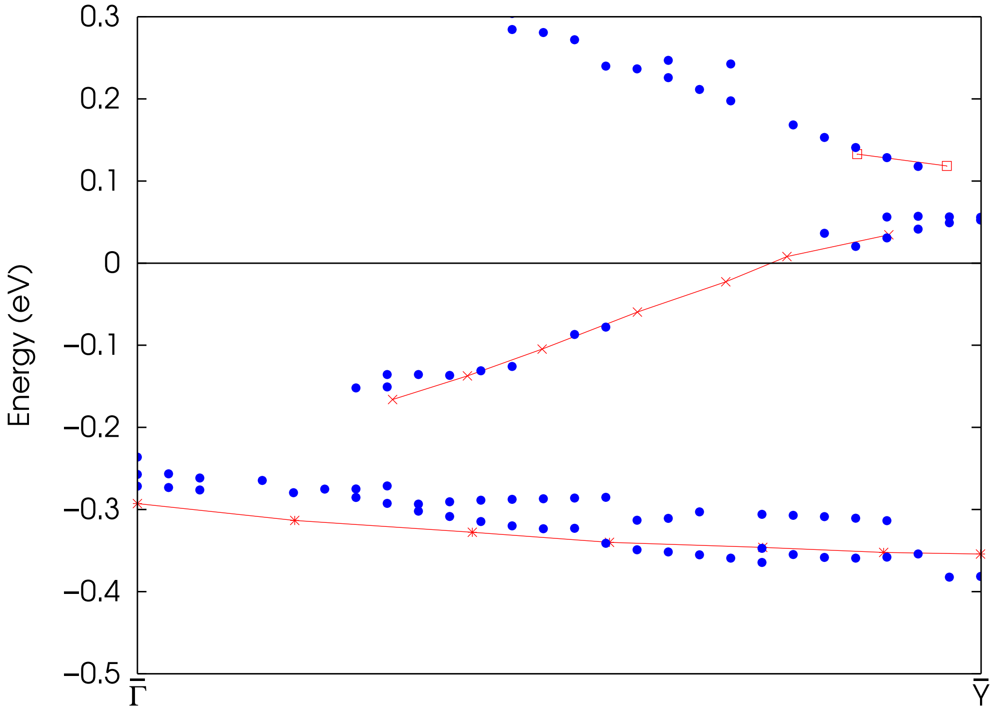

Figure 5.13: The dispersion of the surface state of the Au(788) surface is indicated with blue dots and the experimental surface state dispersion [48] shifted up by 0.1 eV is indicated with red crosses and lines.

indicates that the wavefunction of this surface state decays in the direction perpendicular to the terrace plane, meaning that this surface state is a 2D terrace modulated state. It is indeed confirmed with the equation (5.1) applied to the surface state planar average at $\overline{\Gamma}$ as $G_m = 0.704\ a.u.^{-1}$, which is the value close to the one reported in Table 5.1 for the ideal terrace modulated state.

In the same way it was done for the Au(322) surface, it is possible to apply the 1D KP model in order to analyze the surface band dispersion and estimate the barrier strength. Using the barrier strength $U_0 b = 2.1$ eV and the effective mass $m^* = 0.25 m_e$ I have obtained the band dispersion shown in Fig. 5.16. One can see in this figure that there is a qualitative agreement between *ab initio* and model calculations: in both cases the bands are split into weakly dispersive subbands of the particle in 1D periodic potential, however the maximums of the first and second subbands in *ab initio* calculations are slightly shifted up by 0.04 eV that might indicate that the m^* obtained by the parabolic fit of the bands in the y direction is higher than the real value of the effective mass for this band. Alternatively it might indicate that the simple 1D KP model cannot be applied in this case without some modifications.

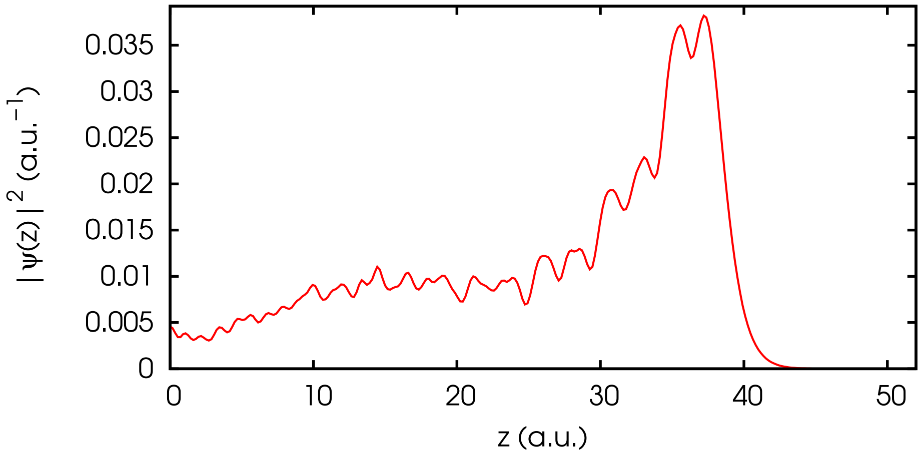

(a)

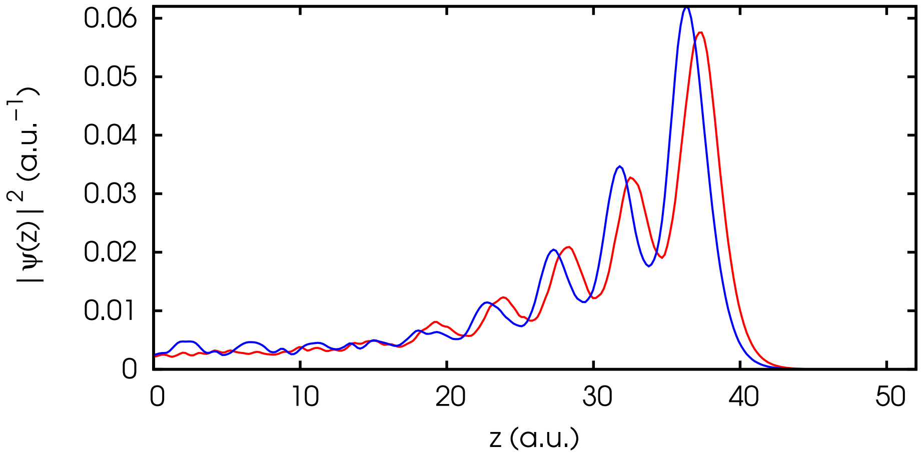

(b)

Figure 5.14: Planar averages of the surface states of Au(788) at (a) the bottom of the first subband at the $\overline{Y}$ point, (b) the top of the first subband at the $\overline{\Gamma}$ point and (c) the top of the second subband at the $\overline{Y}$ point. Different colors correspond to wavefunctions with different eigenvalues identified as surface resonances at the same **k**-point.

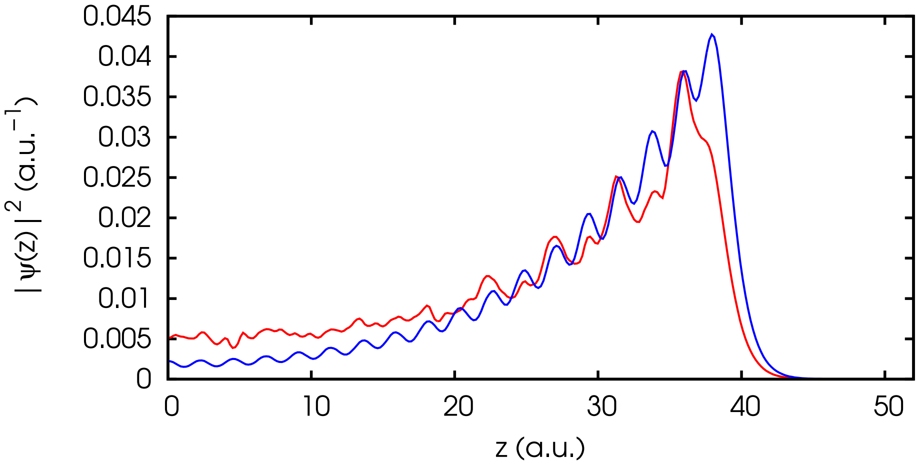

(c)

Figure 5.14: (continued) Planar averages of the surface states of Au(788) at (a) the bottom of the first subband at the $\overline{Y}$ point, (b) the top of the first subband at the $\overline{\Gamma}$ point and (c) the top of the second subband at the $\overline{Y}$ point. Different colors correspond to wavefunctions with different eigenvalues identified as surface resonances at the same **k**-point.

5.2.4 The surface state of Au(455)

In this section I discuss the intermediate case between narrow and wide terraces of Au(322) and Au(788), namely the Au(455) surface with the miscut angle $\alpha = 5.77°$ - small enough to have the band gap opening at the $\overline{\Gamma}$ point - and with an average terrace width of $L = 23.5$ Å. Such a value of the terrace width is small enough to ensure that the surface state will have mainly a 2D character. Unfortunately experimental data for the Au(455) surface is not available as this surface can undergo reconstruction and faceting [44]. As before, I start with the surface band dispersion along the $\overline{Y} - \overline{\Gamma}$ path shown in Fig. 5.17. Along with the calculated bands, I also depict in this figure the results obtained using the 1D KP model that will be discussed later in this section. In this figure one can see that indeed, the Au(455) surface presents an intermediate case between the Au(322) and Au(788) in terms of the surface band dispersion: while it clearly shows that the surface state is split into subbands, its dispersion is not as weak as the dispersion of the first subband of Au(788).

Now let us take a closer look on the localization of the surface state shown in Fig. 5.18. Similarly to the results shown in Fig. 5.14, at the bottom of the first subband at the $\overline{Y}$ point, the surface state has a bulk tail in the wavefunction due to the mixing with the bulk states at the edges of the SBZ, while at the top of the first subband at the $\overline{\Gamma}$ point, where there is a gap in the PBS, the surface state becomes a true gap surface state like the Shockley state of the Au(111) surface. However, the behavior of the surface state wavefunction in-plane, and the way it decays into the bulk, are qualitatively different from the behavior of the surface state of Au(788) shown in Fig. 5.15. At the $\overline{Y}$ point the Au(455) surface state appears to behave like a 2D average-surface modulated state:

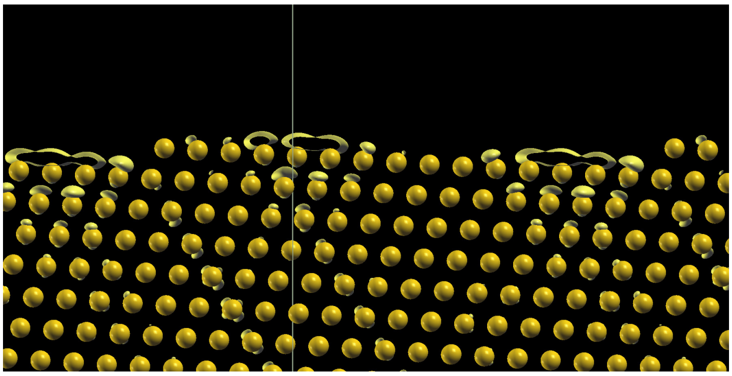

(a)

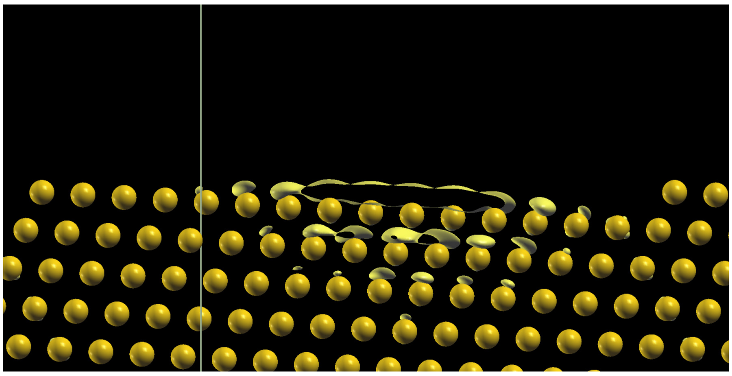

(b)

Figure 5.15: Charge density distribution isosurface of the surface states of Au(788) at (a) the bottom of the first subband at the $\overline{Y}$ point and (b) the top of the first subband at the $\overline{\Gamma}$ point.

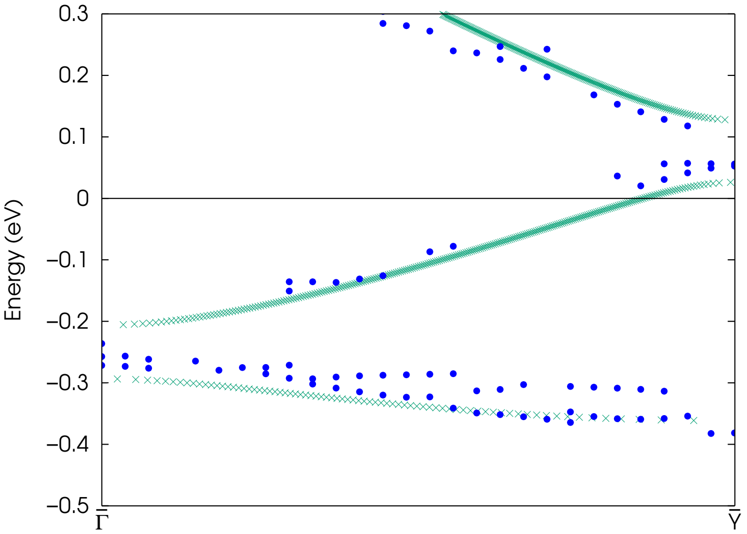

Figure 5.16: The surface state dispersion (blue dots) of the Au(788) surface together with results obtained with the 1D KP model (green crosses).

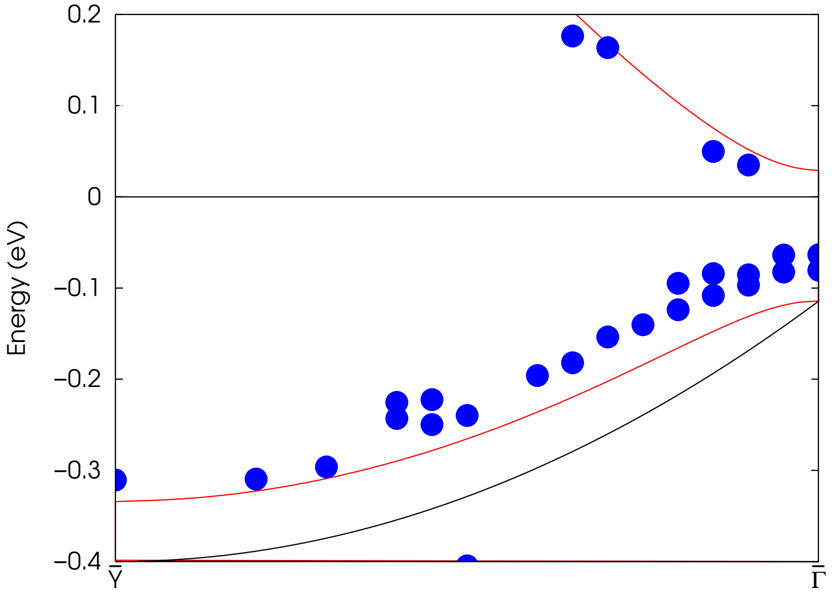

Figure 5.17: The surface state dispersion (blue dots) of the Au(455) surface together with results obtained with the 1D KP model for the Au(455) (red line) and the Au(111) (black line) surfaces.

it is not confined within the terrace and it decays approximately in the [455] direction. Although at $\overline{\Gamma}$ the state appears to be confined within the terrace it still 'sees' the average-surface as it decays in the direction between [455] and [111], and not in the [111] direction like the surface state at $\overline{\Gamma}$ of Au(788) shown in Fig. 5.15(b). This is confirmed as well with the Eq. (5.1), where $G_m = 0.675\ a.u.^{-1}$ while it would be $0.701\ a.u.^{-1}$ for a terrace modulated state (see Table 5.1). I also note that these two values lie closer to each other compared to those of the Au(322) surface, indicating that the character of the Au(455) surface is somewhere in between the terrace modulated and the average surface modulated state.

Finally, let me briefly discuss the fit of the calculated bands with the KP model. The solid red line in Fig. 5.17 shows the results of the KP model calculation for the band dispersion in Au(455) using the barrier strength of $U_0 b = 1.8$ eV and effective mass $m^* = 0.25\ m_e$ obtained with a parabolic fit of band dispersion in the y direction. The solid black line shows the corresponding free electron dispersion. As in the case of Au(788) I note that while the minima of subbands are quite well reproduced with the simple model, the maximum of the band at $\overline{\Gamma}$ in the *ab initio* calculation is shifted up, indicating that the effective mass is smaller than the one of the flat Au(111) surface.

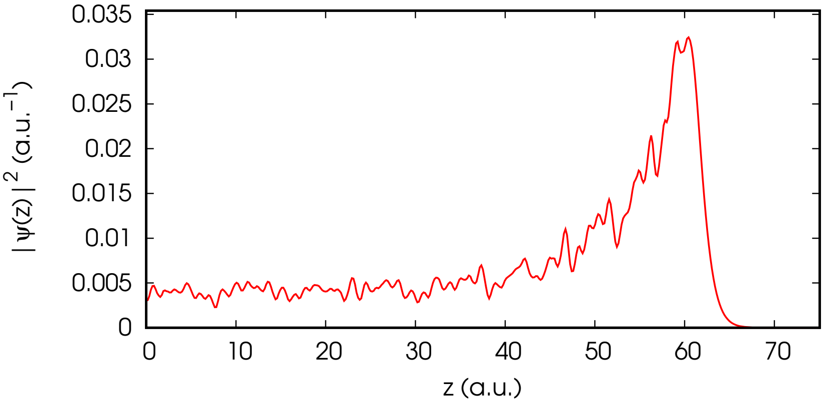

(a)

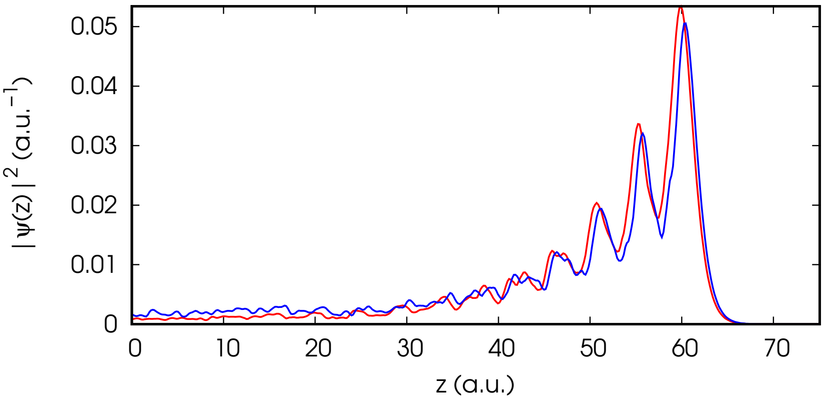

(b)

Figure 5.18: Planar averages of the surface states of Au(455) at (a) the bottom of the first subband at the $\overline{Y}$ point and at the (b) top of the first subband at the $\overline{\Gamma}$ point. Different colors correspond to wavefunctions with different eigenvalues identified as surface resonances at the same **k**-point.

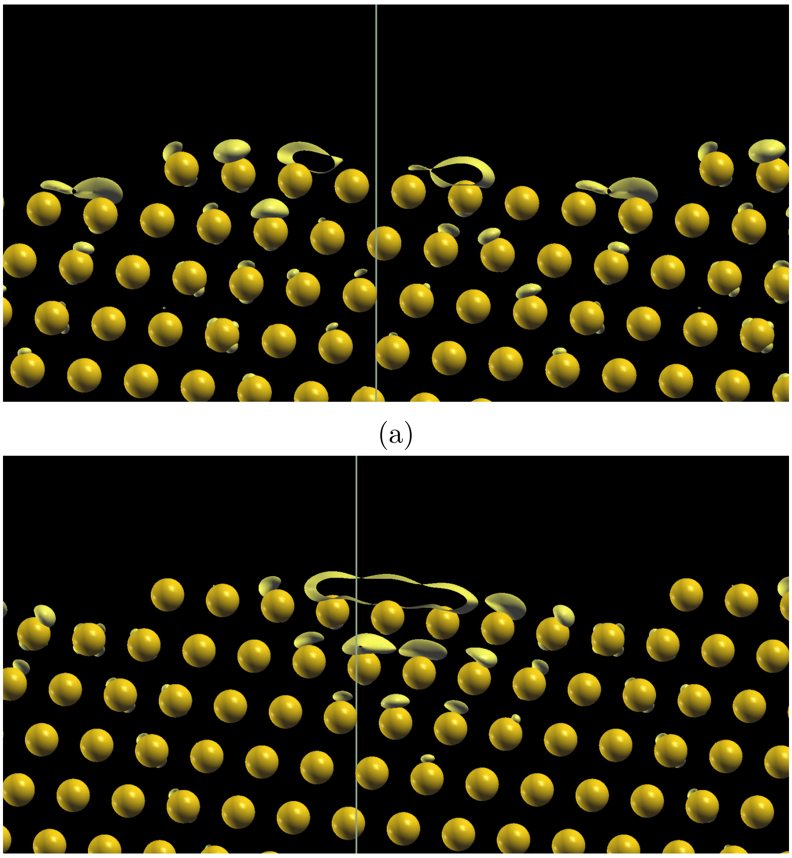

(a)

(b)

Figure 5.19: The charge density distribution isosurface of the surface states of Au(455) at (a) the bottom of the first subband at the $\overline{Y}$ point and (b) the top of the first subband at the $\overline{\Gamma}$ point.

5.3 Summary and outlook

This chapter is devoted to the calculation and analysis of the surface band structure and surface states obtained by means of *ab initio* DFT calculations.

First, I have discussed in details the formation of the surface band structure for the vicinal surfaces. I have shown how the gap in the PBS evolves depending on the miscut angle with the Au(111) surface through the computation of bulk band structure along the special path in the Brillouin zone, confirming that the gap at the Fermi level shrinks with increasing the miscut angle. Then I have discussed and explained the refolding of the band structure in supercell calculations, specifically in the case of the orthorhombic supercell of flat and vicinal Au(111). I have demonstrated how one can understand the complex refolded band structure using simple geometrical reasoning. Then I have performed an unfolding of the band structure for the small orthorhombic supercell of Au(111).

Second, I have performed an *ab initio* calculations for three vicinal surfaces, Au(322), Au(788) and Au(455) at the scalar-relativistic LDA level. I have shown, using projections onto the atomic orbitals, that Shockley states in the gap of the bulk PBS of the Au(455) and Au(788) surfaces are almost as localized as the Shockley state of the Au(111) surface. At variance, the resonant surface states are less localized on the surface and have a tail that extends infinitely in the bulk of the slab. Nevertheless all these surface states and resonances mainly project on the p atomic orbitals, like the surface state of the Au(111) surface. I also note that resonant surface states project more on the d atomic orbitals compared to the Shockley state, indicating the strong mixing with bulk d bands. I have demonstrated that surface state dispersion and character obtained with *ab initio* calculations are in good qualitative agreement with earlier experimental results, i.e. I have observed a 2D surface resonance for Au(322) that shows an average-surface modulated character and a partially confined quasi-1D surface state for the Au(788) surface that forms weakly dispersive subbands that have a terrace modulated character.

Last, I have used the 1D Kronig-Penney model in order to perform a quantitative comparison between surface bands of three surfaces and experiments. For Au(322) the agreement between the *ab initio* results, model calculation and experiments is remarkable, showing the same barrier strength, band bottom shift and effective mass for experimental and theoretical band dispersions. Moreover, the surface band dispersion calculated with the 1D Kronig-Penney model is in perfect agreement with the *ab initio* surface band dispersion, proving that the model is suitable for this system. At variance, fitting of the calculated surface band dispersion with the Kronig-Penney model underestimates the maxima of the subbands for both Au(455) and Au(788) surfaces, while giving an overall good qualitative picture. I assume two possible reasons for this discrepancy: either the calculations performed to obtained these results are not fully converged, or more likely, the simple 1D model is not completely suitable for these systems.

In perspective, the surface bands of Au(788) and Au(455) should be investigated thoroughly with SOC in order to resolve the discrepancies between model, calculations and experiments, in particular to understand the magnitude of the SOC-induced energy shift. In addition one could study Au(23 23 21), as this surface has wide terraces allowing the total confinement shown in the ARPES experiments. Finally, in this chapter I have shown that using *ab initio* DFT calculations it is possible to conduct a thorough study of the surface state of vicinal surfaces. I have also shown that using a simple 1D KP model it is possible to fit the resulting dispersion. It means that in principal, by performing calculations for a variety of similar surfaces it would be possible to create a comprehensive database of the KP model parameters that would allow to interpolate them onto other surfaces and accurately predict the surface state dispersion for other similar surfaces without performing calculations. At variance, for more complex systems, i.e. nanowires on vicinal surfaces or adsorbed nanoparticles I would not expect the KP model to work as good. Rather, for these kind of surfaces the methodology I used in this chapter to study the surface states of vicinal surfaces can be employed.

Chapter 6

Ab initio calculation of EEL spectra for bulk Au. Influence of spin-orbit coupling

In this chapter I present the results of *ab initio* calculations of EEL spectra for bulk Au and the Au(111) surface with and without SOC. To date multiple *ab initio* studies of valence EEL spectra have been performed for bulk Au [57, 52] or for the Au(111) surface [58] in order to characterize surface plasmon, revealing and discussing the origin of various peaks in EEL spectra [52] and obtaining the dispersion of the acoustic surface plasmon [58] showing the good agreement with the experimental results. It was suggested by the author of the Ref. [58] that the remaining discrepancy between the *ab initio* ASP dispersion and experimental results for Au(111) might be due to the neglect of SOC in the calculations. Before studying the EEL spectra of the Au(111) surface I will first discuss in details bulk Au. In this chapter I will discuss the bulk Au EEL spectrum for vanishing $\mathbf{q}$ and revisit the discussion of the peaks in the low-energy region of the spectrum. Then I will discuss the effect of including SOC on EEL spectra of bulk Au for both vanishing and finite values of $\mathbf{q}$ and I will show that inclusion of SOC for a vanishing transferred momentum improves the agreement with the experimental results.

6.1 EEL spectra of bulk Au

In this section the influence of SOC on the EEL spectrum and plasmon of bulk Au is discussed. Inclusion of SOC in the DFT calculations leads to splittings and slight shifts of the d-bands in the Au Kohn-Sham bandstructure [69], thus interband transition peaks in the EEL spectra that dominate valence EEL spectra (see Sec.3.2.1) are expected to shift and split accordingly. In addition, it might have an influence on the position and intensity of the bulk plasmon peak in the EEL spectrum as the $5d \rightarrow 6s$ interband transition is also shifted in energy.

6.1.1 Computational details

Calculations have been performed by using scalar-relativistic (SR) or fully-relativistic (FR) ultrasoft pseudopotentials with 11 electrons in the valence region and the LDA approximation for the exchange-correlation functional except for the EEL spectrum calculations for vanishing $\mathbf{q}$. In that case I have used the optimized norm-conserving PBE pseudopotential containing 19 electrons in the valence region and aimed to reproduce experimental results in a wider frequency region than the pseudopotential with 11 electrons in the valence region (see details on pseudopotential and exchange-correlation approximation selection in Appendix).

I have used the experimental lattice constant at room temperature $a_0 = 7.71$ a.u. and the kinetic-energy cutoff $E_{cut} = 20$ Ry for 11 electron pseudopotential and $E_{cut} = 20$ Ry for 19 electron pseudopotential, which was sufficient to obtained converged EEL spectra up to E=30 eV. The sampling of the first Brillouin zone (BZ) was performed using a uniform 32x32x32 $\mathbf{k}$ point mesh centered at the Γ point. Methfessel-Paxton smearing with a broadening parameter of 0.002 Ry was used for the ground-state calculation.

EEL spectrum calculations were performed using the Liouville-Lanczos approach implemented in the thermo_pw module for QUANTUM Espresso package. In order to obtain the converged EEL spectrum 4000 Lanzos iteration with extrapolation to 20000 iterations were performed for each value of the transferred momentum. A Lorentzian broadening of 0.01 Ry is used to plot the EEL spectra.

6.1.2 EEL spectra of bulk Au

6.1.2.a EEL spectrum of bulk Au without SOC

First, I would like to briefly revisit the EEL spectrum of bulk Au in the scalar-relativistic approximation. In the Fig. 6.1 I show the loss function of bulk Au and the corresponding dielectric function computed using an optimized norm-conserving pseudopotential with 19 electrons in the valence region (see Appendix A.1). Table. 6.1 summarizes the most prominent peaks and their origins in the loss function (peak labeling for peaks 1-6 has been adapted from Ref. [52]) (see also Fig. 3.1(b)).

While the bulk plasmon peak and peaks 2-6 have been thoroughly discussed [55, 52], I would like to pay a closer attention to peaks labeled 1 and $2'$ in Fig. 6.1(a).

Peak 1 in the SM of Ref. [52] has been attributed to the plasmon-type resonance, as ϵ_1 vanishes and a local minimum is observed in ϵ_2 (see Fig.6.1(b)). To further elaborate on this assumption I note that one can extend a model used to explain a red-shift of the bulk plasmon in Sec. 3.1.2 adding another bound oscillator with frequency ω_1 in the Eq. (3.4):

$$\epsilon(\omega) = 1 - \frac{\omega_{BP}^2}{\omega^2} + \frac{f_1\omega_{BP}^2}{\omega_1^2 - \omega^2} + \frac{f_2\omega_{BP}^2}{\omega_2^2 - \omega^2}, \tag{6.1}$$

where $\omega_1 = 2.6$ eV is the frequency of the interband transition onset around X and $\omega_2 = 7$ eV is the frequency of the second interband transition produced by $d \to s$ and $d \to p$ transitions along the $W - K$ path in the Brillouin zone [79]. If one assumes $f_1 = f_2 = 1$ (similarly to supplemental material of Ref. [52]) $\epsilon(\omega)$ of Eq. (6.1) will vanish

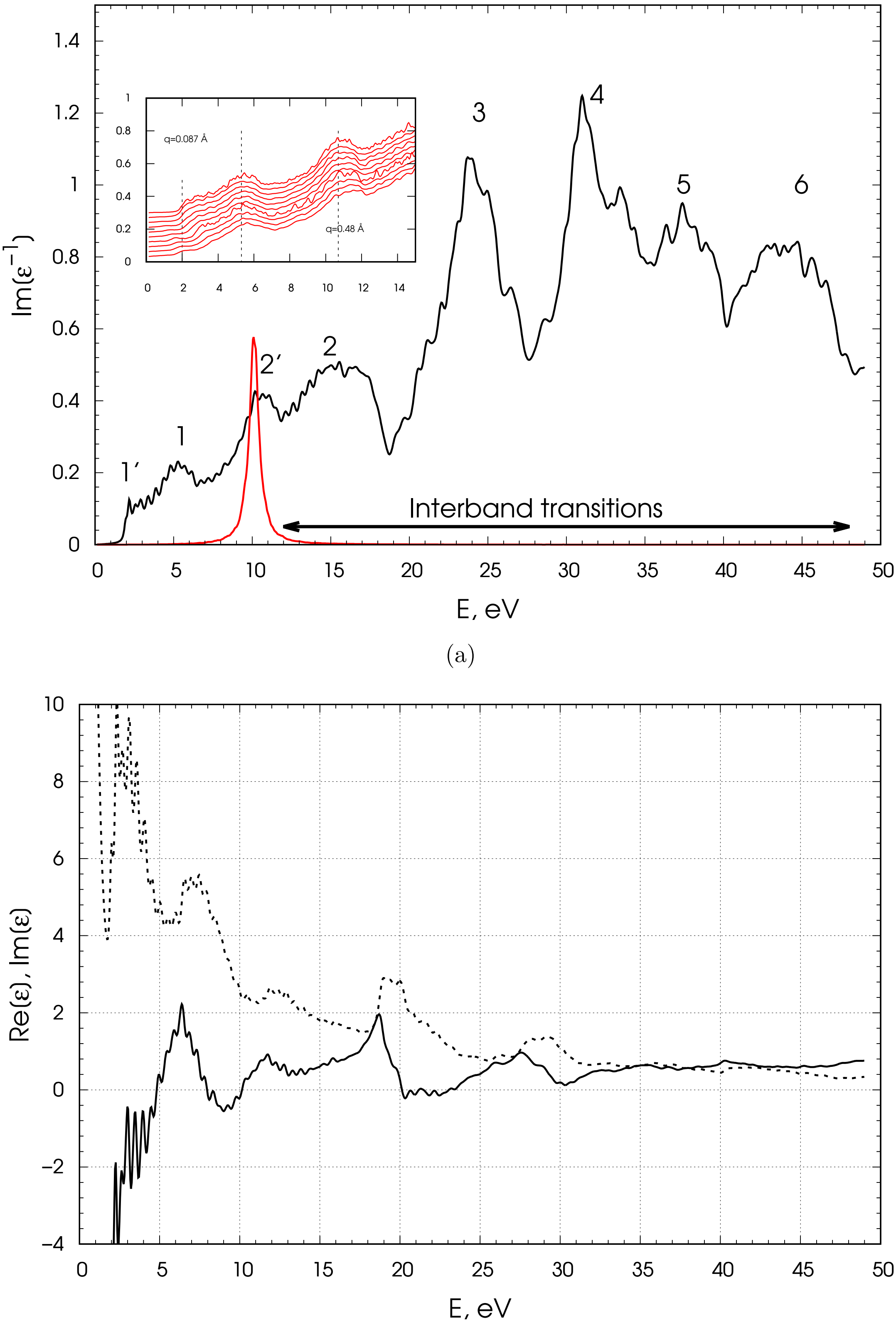

(a)

(b)

Figure 6.1: (a) EEL spectra for bulk Au with 19 electrons (black line) and with 1 electron (red line) in the valence calculated without SOC at the experimental lattice parameter for vanishing **q**. The inset shows the loss spectra for different values of **q** (spectra are offset for clarity) of plasmon-type excitations 1′, 1, 2′ in the 0-15 eV region. (b) Real (solid line) and imaginary (dashed line) part of the dielectric function of bulk Au with 19 electron pseudopotential.

peak #	ω,eV	origin	comments
$1'$ (BP)	2.2	Bulk plasmon screened by 5d	Severely damped due to the underestimation of the interband transition onset
1 (5d BP)	5.3	Plasmon-type resonance from 5d	
$2'$(UP)	10.5	Screened BP from 6s	
2	15.4	Classical Drude-Lindhard oscillators [51, 52]	
3	24		
4	31		
5	37		
6	44		

Table 6.1: Summary of the position ang origins of peaks labeled in EEL spectra for vanishing **q** shown in Fig. 6.1(a). Labels $1'$ and $2'$ are supplemental to the labels given in Ref. [52](see Fig. 3.1(b)).

around $\omega = 2$ eV and $\omega = 5.8$ eV. Indeed, ϵ_1 attains small negative values around 2.7 eV and vanishes at 5 eV with ϵ_2 having local minima leading to severely damped plasmon at 2 eV and a broad plasmon peak at 5.3 eV.

Contrarily to the two plasmon-type peaks 1 and 1', the peak $2'$ at 10.5 eV in Fig. 6.1(a) has not been discussed so far. Inspection of ϵ_1, ϵ_2 in Fig. 6.1(b) suggests the collective oscillation nature of this peak ($\epsilon_1 = 0$ and local minimum in ϵ_2). In Fig. 6.1(a) I show comparison of the loss function obtained with the pseudopotential that includes 5d electrons and loss function obtained with the pseudopotential where 5d electrons are frozen in the core. In the latter case, due to the absence of 5d electrons, the well defined Drude plasmon peak is developed at 10.1 eV, close to the peak $2'$, indicating that peak $2'$ might be a remnant of the unscreened bulk plasmon (UP).

Assigning peaks 1 and 2' to the plasmon excitation screened by a second interband transition and to the unscreened plasmon respectively, is backed by the fact that these peaks disperse with the increase of the transferred momentum **q**, which is characteristic of collective excitations and not of interband transitions.

In conclusion, I have shown that signatures of plasmons in EEL spectra of bulk Au are more complex than previously believed.

6.1.2.b EEL spectrum of bulk Au with SOC

In the previous subsection I have reviewed and discussed the EEL spectrum of bulk Au computed without SOC focusing on the low energy plasmon excitations. In order to study the influence of SOC on the bulk Au EEL spectrum and bulk plasmon I have performed simulations for both vanishing and finite transferred momenta **q**. In Figure 6.2, I show the comparison of the EEL spectra of Au within SR and FR approximations along with the dielectric function computed using an optimized norm-conserving pseudopotential with 19 electrons in the valence region. In Fig. 6.3 I show the comparison of experimental REELS spectra and of EEL spectra computed with and without SOC with big peak broadening to mimic the experimental resolution along with the corresponding band structure. As one can see, differences between two spectra are small (Table 6.2 summarizes the SOC induced changes). The main change in peak position involves the unscreened plasmon peak $2'$, which is blue shifted by 0.4 eV and split by 1.5 eV into 2 peaks. The overall shape of the spectrum is left unchanged. In particular, the bulk plasmon peak (marked with an arrow), that is already severely damped and shifted in the SR approximation, remains unchanged. I also note that peak $2'$ is absent in the experimental spectrum and practically disappears in the EEL spectra computed with SOC and with a big value of the peak broadening. For this peak the agreement between theory and experiment is improved with inclusion of SOC.

peak #	ω (eV)	Change in the shape
$1'$ (BP)	2.2	Unchanged
1 (5d BP)	5.3	Loses some intensity
$2'$(UP)	10.9	Split by 1.5 eV and loses intensity
2	15.4	Unchanged
3	24	Loses intensity
4	31	Loses intensity
5	37	Unchanged
6	44	Unchanged

Table 6.2: SOC-induced changes in the peak positions and shape of the EEL spectrum for vanishing $\mathbf{q}$ reported in Fig. 6.4(a).

The influence of the SOC becomes less pronounced for bigger values of the transferred momentum $\mathbf{q}$. In Fig. 6.4 I show the bulk Au EEL spectrum computed for finite values of the transferred momentum $\mathbf{q}$ (0.39, 0.77 and 1.39 Å^{-1}). In Fig. 6.5 I show the absolute difference between spectra computed with and without SOC. While for the smallest $\mathbf{q} = 0.39$ Å^{-1} there are still some difference between SR and FR calculations (i.e. peak 1 is less intense in FR calculation and peak 2 develops only for FR case similar to the case of vanishing $\mathbf{q}$) starting from $\mathbf{q} = 0.77$ Å^{-1} two EEL spectra become very close. The possible reason for this is following: for the small value of $\mathbf{q}$, $e^{-i\mathbf{qr}} \approx 1 - i\mathbf{qr}$ and only dipole-allowed transitions contribute to the spectra. For larger values of $\mathbf{q}$ other transitions start to contribute, thus smearing out the peaks including the peaks that have developed due to the inclusion of SOC in the calculations. The increasing similarity as a function of q is seen in the four panels of Fig. 6.5, where I report the absolute value of the difference in intensity between the FR and SR calculations (black line). Of course, the higher the modulus of the transferred momentum, the smaller the average difference in intensity (red horizontal line).

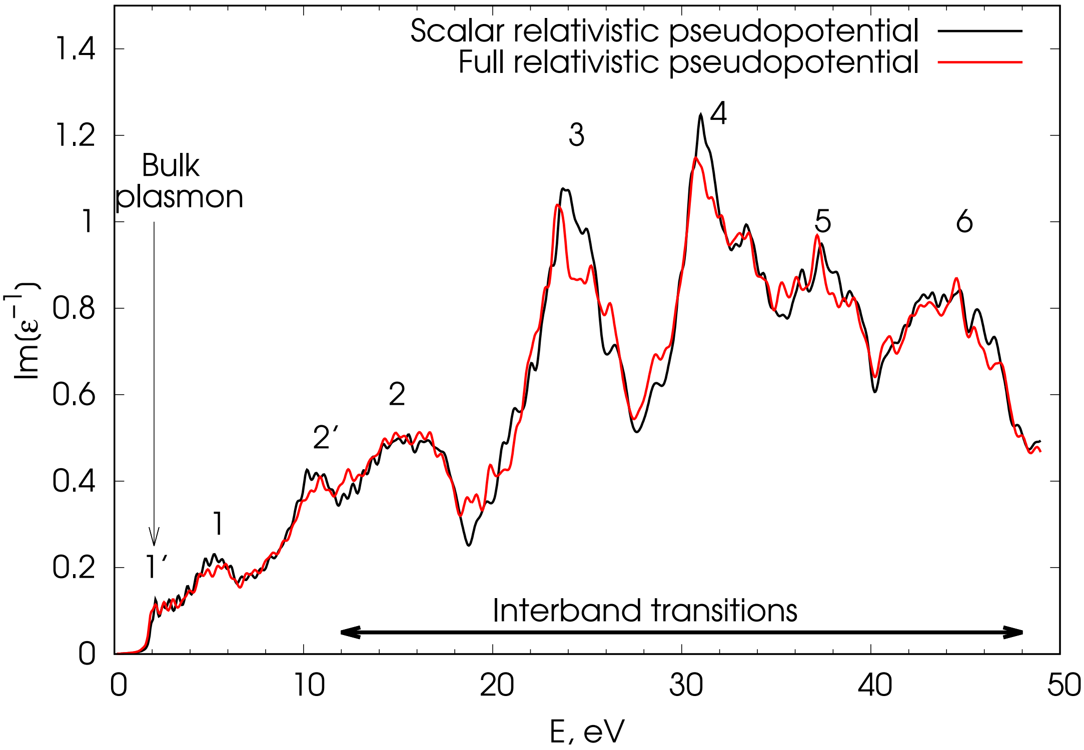

(a)

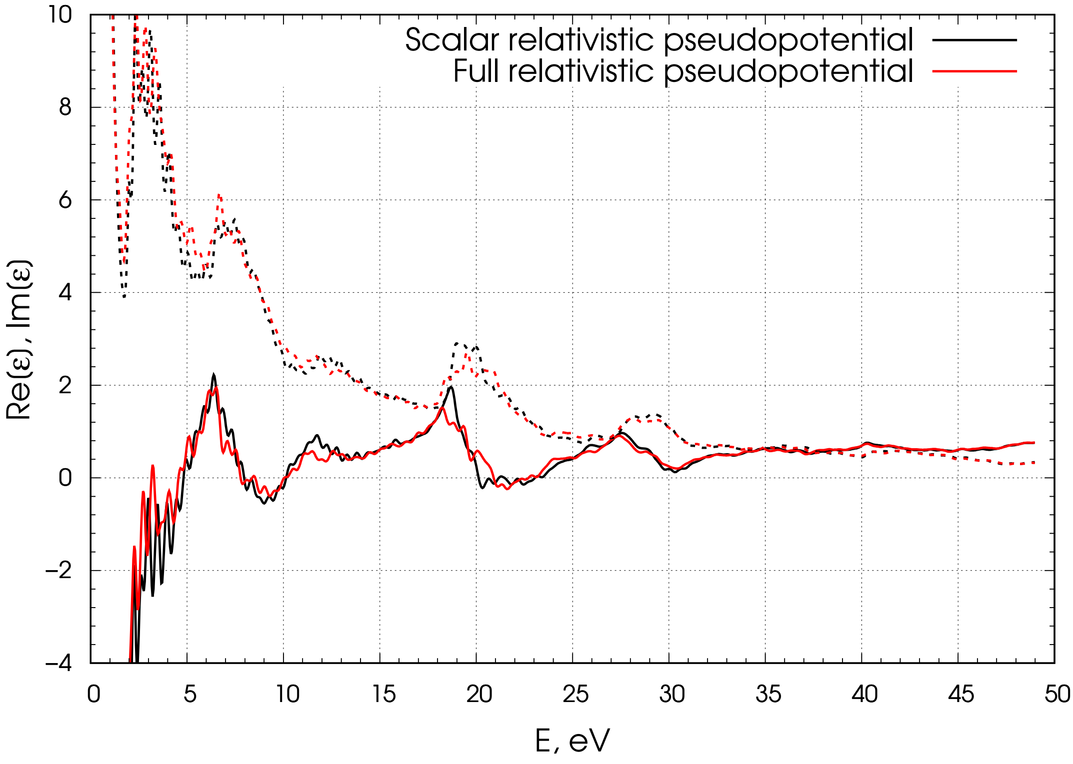

(b)

Figure 6.2: (a)The EEL spectra for bulk Au without (black lines) and with (red lines) SOC calculated at the experiment lattice parameter for vanishing **q**. (b) Real (solid line) and imaginary (dashed line) part of the dielectric function of bulk Au.

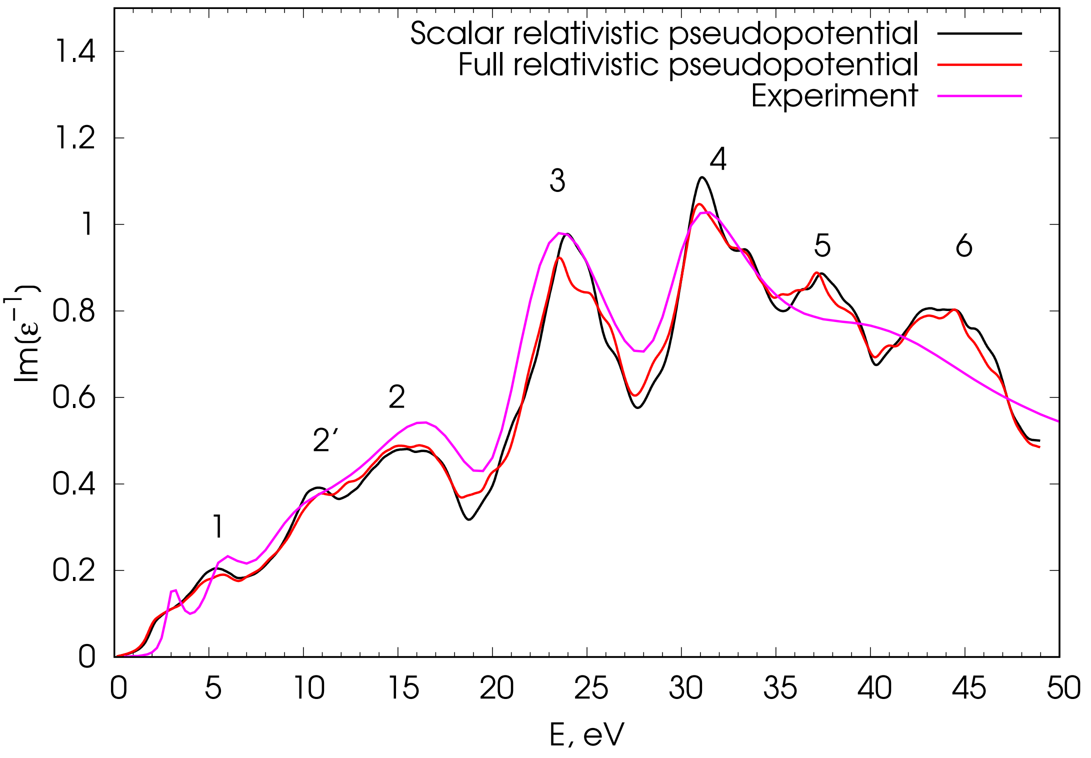

(a)

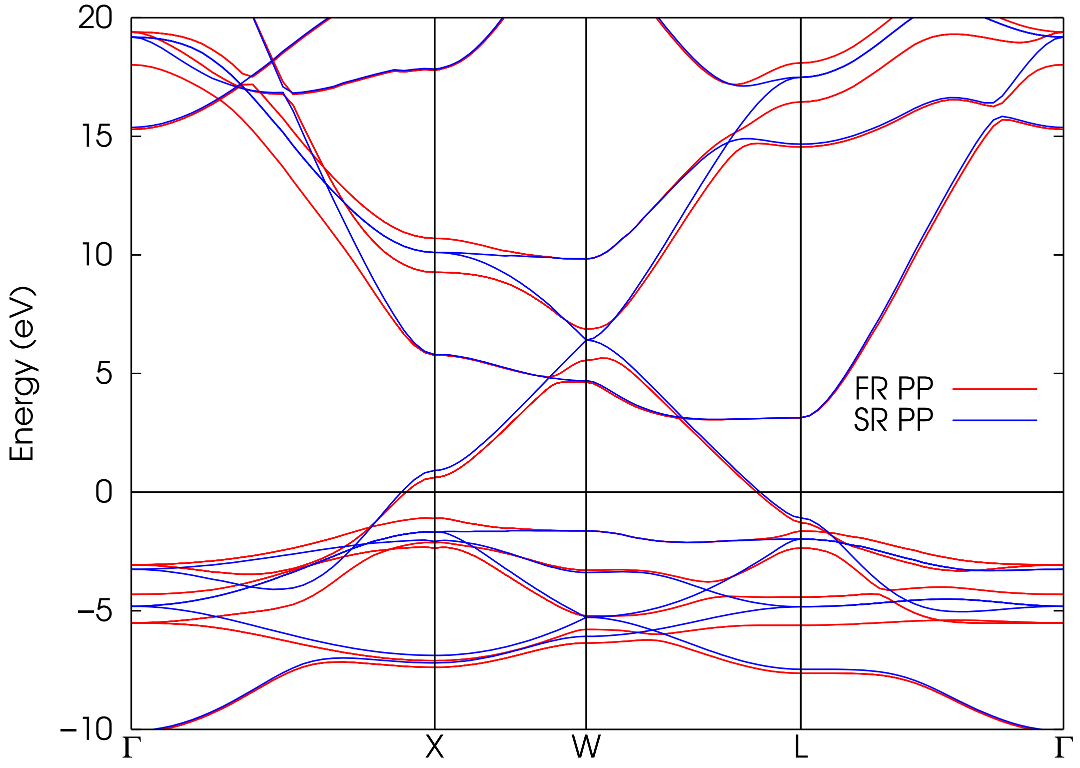

(b)

Figure 6.3: (a) EEL spectra for bulk Au without (black lines) and with (red lines) SOC calculated at the experiment lattice parameter for vanishing $\mathbf{q}$ compared with REELS experiment results (pink line) [57]. (b) LDA Kohn-Sham band structures of bulk Au with (red lines) and without SOC (black lines).

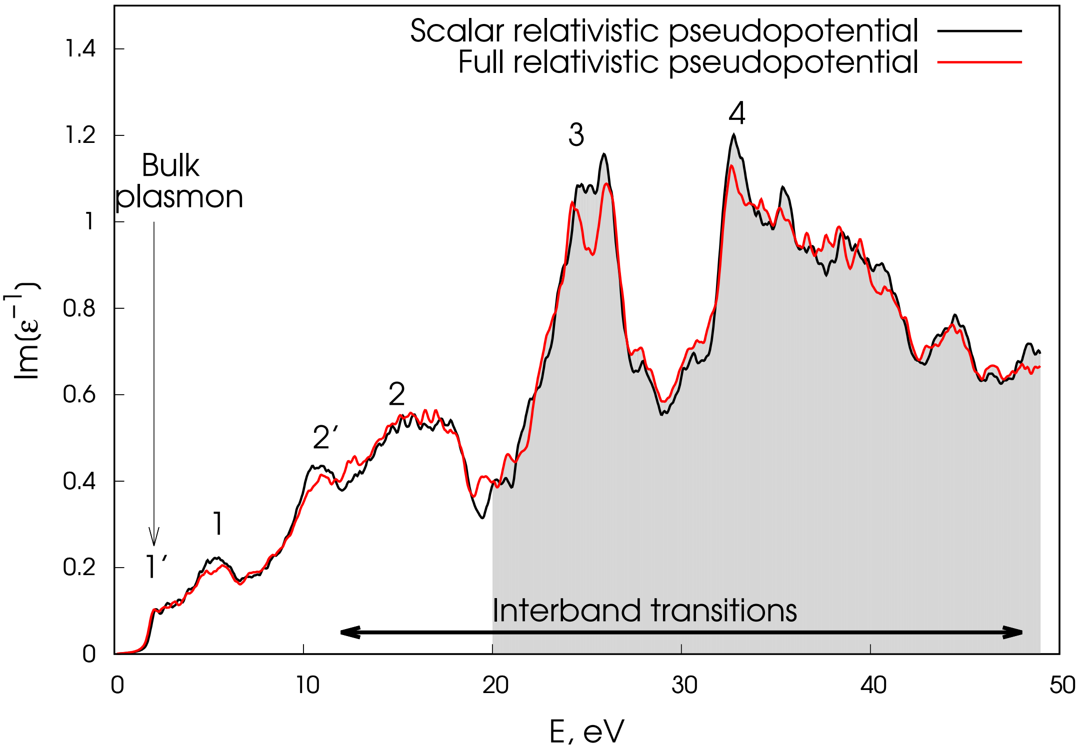

(a)

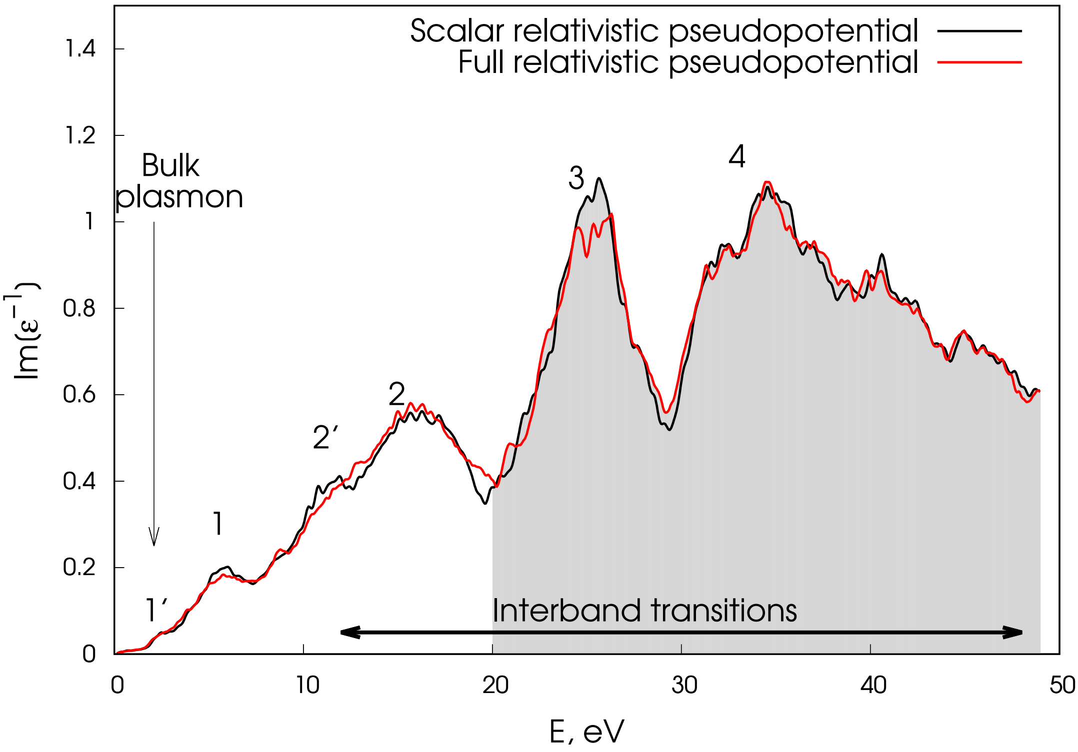

(b)

Figure 6.4: EEL spectra for bulk Au without (black lines) and with (red lines) SOC calculated at the experiment lattice parameter for three different values of $\mathbf{q}$: (a) 0.03, (b) 0.39, (c) 0.77 and (d) 1.39 Å^{-1}. The shaded area represents the energy range where the 11 electron pseudopotential shows some differences with respect to the 19 electron pseudopotential.

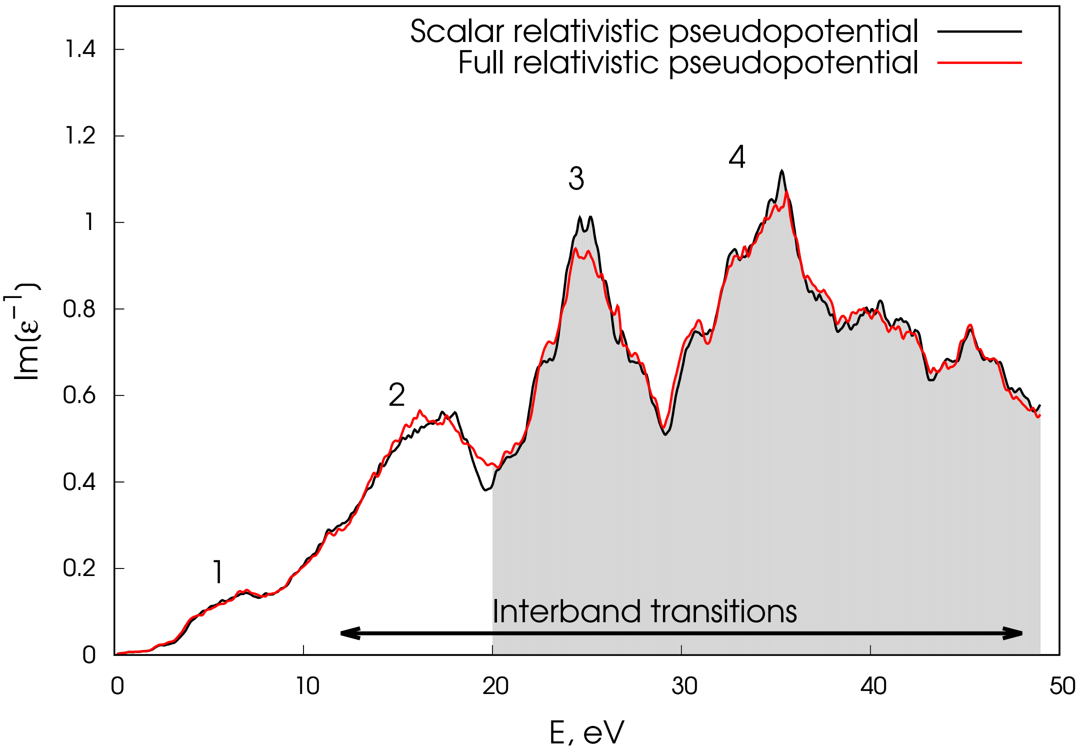

(c)

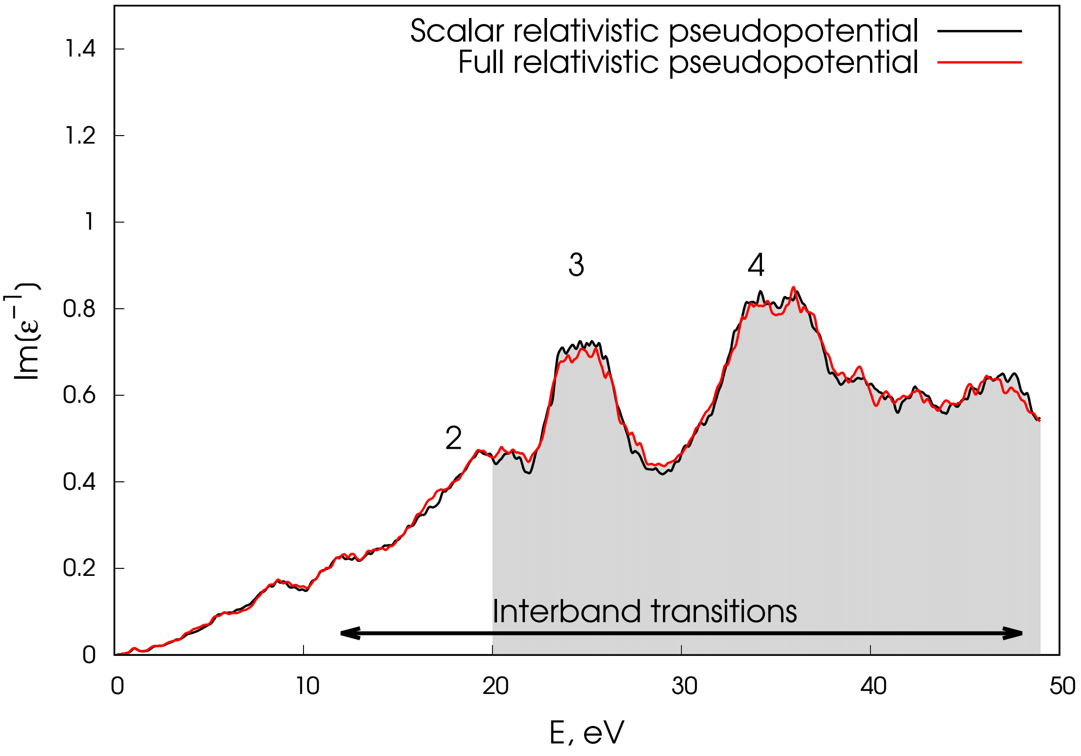

(d)

Figure 6.4: (continued) EEL spectra for bulk Au without (black lines) and with (red lines) SOC calculated at the experiment lattice parameter for three different values of **q**: (a) 0.03, (b) 0.39, (c) 0.77 and (d) 1.39 Å^{-1}. The shaded area represents the energy range where the 11 electron pseudopotential shows some differences with respect to the 19 electron pseudopotential.

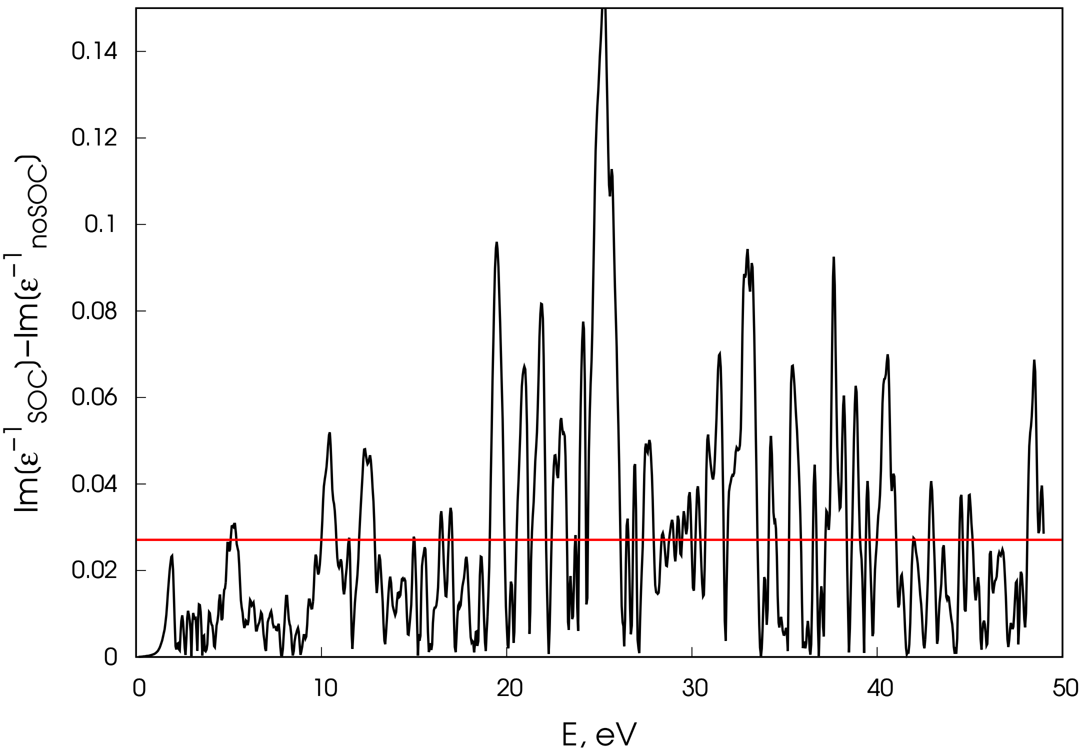

(a)

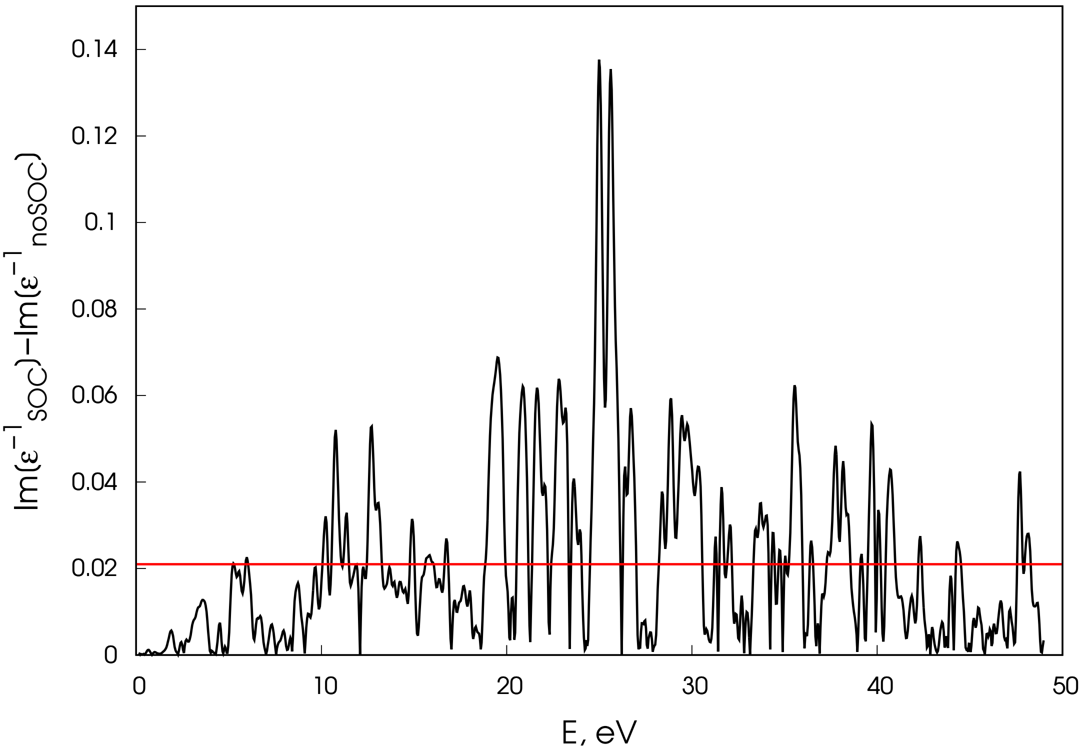

(b)

Figure 6.5: Absolute value (black line) and average (red line) of the difference between EEL spectra obtained with and without SOC spectra for different values of **q** (note the different scale on ordinate axis): (a) vanishing **q** (Fig. 6.4(a)), (b) 0.39 $Å^{-1}$ (Fig. 6.4(b)), (c) 0.77 $Å^{-1}$ (Fig. 6.4(c)) and (d) 1.39 $Å^{-1}$ (Fig. 6.4(d)).

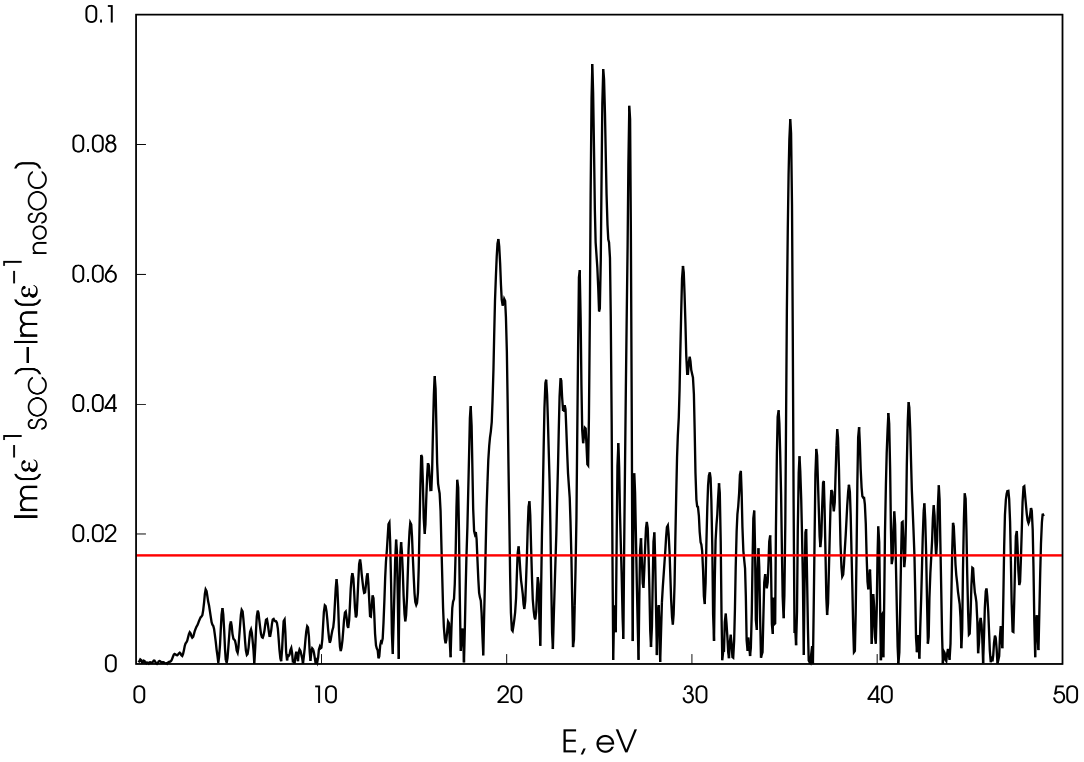

(c)

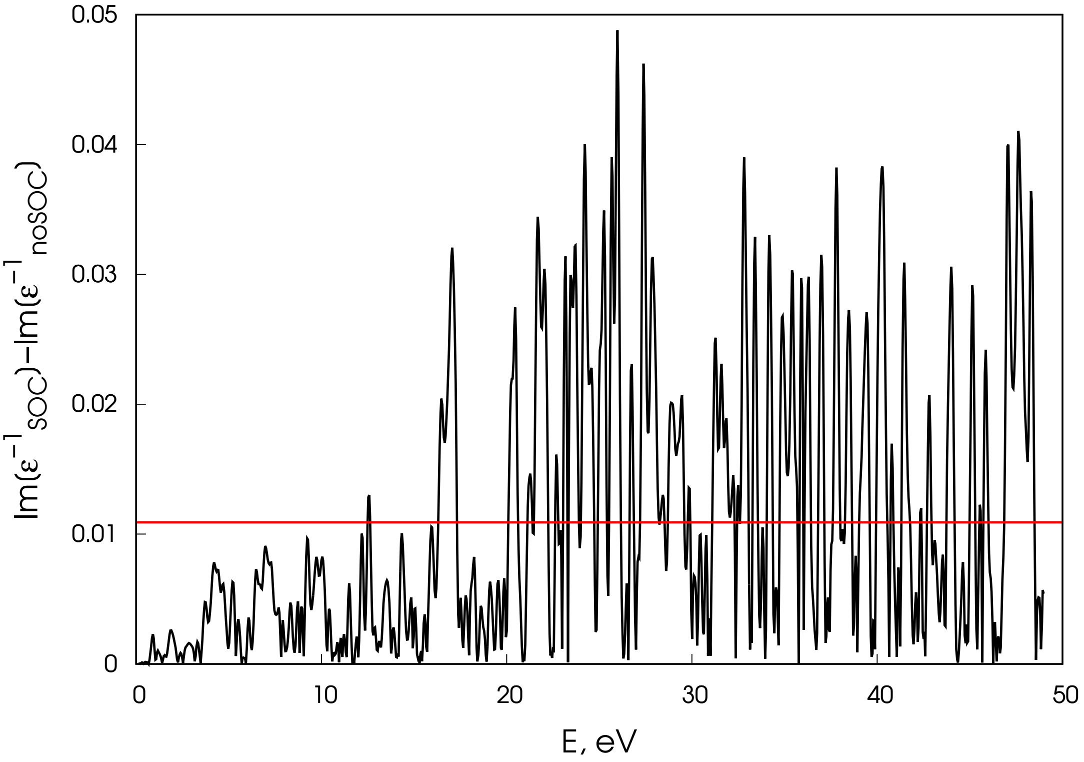

(d)

Figure 6.5: (continued) Absolute value (black line) and average (red line) of the difference between EEL spectra obtained with and without SOC spectra for different values of **q** (note the different scale on ordinate axis): (a) vanishing **q** (Fig. 6.4(a)), (b) 0.39 Å^{-1} (Fig. 6.4(b)), (c) 0.77 Å^{-1} (Fig. 6.4(c)) and (d) 1.39 Å^{-1} (Fig. 6.4(d)).

6.2 Conclusion and perspective

This chapter is devoted to the study of the EEL spectra of bulk Au and, for the first time, to the influence of spin orbit coupling (SOC) on it. First, I have compared the *ab initio* results for EEL spectra of bulk Au calculated with and without SOC for the different values of transferred momentum $\mathbf{q}$. Analysis of the low energy EEL spectra in this region allowed me to assign the peak at 10 eV (labeled $2'$) to the reminiscence of the unscreened bulk plasmon of the $6s$ electron. In conclusion, the inclusion of SOC in the EEL spectrum calculations of bulk Au leads to minor but noticeable modifications of both interband transitions and bulk plasmon peaks in the loss spectra. I have shown that differences between spectra computed with and without SOC fade out for high values of $\mathbf{q}$ and that, as a rule, the higher the transferred momentum the smaller the average effect of SOC on the EEL spectrum. I would like to point out the remarkable agreement of the loss function obtained in the fully relativistic calculation with the experimental loss function obtained in REELS experiment [57] - while positions of peaks $1'$ and 1 are underestimated in LDA, peak $2'$ becomes more damped in the fully relativistic calculation in better agreement with experiment than the scalar relativistic calculation.

Chapter 7

Ab initio calculation of the EEL spectra of the Au(111) surface. Influence of spin-orbit coupling

In this Chapter, the EEL spectra of the Au(111) surface and the influence of spin-orbit coupling (SOC) on the EEL spectrum and the acoustic surface plasmon (ASP) of Au(111) are investigated. The effect of the inclusion of SOC on the EEL spectra of bulk Au has been discussed in Sec. 6.1, where I have shown that it has a small but still noticeable effect. The ASP originates from the Shockley states specific to the surface (see. Sec. 3.1.4). As discussed in Sec. 2.2.2, the surface state of Au(111) is moved by 0.1 eV down in energy and is split into two parabolic states. The influence of SOC on the ASP is studied in the present Chapter. I will start with the discussion of EEL spectra of Au (111) without and with SOC and its comparison with bulk Au EEL spectra from Section 6.1.2. Then I will discuss the ASP of the Au(111) surface, its identification in my calculations and compare my results to other experimental and theoretical works. Finally, I will discuss modifications of the ASP dispersion obtained from EEL spectrum calculations with SOC and discuss the discrepancies between experimental and *ab initio* results. These calculations were made possible because of the theoretical and numerical development reported in Chapter 4.

7.1 Computational details

Calculations have been performed with the same approximation as in Sec. 6.1.2.a, using the same 11 electron ultrasoft pseudopotential and the experimental lattice constant. In order to simulate the surface, the slab supercell approach was used. A supercell was constructed with twenty one layers of gold and a vacuum space of 3 nm between slabs. The sampling of the first BZ was performed using a uniform 24x24x1 $\mathbf{k}$ point mesh centered at the Γ point. A Methfessel-Paxton smearing with a broadening parameter of 0.002 Ry was used for the ground-state calculation. Two Lorentzian broadenings of 0.01 Ry and 0.003 Ry are used to respectively plot the EEL spectrum and to determine the ASP peak position. The calculation for the Au slab with the Pt monolayer was performed by substiting surface Au atoms with Pt atoms without changing the lattice parameter.

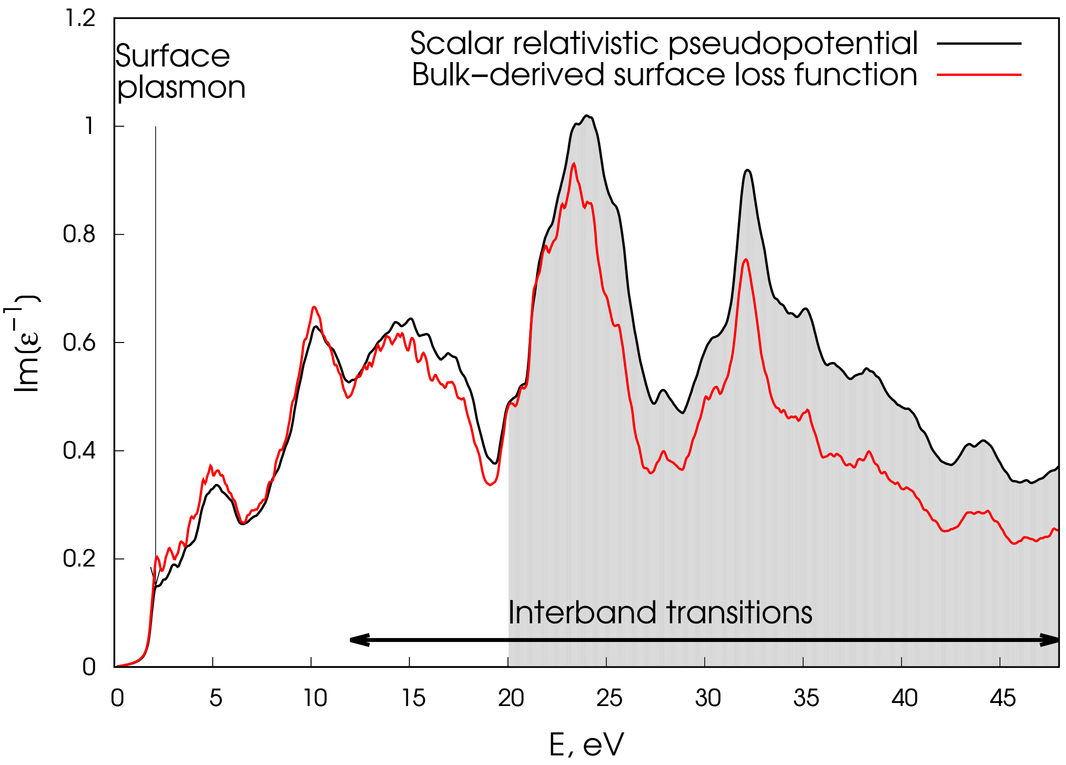

Figure 7.1: Au(111) surface EEL spectrum (black line) compared to the Au(111) EEL spectrum derived from the bulk (Fig. 6.4(a)) using Eq. (7.1) (red line) calculated without SOC. The shaded area represents the energy range where the 11 electron pseudopotential shows some differences with respect to the 19 electrons pseudopotential.

7.2 EELS spectra of the Au(111) surface

7.2.1 The EEL spectra of the Au(111) surface without SOC

Let us first examine the overall EEL spectrum of the Au(111) surface and verify that it is consistent with the EEL spectra of bulk Au and results obtained in other works. In the long wavelength limit the loss function of the semi-infinite solid (neglecting the momentum dispersion) can be written as [38]:

$$L_s(\omega) = -Im\frac{1}{\epsilon(\omega)+1}, \tag{7.1}$$

where $\epsilon(\omega)$ is the frequency-dependent dielectric function of the bulk solid. While in my simulation I have neither a semi-infinite crystal, nor a semi-infinite vacuum above, I still consider the equation above a decent approximation that allows me to distinguish bulk-derived features in the spectrum from surface contributions. Indeed, one can see in Fig. 7.1 that peaks in the surface loss spectra are in a good agreement with peaks in the loss function derived from the bulk dielectric function.

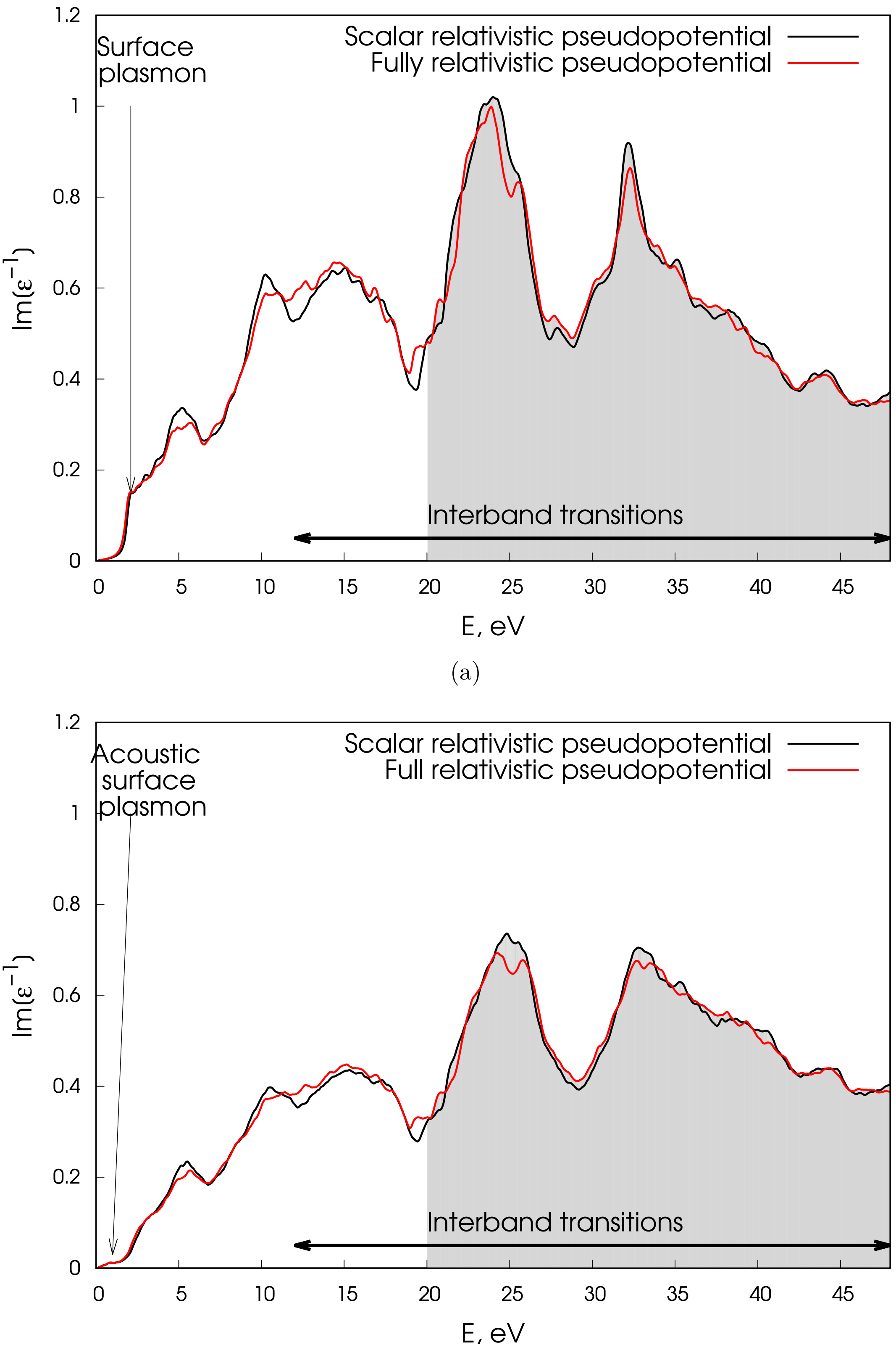

(a)

(b)

Figure 7.2: The Au(111) surface EEL spectra without (black lines) and with (red lines) SOC calculated at the experimental lattice parameter for (a) vanishing in-plane **q** and (b) finite in-plane $\mathbf{q} = 0.175$ Å^{-1}. The shaded area represents the energy range where the 11 electron pseudopotential shows some differences with respect to the 19 electrons pseudopotential.

7.2.2 The EEL spectra of the Au(111) surface with SOC

In Fig. 7.2(a) I report the first Au(111) EEL spectrum calculation with SOC compared to the calculation without SOC from the previous section. SOC does not have a significant influence on the conventional surface plasmon and interband transition peaks of the loss spectrum. In Fig. 7.2 I show EEL spectra of Au(111) for vanishing and finite values of $\mathbf{q}$ with and without SOC. One can see that SOC modifies the same peaks and in the same way as for the bulk Au EEL spectrum discussed in Sec. 6.1.2.b.

7.3 Study of the acoustic surface plasmons

The Au(111) surface can support conventional and acoustic surface plasmons (ASP). While the former is heavily damped and shifted due to the overestimation of the $5d$ band energy in LDA, the latter originates from the surface state that is well described by DFT-LDA [34]. ASP has a linear dispersion $\omega \sim \alpha v_F q$, thus there is no ASP peak in the EEL spectrum with vanishing $\mathbf{q}$, however it appears for the higher values of $\mathbf{q}$ as it is seen on the zooms of the EEL spectra for $\mathbf{q} = 0.025$ Å^{-1} and $\mathbf{q} = 0.175$ Å^{-1} in Fig. 7.3. Here I point out that while it is enough to perform 2500 iterations to obtain the converged EEL spectrum for E>1.5 eV, additional (up to 4000) Lanczos iterations are required to obtain the converged ASP peak. Moreover, SOC-induced splitting of the Shockley state into two surface states could potentially lead to two acoustic surface plasmon modes. I will show that actually this is not the case in my calculation.

7.3.1 ASP identification

In section 3.2.4 I have explained the methods used so far to identify ASP in previous experimental and theoretical studies. Due to the nature of the Liouville-Lanczos method used to calculate EEL spectra it is not possible to directly assign the excitations that appear in the loss spectrum to certain bands and transitions, adding some complexity to the analysis of the results. In the present work I have performed several tests that allow an indirect identification of the low-energy peak in EEL spectra as the Shockley surface state derived ASP excitation:

1. ASP is an in-plane excitation, i.e. it requires the transferred wave-vector to be in the plane parallel to the surface-vacuum interface. I have performed the EEL spectrum calculation for $\mathbf{q}$ in the direction perpendicular to the surface and I have not observed any meaningful excitations in the low-energy part of the spectrum. This fact suggest that the excitation observed when $\mathbf{q}$ is in-plane has a surface nature.

2. In order to check whether the low energy peak is connected to the surface state, I have performed the EELS calculation for the Au(111) surface covered with a monolayer of Pt and have not observed any ASP like peak, as such a surface support

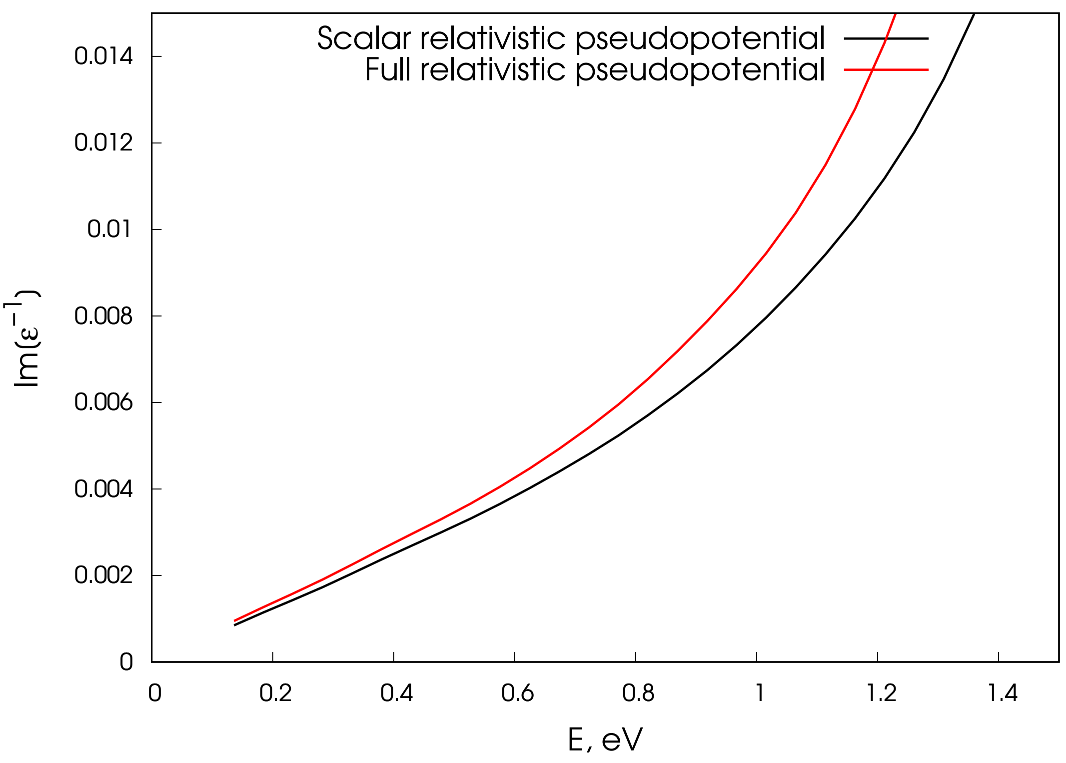

(a)

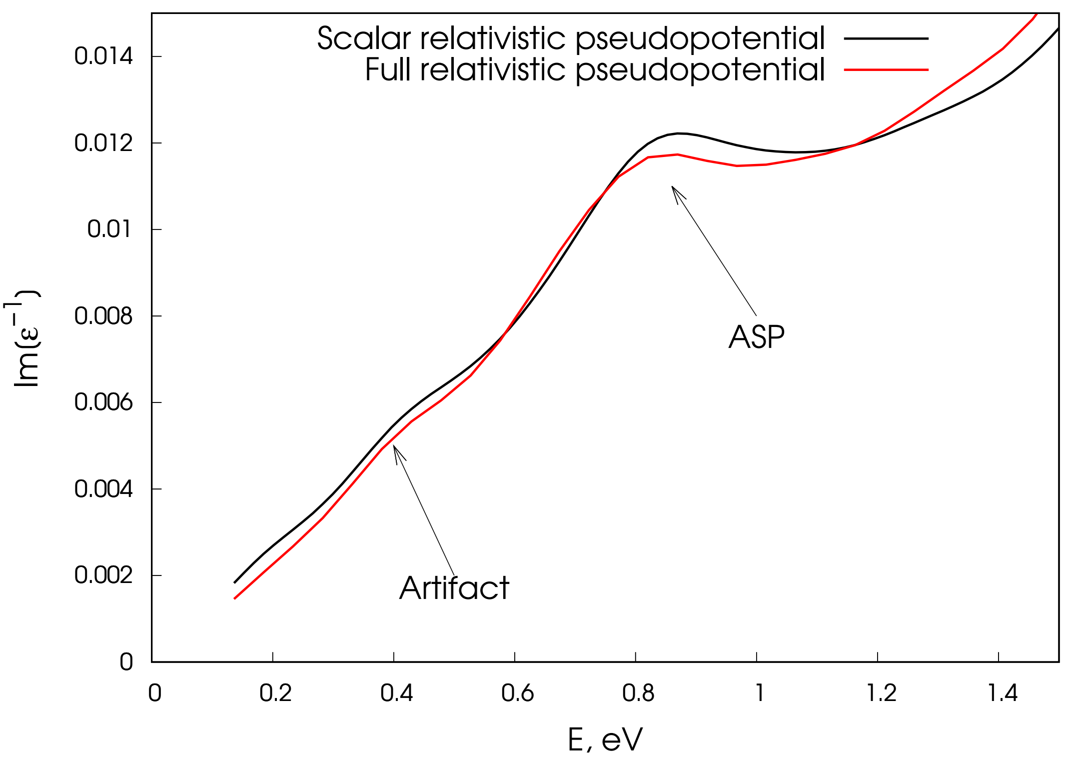

(b)

Figure 7.3: Zoom of the EEL spectra reported in Fig. 7.2 showing (a) the absence of the ASP peak for $\mathbf{q} = 0.025$ Å^{-1} and (b) the presence for $\mathbf{q} = 0.175$ Å^{-1}.

only an unoccupied Shockley-like surface state, and thus, the ASP cannot be excited in this system.

3. I have performed an EEL spectrum calculation for the bulk Au using the unit cell with the hexagonal geometry (like the unit cell for Au(111)) in order to verify that the observed low-energy excitation I assign to ASP is neither a bulk derived excitation nor a numerical artifact coming from the system geometry.

4. I have compared the loss function shown in Ref. [58] for Au(111) with the loss function from my calculations. As one can see in Fig. 7.5(b) the shapes of the two loss functions are very similar to each other with the ASP peak position in my calculation being 0.04 eV higher than in Ref. [58]. Keeping in mind that I use a different approach (the Liouville-Lanczos approach in the ultrasoft pseudopotential scheme *versus* the solution of the Dyson equation in the projector augmented wave scheme) and different exchange and correlation functional (LDA versus GLLB-sc) I conclude that a very good agreement between the two calculations is reached.

Finally, the results I have obtained agree well with previous *ab initio* calculations performed in Refs. [58, 13] in the scalar-relativistic theory (Fig. 7.7(a)). By itself each of the performed test is not enough to assign the observed excitations to ASPs. Together they give a certain degree of confidence in the identification of these excitations as ASPs. I estimate a maximum error bar of the ASP peak position in my calculation to be ~ 0.03 eV.

7.3.2 Position of the electron-hole continuum

In Ref. [58, 13] *ab initio* studies of the ASP dispersion of Au(111) have been performed in the SR theory. In both works the ASP had a dispersion close to linear, $\omega_{ASP} = \alpha v_f^{2D} q$, with $\alpha < 1$, meaning that the ASP mode runs inside the continuum for intraband electron-hole excitations within the Shockley surface state (SS) band. The electron-hole continuum has been reported in Fig. 7.7(a) as dashed and dot-dashed line to the upper edges of bulk and Shockley state electron-hole pairs continuum respectively. Both have been computed in the following way:

$$E_{e-h}(q) = E(k_f + q) - E(k_f), \tag{7.2}$$

where E_{e-h} denotes the edge of electron-hole pair continuum at a wavevector q, $E(k)$ corresponds to the energy of the electron band of interest (bulk band that crosses the Fermi level or Shockley state) at wavevector k and k_f is the Fermi wavevector.

7.3.3 Electron velocity in the surface state

It has been argued in Ref. [13] that $\alpha < 1$ is a result of the incomplete dynamical screening of the majority of slow bulk electrons by fast surface electrons is Shockley SS, contrary to the previous predictions [17, 18]. However, authors of Ref. [58] suggested that the ASP dispersion is governed by the surface mode in the dielectric band structure (see Sec. 3.2.4) rather than by the Fermi velocity of the surface state, as the rigid shift of the

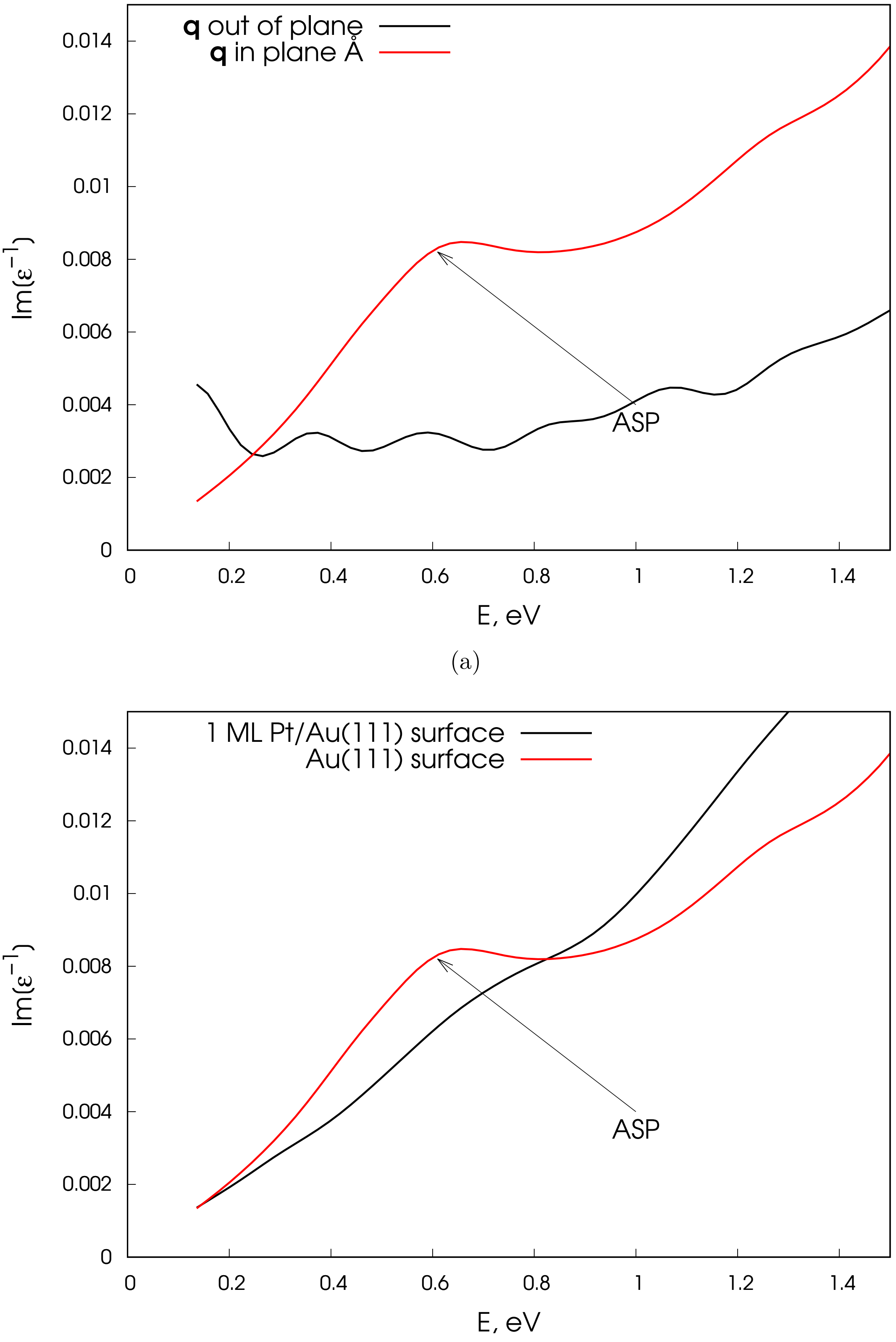

(a)

(b)

Figure 7.4: (a) The Au(111) EEL spectrum computed for $\mathbf{q} = 0.125$ Å^{-1} in (red) and out (black) of the surface plane; (b) pure Au(111) EEL spectrum (red) and Au(111) with one monolayer of Pt EEL spectrum (black) for $\mathbf{q} = 0.125$ Å^{-1}.

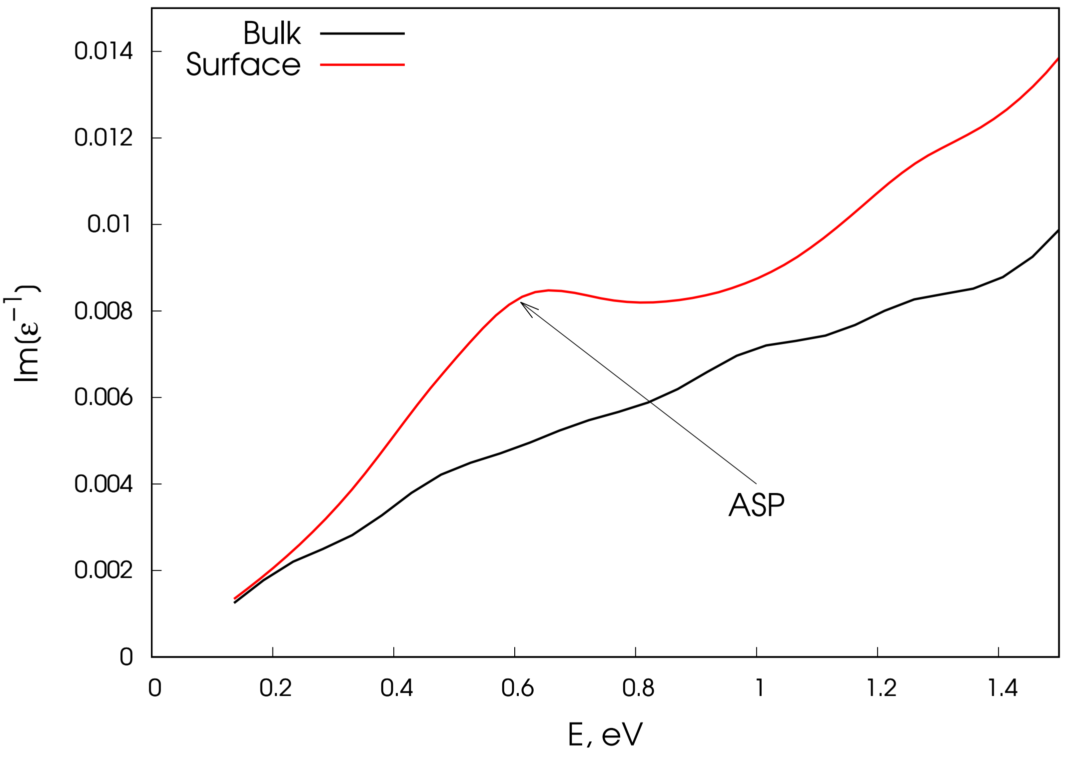

(a)

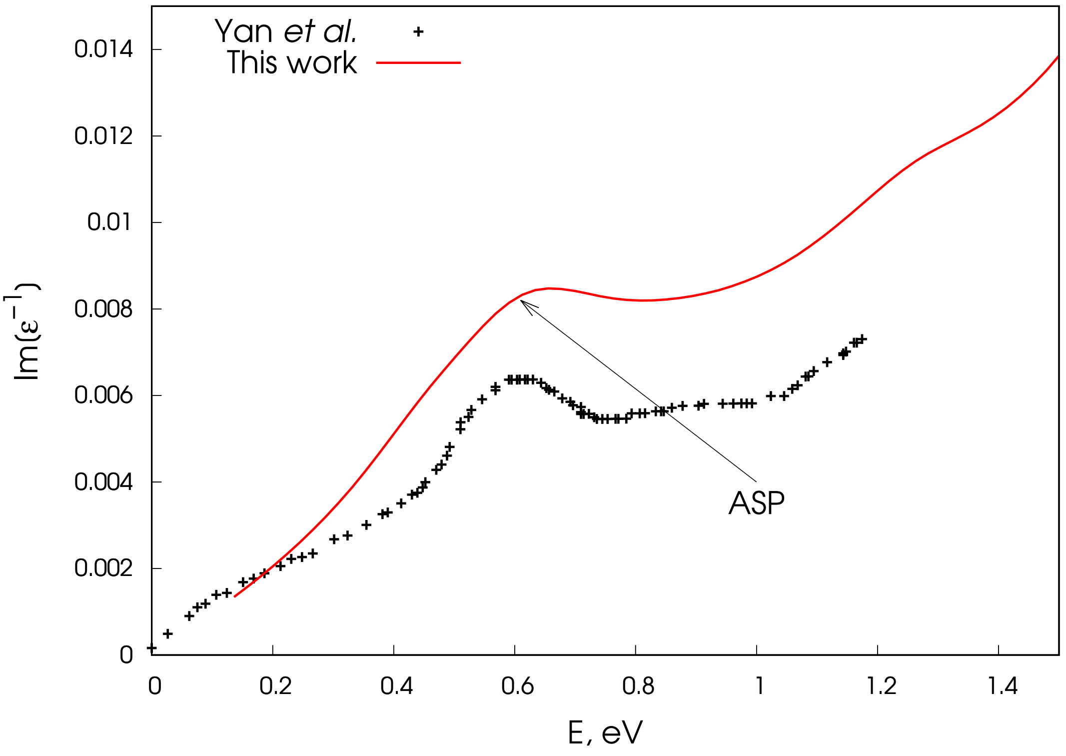

(b)

Figure 7.5: (a) Au(111) EEL spectrum (red) and bulk Au EEL spectrum (black) in the same geometry as Au(111) computed for $\mathbf{q} = 0.125$ Å^{-1}; (b) Au(111) EEL spectrum obtained in this work (red) and in Ref. [58](black crosses) for $\mathbf{q} = 0.125$ Å^{-1}.

Calculation	SR	FR	SR shifted
v_F^{2D}, a.u.	0.36	0.4, 0.38	0.385
$< v_F^{2D} >$, a.u.	-	0.39	-

Table 7.1: Fermi velocities v_F^{2D} of the surface states in my calculation (see also Fig. 7.6). $< v_F^{2D} >$ is the average of Fermi velocities in the cases where there are more than one state (FR).

surface band (and thus the change in v_f) does not result in significant modification of the ASP energies. While the method I use does not presently provide an access to the dielectric band structure, one might assume that SOC will not change it significantly as I will explain now. The Fermi velocity for the surface state does not change drastically as one can see in Fig. 7.6 where I report the velocity of the surface state of Au(111). One can see that the v_f^{2D} is slightly higher for the surface state doublet obtained with SOC mainly due to the lower position of the Shockley surface state in the SOC case: if the Shockley obtained without SOC is shifted down by 0.1 eV in energy (black dashed line), the behavior of the velocity matches the case with SOC. Potentially, splitting of the Shockley surface state into two could lead into splitting of the ASP into two, however since the difference between v_f^{2D} of the two Rashba split states is $\sim 6\%$ it is most probable that a single excitation will be observed.

7.3.4 Dispersion of the ASP without SOC

In order to obtain the ASP dispersion and compare it to theoretical results from previous works [58, 13], I have performed 5 EEL spectrum calculations for different values of $\mathbf{q}$ without SOC and tracked the position of the ASP peak in the low-energy part of each spectrum. The resulting dispersion is shown in Fig. 7.7.

7.3.5 Dispersion of the ASP with SOC

In order to study the influence of SOC on the ASP, I have performed 5 EEL spectrum calculations for different values of $\mathbf{q}$ taking SOC into account. To my knowledge this is the first report of the calculation of EEL spectra for the Au(111) surface with SOC. Despite the Rashba splitting of the Shockley state, only one ASP peak is observed in obtained spectra. The resulting ASP dispersion in the FR theory is reported in Fig. 7.7(b) together with my SR calculation and experimental results [80]. As one can see in this figure, the inclusion of SOC does not lead to a significant change in the ASP behavior: the difference between the ASP energy for the biggest value of $\mathbf{q}$ amount to 0.04 eV.

7.3.6 Slope of the ASP dispersion

In Table 7.2 I summarize the value of α (see Sec. 3.1.4) obtained from the linear fit $\omega_{ASP} = \alpha v_F^{2D} q$ of the ASP dispersion in different works. In this fit I have used values of the unshifted v_F^{2D} in the SR case and the average $< v_F^{2D} >$ in the FR case reported in

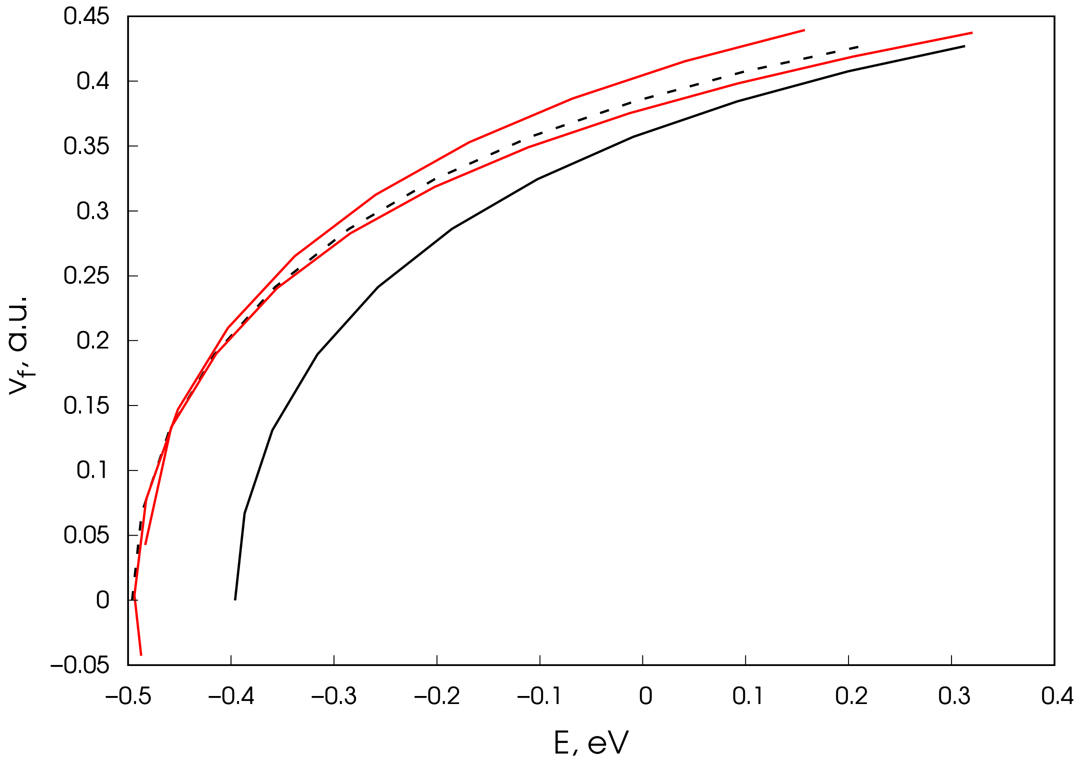

Figure 7.6: Au(111) surface electron velocity distribution vs. energy of the surface state without (black line) and with (red lines) SOC. The black dashed line corresponds to the surface state obtained without SOC and shifted downwards in energy by 0.1 eV to mimic the effect of SOC energy shift.

Source	SR	FR	SR (Ref. [58])	SR (Ref. [13])	Experiment (Ref. [13])
α	0.9	0.81	0.95(?)	0.96, 1.02	0.83, 0.89
v_F^{2D}, a.u.	0.36	0.39	0.35(?)	0.35	0.35

Table 7.2: Summary of the linear fits ($\omega_{ASP} = \alpha v_F^{2D} q$) of ASP dispersion obtained in the different works shown in Fig. 7.7. Authors of Ref. [58] have not given their value for the effective mass nor the surface state Fermi velocity so they were assumed to be similar to other works, the two values of α for Ref. [13] correspond to fit up to $\mathbf{q} = 0.15\text{Å}^{-1}$ and $\mathbf{q} = 0.25\text{Å}^{-1}$ respectively.

the table 7.1. Here one can see that the inclusion of SOC does not lead to a significant modification of the ASP dispersion, thus the discrepancy between the theoretical and experimental results remains. In fact the coefficient α of the ASP dispersion calculated with SOC is slightly lower than α of the ASP dispersion calculated without SOC, however taking into account the error bar of the ASP peak position determination ($\sim$ 0.03 eV) this difference can be considered as small. The agreement between experimental and *ab initio* results is excellent for $\mathbf{q} < 0.15$ Å, however for larger momenta *ab initio* calculations overestimate the ASP energy obtained in experiments.

7.3.7 Discussions

The disagreement between calculations and experiment cannot be attributed to the decay of the ASP into electron-hole pair excitations (see Sec. 7.3.2), since the ASP dispersion curves run entirely inside both bulk and Shockley state electron-hole pair continuum as one can see in Fig.7.7(a). Thus, it is important to discuss further possible sources of discrepancy, since the introduction of SOC does not resolve it. First, it is possible that the accuracy of the measured ASP peak positions becomes lower for bigger values of $\mathbf{q}$, where all of the three theoretical results ([58, 13] and mine) start to deviate from the experimental one. It was pointed out in the study of ASP of Cu(111) [15] that for higher transferred momenta, the most prominent feature in the low energy part of the spectra is wide and contains various contributions. Thus unambiguous identification of the ASP peak in the spectra becomes a challenging task for the experimentalists. Second, it is possible that I have not accounted for all effects that can influence ASP - in my calculations I have used the simple LDA approximation for the exchange-correlation functional which however seems appropriate for the surface states (see 5). It is also known that the DFT does not provide an accurate description of image states that can interact with the surface state [81].

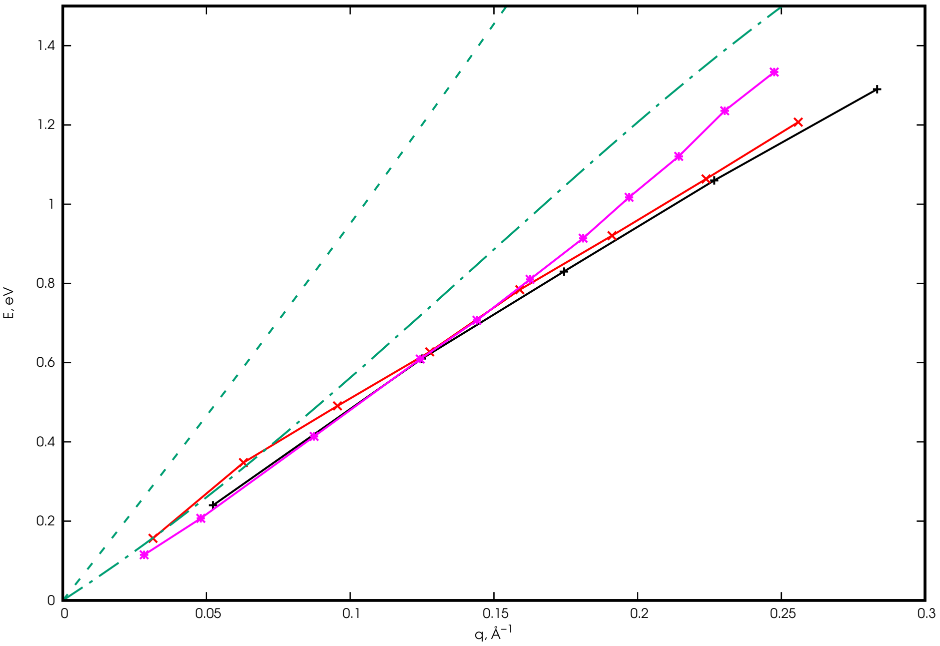

(a)

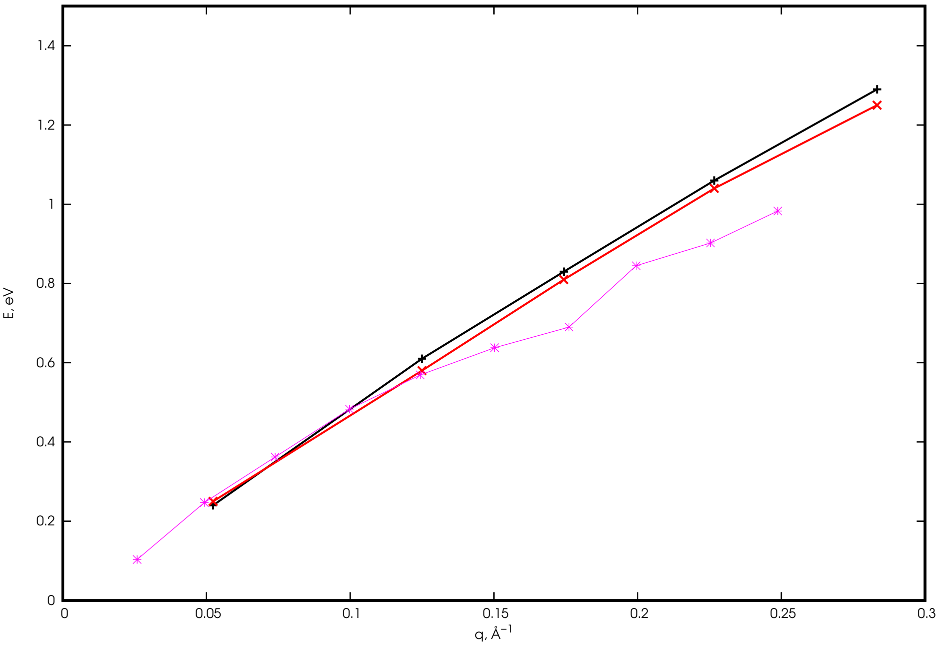

(b)

Figure 7.7: *Ab initio* acoustic surface plasmon dispersion of the Au(111) surface. (a) Comparison of SR *ab initio* ASP dispersion (black line) with SR *ab initio* calculations of Ref. [58] (magenta line) and Ref. [13] (red line). The green dotted and dash-dotted lines represent the upper edges of bulk and Shockley electron-hole pair continuum respectively (b) Comparison of the ASP dispersion obtained with (black line) and without (red line) SOC with the experimental results [13] (magenta line). Black and red lines correspond to the calculation with and without SOC respectively. Calculations have been performed for a slab with 21 layers of gold atoms and 3 nm of vacuum.

7.4 Conclusion and perspective

This chapter is devoted to the study of the influence of spin orbit coupling (SOC) on the EEL spectra of the Au(111) surface and on the acoustic surface plasmon (ASP) excitation of the Au(111) surface, as well as the comparison with previous experimental and theoretical studies performed without inclusion of SOC. First, I have compared the *ab initio* results for the EEL spectrum of the Au(111) surface for small $\mathbf{q}$ without SOC to the EEL spectrum of bulk Au, showing that indeed, the majority of peaks in the EEL spectrum of the Au(111) surface originates from bulk excitations. Then I have shown that the effect of SOC on the EEL spectrum of the Au(111) surface is similar to the one of the EEL spectrum of bulk Au discussed in Chapter 6 - small but noticeable. Finally I have studied the ASP dispersion with SOC and compared it to previous experimental and *ab initio* results obtained without SOC. I have seen that the inclusion of SOC does not modify significantly neither the intensity nor the position of the ASP peak in EEL spectra, suggesting that there might be other factors contributing to the discrepancy between the experimental and *ab initio* results. Nevertheless, I can conclude that the Liouville-Lanczos approach used in this work allowed to study, for the first time, the influence of SOC on the EEL spectra of the Au(111) surface as well as the ASP excitation of the Au (111) surface. Obtained results suggest that SOC leads to small modifications, with all of the most prominent features already captured in scalar-relativistic calculations. They also suggest that *ab initio* study of the vicinal Au(788) surface, where ASP has been experimentally observed [16], and of the Au(455) surface,, can be performed within a scalar-relativistic approximation.

Chapter 8

The EEL spectra and the acoustic surface plasmon of the Au(455) surface.

This chapter is devoted to the *ab initio* study of the EEL spectra and acoustic surface plasmon (ASP) of the vicinal Au(455) surface.

As I have briefly discussed before, the ASP has a sound-like dispersion and is able to confine light to a much higher degree compared to conventional surface plasmons (CSP). This property is ideal for various applications, i.e. propagation of wavepackets without a distortion. However, the excitation of the ASP with light remains an open question - for example a grating of the surface used to excite CSP should be performed on the atomistic level to allow coupling of light to ASP. Stepped surfaces, on the other hand, have a potential to support ASP as it has been shown experimentally for Au(788) [16] and provide the required atomic level grating.

In this chapter I will focus on the *ab initio* study of the stepped Au(455) surface whose structure is similar to the Au(788) surface but not as hard from the computational point of view. I note that to my knowledge it is the first EEL spectrum calculation for a periodic system of such a size, that was made possible thanks to the development of the Liouville-Lanczos approach for TDDFPT in past works and implementations done in Chapter 4. I will first briefly discuss the overall EEL spectrum of the Au(455) surface and show its similarities to the EEL spectrum of Au(111). Then I will discuss the ASP dispersion for the Au(455) surface and compare it to that of the Au(111) surface. Finally I will draw some conclusions and discuss the future perspectives.

8.1 Calculation details

Calculations have been performed within the same approximation as in Sec. 6.1.2.a using the same 11 electron scalar relativistic ultrasoft pseudopotential and the experimental lattice constant. Effects of SOC were not included in the present work. In order to simulate the surface the slab supercell approach was used. The Au(455) surface has been modeled with a 5 nm thick slab and 5 nm of vacuum in the supercell. The slab contains 209 Au atoms and sampling of the first Brillouin zone has been done using a 16x2x1 Monkhorst-Pack **k**-point mesh. The Methfessel-Paxton smearing with a broadening parameter of 0.02 Ry was used for the ground-state calculation. 10000 Lanczos iterations have been performed for each value of **q** in order to obtain a converged ASP peak.

8.2 The EEL spectrum of the Au(455) surface

8.2.1 Vanishing transferred momentum

Let us start with the EEL spectrum of the Au(455) surface for the vanishing transferred momentum and compare it to the spectrum of the Au(111) surface computed in Chapter 7. In Fig. 8.1 I report the EEL spectrum of the Au(445) and Au(111) surfaces for vanishing value of **q** in the direction perpendicular to the step. As one can see in the region of interband transitions ($E > 12$ eV) most peaks remain similar in both position and intensity showing that indeed most of the Au(455) spectrum is Au(111)-derived. However, contrarily to the Au(111) surface where the conventional surface plasmon is so damped that it becomes practically indistinguishable [58], one can see in Fig. 8.1 that the CSP is more pronounced on the Au(455) surface. This could mean that the screening of the CSP by $5d$ bands for the Au(455) surface is weaker compared to the Au(111) surface, most probably around the step, as the terrace itself consists of the Au(111) plane. It is also possible but less probable that the CSP emerges as a result of some unaccounted numerical or convergence error, like a spurious interaction between step edges of the opposite sides of the slab due to a (supposed) insufficient slab thickness that was absent for the flat Au(111) surface.

8.2.2 Finite transferred momentum

While for a vanishing momentum the two EEL spectra reported in Fig. 8.1 do show some differences, i.e. the CSP peak is more pronounced in the loss function of the Au(455) surface, these differences fade out for a bigger value of **q**. In Fig. 8.2 I report the EEL spectrum of the Au(111) and Au(455) surfaces for $\mathbf{q} = 0.226$ Å^{-1} in the direction perpendicular to the step. As one can see the two EEL spectra become nearly identical for this value of **q**. Thus one can tentatively conclude that while the spectrum for $\mathbf{q} \to 0$ is sensitive to the surface geometry, the spectrum at finite **q** is less sensitive to it. A confirmation of this hypothesis would require calculations for more different values of **q** and for the surface with different, but similar geometry, for instance Au(788).

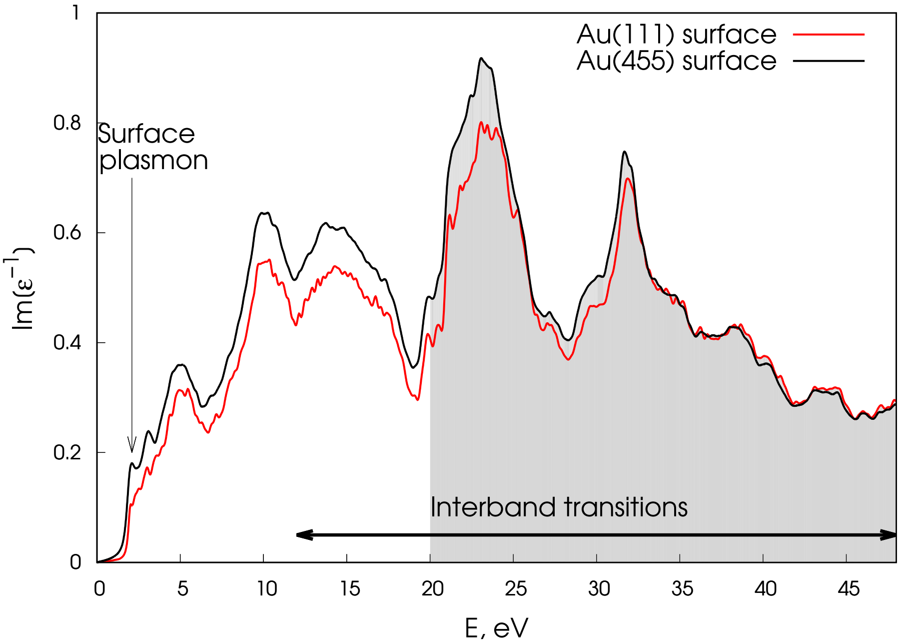

Figure 8.1: Au(455) (black line) and Au(111) (red line) EEL spectra for vanishing $\mathbf{q} \to 0$ in the direction perpendicular to the step. The shaded area represents the energy range where the 11 electron pseudopotential shows some differences with respect to the 19 electron pseudopotential.

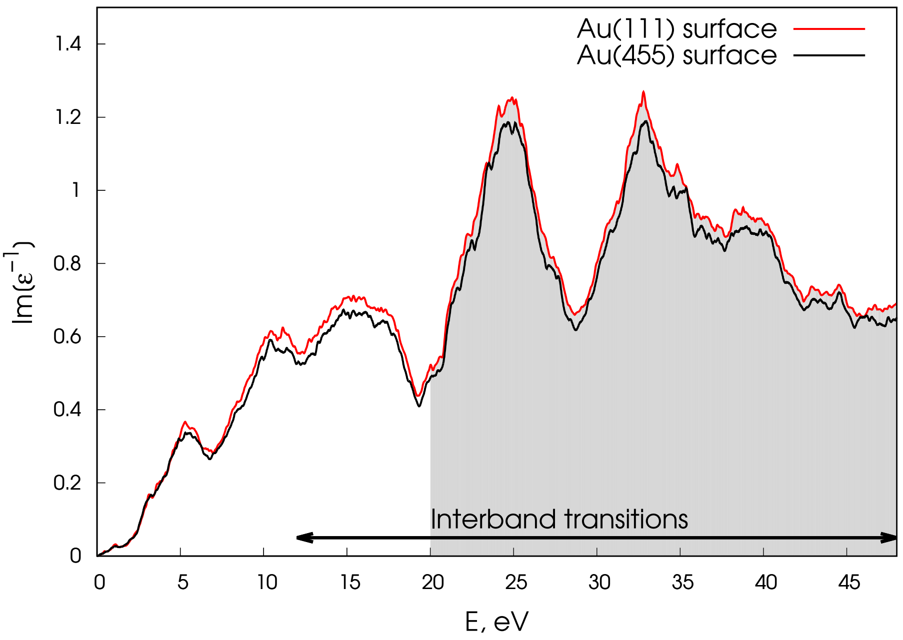

Figure 8.2: Au(455) (black line) and Au(111) (red line) EEL spectra for vanishing $\mathbf{q} = 0.226$ Å^{-1} in the direction perpendicular to the step. The shaded area represents the energy range where the 11 electron pseudopotential showns some differences with respect to the 19 electron pseudopotential.

8.3 Acoustic surface plasmons

8.3.1 Aim of the work

One of the main objectives of the present PhD work is the study of the effects of the structural geometry on the ASP. This requires to study EEL spectra for surfaces other than the Au(111) surface. The surface geometry has been reported for Au(111), Au(322), Au(455) and Au(788) in Chapter 5. For the Au(322) surface in spite of the interest for the resonant surface state seen in the band structure, it was shown that the miscut angle (11.4°) is too large to support the surface state in the projected band structure gap. Thus it is expected to hinder the excitation of the ASP on the Au(322) surface, as in the case of the surface resonance it is only weakly localized on the surface and heavily mixed with the underlaying continuum of bulk states and I do not expect it to give a rise to an ASP excitation. ASP on the Au(111) surface has been studied both theoretically (Refs. [58, 13] and Chapter 7 of this thesis) and experimentally [61, 13] and the ASP on the Au(788) surface has been studied experimentally in Ref. [16] with a simple model used to calculate a theoretical ASP dispersion.

8.3.2 Computational compromise

In my work it has been decided to study the Au(455) surface as it offers a convenient compromise. On the one hand, it is a stepped surface where a partial confinement of the Shockley surface state was observed in my calculations, thus making it similar to the Au(788) surface from this point of view. On the other hand, as the terrace width is smaller in the Au(455) surface compared to the Au(788) surface (23 Å versus 39 Å) the size of the supercell required to model the slab of the same thickness is considerably smaller which allows to reduce the overall computational cost of the EEL spectrum calculations for the Au(455) surface. The ultimate price to pay for this decision is an absence of the experimental data for the ASP of the Au(455) surface, as in the experiments this surface is not stable and undergoes strong reconstruction [44]. It was also decided not to include spin-orbit coupling in these calculation as according to the results I have shown in the Chapter 7 it has a relatively small effect on the ASP dispersion of the Au(111) surface, while inclusion of SOC increases the spent CPU time at least by a factor of 4. Nevertheless, the cost of such calculations remains high - a calculation of a EEL spectrum for a single value of $\mathbf{q}$ takes approximately 145000 cluster core-hours on 4320 cores and requires about 6800 GB of RAM on the JUWELS cluster (Jülich, Germany), while a similar calculation but for the Au(111) surface takes around 4000 core-hours on 720 cores and requires 300 GB of RAM on the same cluster.

8.3.3 Electron velocity in the surface state of Au(455)

Similarly to Section 7.3.3, I start with the inspection of the electron velocity in the Shockley surface state. In Fig. 8.4 I report the electron velocity distribution of the surface state across the step (along the red line in the first Brillouin zone of the Au(455) surface shown in Fig. 8.3). I note that due to the anisotropy of the surface, the Shockley state

Surface	Au(111)	Au(455)
v_F^{2D}, a.u.	0.36	0.18

Table 8.1: Fermi velocities v_F^{2D} of the Shockley surface state in my calculations (see also Fig. 8.4) for the Au(111) and Au(455) surfaces.

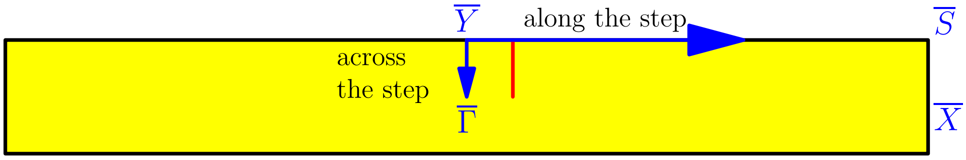

Figure 8.3: The first Brillouin zone of the Au(455) surface. The red line shows the direction along which the electron velocity distribution in Fig. 8.4 is shown.

will have a parabolic dispersion along the step and split into sub-bands across the step (see. Chapter 5). This is the reason of the choice of the path in Fig. 8.3 along which the electron velocity was calculated. I also note that for the sake of convenience, the velocity reported in Fig 8.4 has been computed from the 1D Kronig-Penney fit of the *ab initio* calculated surface state. In table 8.1, I summarize the Fermi velocity of the Shockley state of the Au(111) and Au(455) surfaces. As one can see, the v_F of the Au(455) surface state is twice smaller than v_F of the Au(111) surface state. Assuming that the ASP dispersion follows the same law as it did for the Au(111) surface, $\omega_{ASP} = \alpha v_f^{2D} q$ and has a similar α, it would mean that a single ASP peak with an energy about twice smaller in Au(455) than in the Au(111) surface should be observed.

8.3.4 The ASP dispersion

In Fig. 8.5, I report the dispersion of the ASP across the step of the Au(455) surface along with the ASP dispersion of the Au(111) surface reported in Chapter 7. One can see that dispersion lines practically coincide for $q < 0.125$ Å, while for bigger values of $\mathbf{q}$, the ASP of Au(455) runs just slightly below the ASP of Au(111), contrarily to the expectation made in previous section that it would have a twice smaller energy. These results agree with the experimental results for the Au(788) obtained in Ref. [16] where the upper ASP branch has a dispersion very similar to the one of the Au(111) surface up to the value of $\mathbf{q} \sim 0.2$ Å^{-1}.

In fact, for higher values of $\mathbf{q}$ where it exceeds reciprocal lattice vectors G_0 so that multiples of G_0 can be transferred, the ASP became localized within terraces of Au(788). Thus the smaller ASP energy for $q > 0.125$ Å of Au(455) in my calculations can be the trace of the ASP localization, that should, in principal, become more pronounced for bigger values of $\mathbf{q}$.

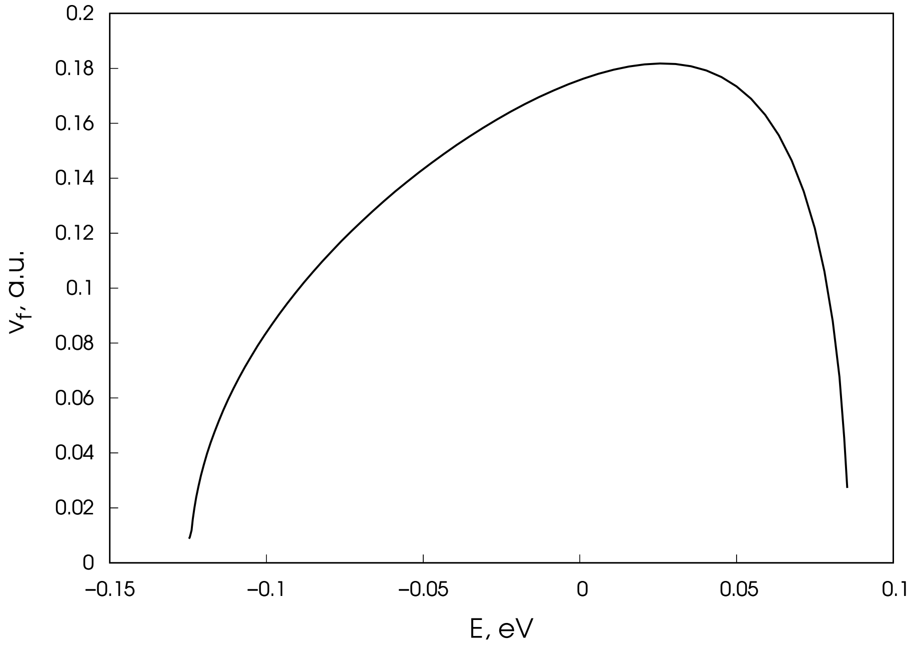

Figure 8.4: Au(455) velocity distribution vs. energy of the surface state calculated without SOC along the direction indicated with the red line in the Fig. 8.3 (across the step).

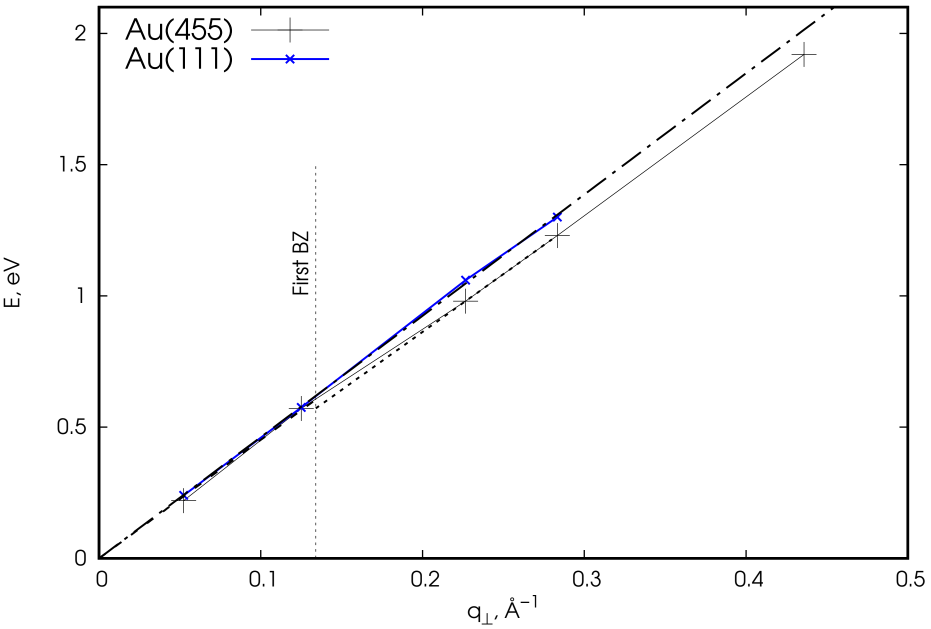

Figure 8.5: The ASP dispersion of the Au(455) (black solid line) and Au(111) (blue solid line) surfaces. The vertical dotted line indicates the edge of the first Brillouin zone of Au(455). The dash-dotted line is the fit of the Au(111) ASP dispersion extrapolate to 0, while the short dashed and dotted lines correspond to the fit of Au(455) ASP dispersion within and beyond the first Brillouin zone respectively.

8.3.5 Discussion

The fact that the dispersion of the ASP of the Au(455) surface reported in Fig. 8.5 does not follow the same law as the ASP dispersion of Au(111), $\omega_{ASP} = \alpha v_f^{2D} q$ (Eq. (3.6)) and has a similar slope despite the twice smaller v_F, suggests that the situation is more complex than it was considered in the model for ASP [11, 17]. Indeed, it was assumed that the surface state is represented by a single parabolic band, which is the case for the Au(111) surface. This assumption does not hold for the Au(455) nor for the Au(788) surface, where the parabolic band is split into subbands due to the step-induced periodic potential. In such a system with subbands there might be two types of excitations: an intrasubband plasmon, similar to the one of the Au(111) surface, that involves only one surface state subband and an intersubband plasmon that involves the transitions from the occupied subband to the next unoccupied subband. As the next subbands have higher values of the electron velocity it will naturally result in a higher plasmon energy than the one suggested by Eq. (3.6). In this case I would expect that that the ASP dispersion will have minigaps at the Brillouin zone borders that would correspond to the minigaps between the surface state subbands. In order to verify this theory additional calculations will be required in order to probe more **q** points around the zone border. Even then it might be obscured due to the finite width of the ASP peaks in the EEL spectrum.

8.4 Conclusions and perspectives

This chapter is devoted to the study of the EEL spectra and ASP of the Au(455) surface and their comparison with the Au(111) surface. I have shown that, as expected, the EEL spectrum of Au(455) largely resembles the EEL spectrum of the Au(111) surface for finite **q** and shows notable differences at vanishing **q**.

The dispersion of the ASP of the Au(455) surface practically coincides with the dispersion of the Au(111) ASP for $q < 0.125$Å and shows signs of confinement for $q > 0.125$ Å. The main result of the present work is the fact that the geometry of the surface turns out to have a significant effect on the ASP dispersion of the Au(455) surface. I suggest that this is due to the nature of the ASP excitation in complex surfaces in which the Shockley state is split into subbands: in such systems intrasubband and intersubband plasmons may coexist. I have shown that for the applications where one is interested in a uniform plasmon propagation velocity one should consider a region of small values of **q** ($q < 0.125$ Å^{-1} for the Au(455) surface), as the surface geometry does not have a significant impact on the ASP dispersion in this region. In other cases however, when one will deal with higher momentum transfer values, a special attention is required, as the ASP may be confined and will not have a linear dispersion. Thus one might have to consider to make a dedicated material design aimed at the optimization of the surface geometry and its properties using *ab initio* methods.

Due to the fact that in the experiments one cannot study the Au(455) surface which undergoes strong reconstruction the study performed in this chapter is mainly academical. Nevertheless, I have shown that indeed, on vicinal surfaces where the Shockley surface state is observed, the ASP can be seen in the EEL spectrum. More importantly, this study has shown the powerfulness of the Liouville-Lanczos approach when it comes to the simulations of large systems that would be unfeasible with any other state-of-the art method. In the future it will be possible not just to perform a full *ab initio* study of the ASP of the Au(788) surface but also to simulate and study EEL spectra of ASP of complex nanostructures, i.e. nanowires on vicinal surfaces. Such calculations will allow to use a first-principles approach to the material design for plasmonic applications, allowing to make more accurate predictions than simplified models before conducting any actual experiments.

General conclusions and perspectives

This thesis has been devoted to the *ab initio* study of plasmons and surface states of gold surfaces and to understand the role of spin-orbit coupling (SOC) and of surface geometry. I used density functional theory (DFT) [40, 41] and a recently developed Liouville-Lanczos approach [21, 22, 23, 24, 25, 26] to time dependent density functional theory (TDDFT) that allows one to compute EEL spectra for periodic systems in a very effective manner, that was generalized to the full relativistic ultrasoft pseudopotential scheme in this work.

I have conducted a thorough study of the surface states and resonances on the three Au(111) vicinal surfaces: Au(322), Au(455) and Au(788). I have shown that despite the challenges introduced due to the surface structure (big unit cell and band structure refolding), the surface state of the vicinal surfaces can be studied using the *ab initio* DFT approach. First, I have discussed in details how the band structure refolds for vicinal surfaces and how the projected bulk band structure (PBS) can be understood. Then I have computed the surface band structures for the Au(322), Au(455) and Au(788) surfaces identifying for each surface the Shockley surface states and surface resonances through the study of the planar averages of the charge density and projections of the surface state wavefunctions onto the atomic orbitals. The latter allowed to unambiguously conclude that all of the identified surface states and resonances are derived from the Shockley state of the flat Au(111) surface. Using the 1D Kronig-Penney model I have fitted the surface state dispersion and compared the fit parameters with those available from previous experimental works, finding a remarkable agreement. Finally I have proposed a way to distinguish between the terrace modulated and average surface modulated state and successfully used the criterion for the surface resonance of Au(322) and Shockley state of Au(455) and Au(788).

In collaboration with Andrea Dal Corso I have made a generalization of the Liouville-Lanczos (LL) approach to TDDFPT to the full relativistic ultrasoft pseudopotential scheme. The LL approach was already superior in terms of performance to the traditional TDDFT approach based on the solution of the Dyson-like equation for susceptibility. The use of ultrasoft pseudopotentials allows to reduce the number of plane waves needed in the calculations and thus to further improve the LL approach performance. These methodological improvements allow to perform very accurate EEL spectra simulations for systems of unprecedented size that in the past were considered unfeasible from the computational point of view.

I have thoroughly studied EEL spectra of bulk Au for different values of transferred momentum with and without SOC. I have re-examined the low energy (<15 eV) EEL spectrum and shown that plasmon signatures in EEL spectra of Au are more complex that previously believed as it contains a peak of the unscreened Drude plasmon. I have then shown that while the SOC does not change EEL spectrum of bulk Au drastically, it does improve the overall agreement with experimental results, in particular with respect to the unscreened Drude plasmon. Finally I have shown that the effect of SOC becomes progressively smaller with increasing value of the transferred momentum and, eventually, the EEL spectrum calculated with SOC practically coincides with the spectrum calculated without SOC.

I have also studied the EEL spectrum of the Au(111) surface and acoustic surface plasmon (ASP) dispersion of Au(111) as well as the role of SOC. I have shown that indeed, the major part of the surface EEL spectrum is derived from the EEL spectrum of bulk. Thus, the inclusion of SOC in the EEL spectrum calculations for the Au(111) surface leads to changes in the spectrum that are similar to the bulk case. I have then studied the ASP dispersion of the Au(111) surface with and without SOC and compared to the previous experimental and *ab initio* results obtained without SOC. I have shown that SOC does not significantly modify the ASP peak, neither its position nor its intensity but, nevertheless, slightly improves the agreement with the experimental results. This finding disproves the hypothesis that neglecting SOC in the past calculations was the reason of the discrepancy between experimental and theoretical results and suggests that another mechanism is responsible for the discrepancy.

I have studied, for the first time, the EEL spectra and ASP of the Au(455) surface. I have shown that for a vanishing value of the transferred momentum the EEL spectrum of Au(455) resembles that of the Au(111) surface, with the notable exception of the conventional surface plasmon that is severely damped for the Au(111) surface in LDA and becomes more pronounced for the Au(455) surface. Finally, I have studied the ASP dispersion of the Au(455) surface. I have shown that for a transferred momentum smaller that 0.125 Å^{-1} the surface geometry has little to no impact on the ASP dispersion, while for bigger values of the transferred momentum the energy of the ASP of Au(455) is smaller than that of the Au(111) surface. I have suggested that it is due to the splitting of the Shockley state into subbands of the Au(455) surface, as in such a system two types of ASP excitation would be possible: an intrasubband plasmon similar to the one of the Au(111) surface that involves an excitation within a single subband, and an intersubbands plasmon that involves transitions between occupied and unoccupied subbands of the surface state.

The perspectives of this PhD work are numerous.

- *Acoustic surface plasmons of the Au(788) surface*

  In the present work I have studied ASP of the Au(455) surface, that was chosen as a compromise between the computational cost of the calculations and expected physical properties. The used method, however, can be readily applied to the more realistic Au(788) surface that would allow a direct comparison with experimental results [16]. Tests on the Au(788) surface have shown that such calculations are feasible.

- *Surface state of complex surfaces*

  In my thesis I have decisively demonstrated that with the use of DFT it is possible to accurately predict and characterize the Shockley surface state on vicinal surfaces of Au(111). The next step would then be a characterization of the surface states of even more complex structures, i.e. nanowires on vicinal surfaces or surfaces with adsorbants that might prove interesting for future plasmonic applications.

- *Material design*

  One of the most challenging part of the design of materials with desired properties is the high cost of the experiments and the long time required to perform numerous experiments, thus theoretical approaches are often used in order to narrow down the list of possible candidates that will be used in the actual experiments. The Liouville-Lanczos approach has the twofold advantage compare to more traditional TDDFT methods in this aspect. On the one hand, due to the high speed of the calculations, it can be used in high-throughput studies, where hundreds or thousands of materials should be studied in a routine manner. On the other hand, due to its unprecedented performance it can be used to study systems that contain hundreds of atoms that were deemed unfeasible before [16].

- *The Liouville-Lanczos approach*

  One of the important achievements of my PhD was an extension of the Liouville-Lanczos approach to the full relativistic ultrasoft pseudopotential scheme. This approach can be considered to be the next-generation method and thus further developments should be done. Namely, TDDFPT+U approach, calculations with hybrid functionals for strongly correlated materials and non-linear response for plasmonic applications beyond the linear order.

Appendix A

EEL spectra convergence

A.1 Pseudopotential.

The most common practice for gold and other noble metals is to use pseudopotential with 11 valence electron - $6s^1$ and semi-core $5d^{10}$ for the case of Au: it provides enough accuracy for many applications and does not require as many computational resources as pseudopotentials that include more core or semi-core electrons in the valence region. In my studies of EEL spectra and ASP I have tested several types of pseudopotentials comparing the results of EEL spectrum calculations for bulk Au with previous full potential linearized augmented plane-wave (FP-LAPW) calculations [52] that have a good agreement with EELS experiments [57]. I have found that the best agreement with FP-LAPW calculations is reached when the optimized norm-conserving pseudopotential [82, 83] with 19 valence electrons configuration $5s^2 5p^6 5d^{10} 6s^1$ is used (see Fig. A.1).

EEL spectra calculated with pseudopotential that contain 11 electrons in the valence region agrees well with FP-LAPW calculations (and with 19 electrons pseudopotential) for E<15eV (see Fig. A.1(b)), while for E>15eV peaks in loss spectrum are blue-shifted by 1-2 eV. I have verified that both LDA and GGA exchange-correlation functional yield the same EEL spectrum if the same lattice constant is used, however for Au theoretical lattice constant obtained with LDA agrees much better than lattice constant obtained with GGA. As my main goal was to study plasmons, specifically acoustic surface plasmons that are found in a low energy part of EEL spectra (E<5 eV) I have decided to use LDA ultrasoft pseudopotential from pslibrary 1.0.0 [84] with 11 electrons in the valence region of the pseudopotential.

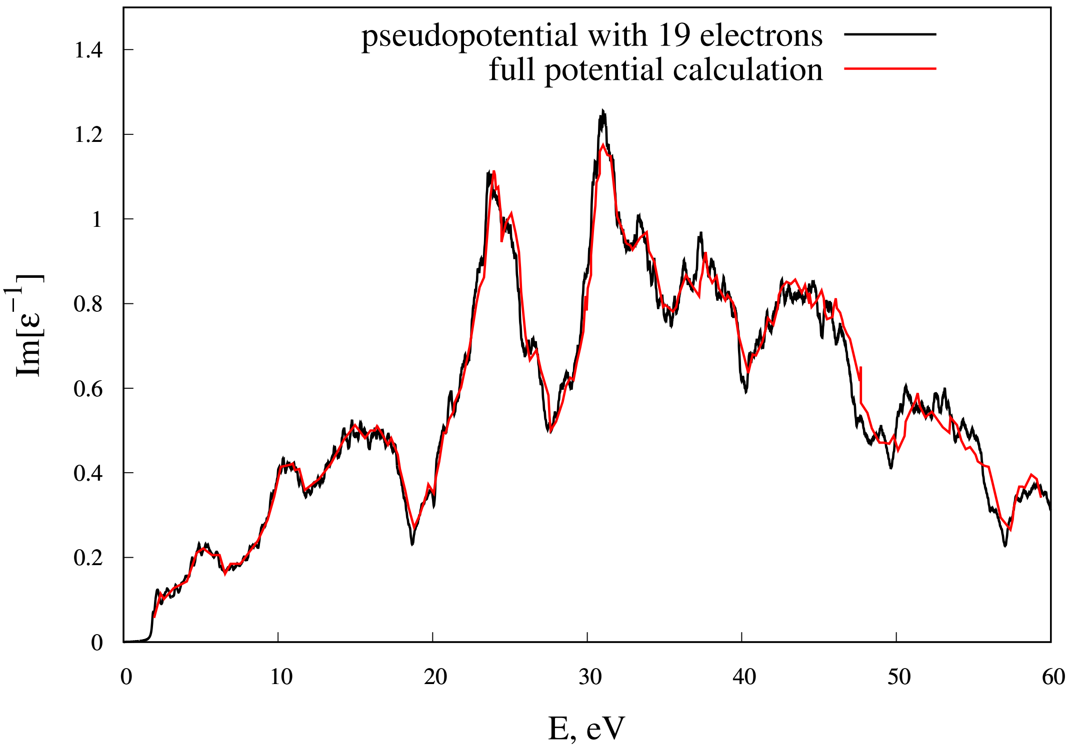

(a)

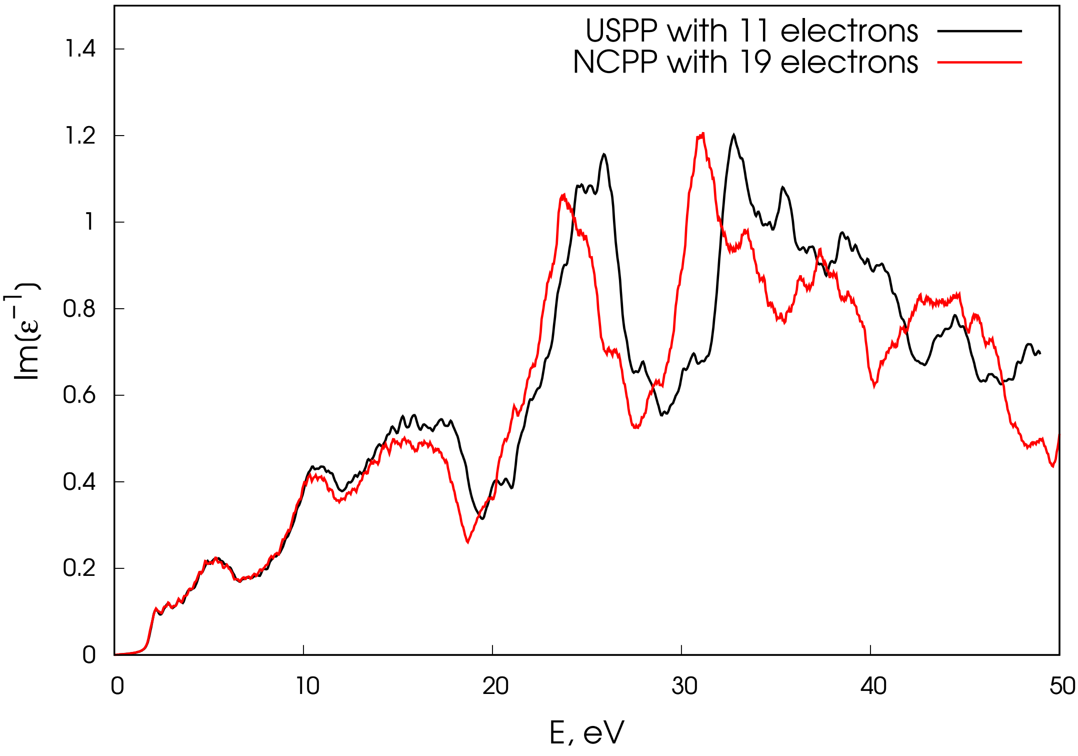

(b)

Figure A.1: Bulk Au EEL spectra computed with (a) the pseudopotential with 19 electrons in the valence region and previous FP-LAPW calculations [52] (b) the pseudopotential with 11 electrons [84] in the valence region that was used in this work and the pseudopotential with 19 electrons in the valence region.

.

A.2 Convergence of the EEL spectrum with respect to the vacuum size

Throughout my whole PhD I have been using a slab-vacuum supercell approach in order to simulate the semi-infinite surface. Thus it is important to use a vacuum of the size that would be enough to decouple the slabs in the neighboring unit cells. In order to determine the adequate vacuum size I have performed a series of tests for the Ag(111) surface and the Au(111) surface. In the Fig. A.2 I report the EEL spectra convergence with respect to the vacuum for the Ag(111) surface at in-plane $q = 0.017\text{Å}^{-1}$. As one can see the full convergence is achieved for value of vacuum between 8 nm and 16 nm that is a quite large value. I note, however that the value of q used is tests was very small, and since long-ranged interactions scale as $\sim q^{-1}$ it implies strong slab-to-slab long-ranged interaction. On the other hand in my work I do not use such a small value of q. In Fig. A.3 I report the Au(111) surface EEL spectra convergence with respect to the vacuum for three values of q: 0.026 Å^{-1}, 0.0523 Å^{-1}, 0.125 Å^{-1}. As one can see, for the smallest $q = 0.026$ Å^{-1} the convergence is indeed slow and a thick vacuum layer is required to decouple neighboring unit cells. However the smaller value of the transferred momentum I have used in my work is $q = 0.0523$ Å^{-1} - already for this value the spectra for the 3 nm and 5 nm of vacuum differ only in the intensity for E<25 eV, while for the bigger $q = 0.125$ Å^{-1} all three spectra are identical. Thus one can conclude that the vacuum of 3 nm and 5 nm that I have used throughout this work is sufficient.

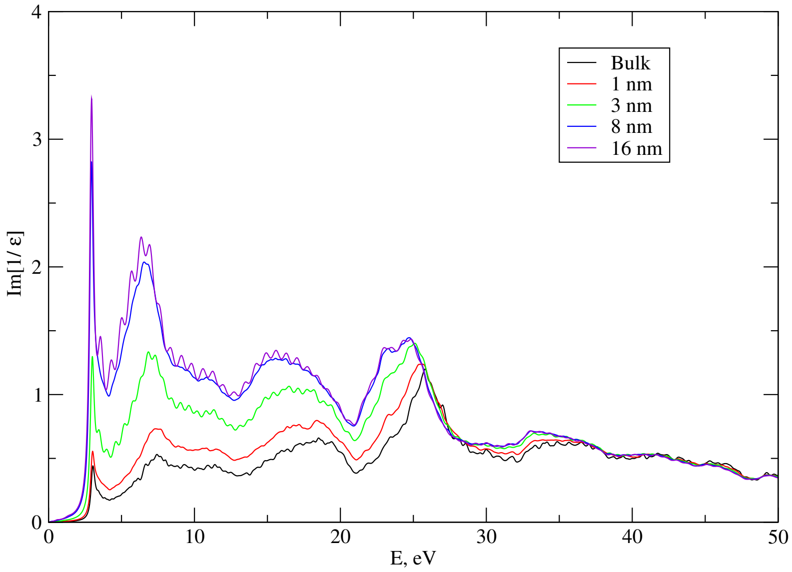

Figure A.2: Ag(111) EEL spectrum calculated using different size of vacuum for the 16 layers slab.

.

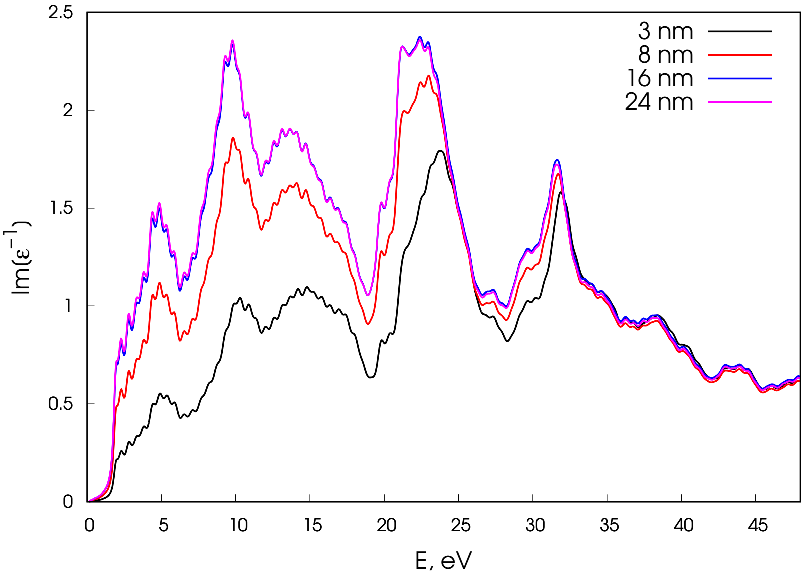

(a)

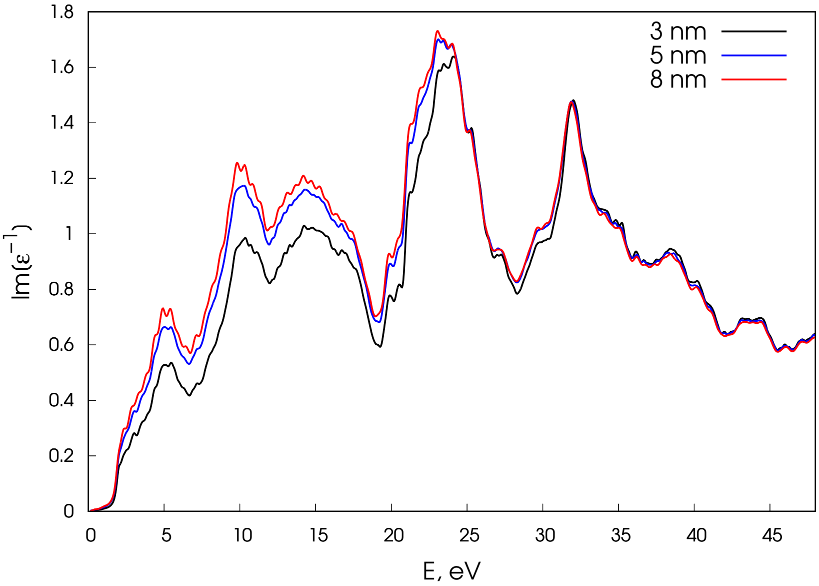

(b)

Figure A.3: Au(111) EEL spectrum calculated using different size of vacuum for the 21 layers slab and using three different values of in-plane q: (a) 0.026 Å^{-1}, (b) 0.0523 Å^{-1},(c) 0.125 Å^{-1}

.

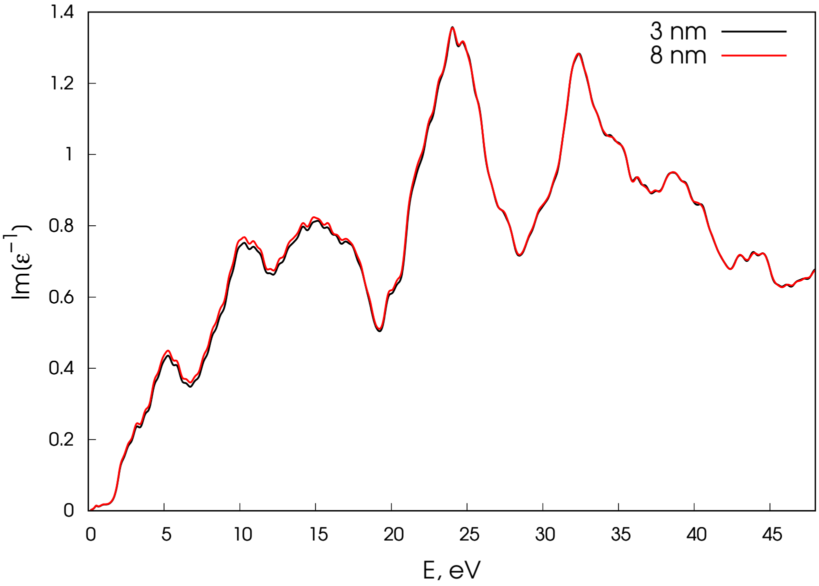

(c)

Figure A.3: (continued) Au(111) EEL spectrum calculated using different size of vacuum for the 21 layers slab and using three different values of in-plane q: (a) 0.026 Å^{-1}, (b) 0.0523 Å^{-1},(c) 0.125 Å^{-1}

.

Bibliography

[1] R.W. Wood. On a remarkable case of uneven distribution of light in a diffraction grating spectrum. The London, Edinburgh, and Dublin Philosophical Magazine and Journal of Science, 4:396–402, 1902.

[2] U. Fano. The theory of anomalous diffraction gratings and of quasi-stationary waves on metallic surfaces (Sommerfeld's waves). J. Opt. Soc. Am., 31:213–222, 1941.

[3] D. Pines and D. Bohm. A collective description of electron interactions: II. collective vs individual particle aspects of the interactions. Phys. Rev., 85:338–353, 1952.

[4] R.H. Ritchie. Plasma losses by fast electrons in thin films. Phys. Rev., 106:874, 1957.

[5] C. J. Powell and J. B. Swan. Origin of the characteristic electron energy losses in aluminum. Phys. Rev., 115:869–875, 1959.

[6] L. Tonks and I. Langmuir. Oscillations in ionized gases. Phys. Rev., 33:195–210, 1929.

[7] E. Runge and E.K.U. Gross. Density-functional theory for time-dependent systems. Phys. Rev. Lett., 52:997, 1984.

[8] E. K. U. Gross and W. Kohn. Local density-functional theory of frequency-dependent linear response. Phys. Rev. Lett., 55:2850, 1985.

[9] F J. García de Abajo. Plasmons go quantum. Nature, 483:417, 2012.

[10] H.-Ch. Weissker and C. Mottet. Optical properties of pure and core-shell noble-metal nanoclusters from TDDFT: The influence of the atomic structure. Phys. Rev. B, 84:165443, 2011.

[11] V. M. Silkin, A. García-Lekue, J. M. Pitarke, E. V. Chulkov, E. Zaremba, and P. M. Echenique. Novel low-energy collective excitation at metal surface. Europhys. Lett., 66:260, 2004.

[12] B. Diaconescu, K. Pohl, L. Vattuone, L. Savio, P. Hofmann, V.M. Silkin, J.M. Pitarke, E.V. Chulkov, P.M. Echenique, D. Farias, and M. Rocca. Low-energy acoustic plasmons. Nature, 448:57, 2007.

[13] L. Vattuone, M. Smerieri, T. Langer, C. Tegenkamp, H. Pfnür, V. M. Silkin, E. V. Chulkov, P. M. Echenique, and M. Rocca. Correlated motion of electrons on the Au(111) surface: Anomalous acoustic surface-plasmon dispersion and single-particle excitations. Phys. Rev. Lett., 110:127405, 2013.

[14] K. Pohl, B. Diaconescu, G. Vercelli, L. Vattuone, V.M. Silkin, E.V. Chulkov, P.M. Echenique, and M. Rocca. Acoustic surface plasmon on Cu(111). European Physics Letters, 90:57006, 2010.

[15] J. Pischel, Em. Welsch, O. Skibbe, and A. Pucci. Acoustic surface plasmon on Cu(111) as an excitation in the mid-infrared range. The Journal of Physical Chemistry C, 117:26964–26968, 2013.

[16] M. Smerieri, L. Vattuone, L. Savio, T. Langer, C. Tegenkamp, H. Pfnür, V. M. Silkin, and M. Rocca. Anisotropic dispersion and partial localization of acoustic surface plasmons on an atomically stepped surface: Au(788). Phys. Rev. Lett., 113:186804, 2014.

[17] J.M. Pitarke, V. U. Nazarov, V.M. Silkin, E.V. Chulkov, E. Zaremba, and P.M. Echenique. Theory of acoustic surface plasmons. Phys. Rev. B, 70:205403, 2004.

[18] V. M. Silkin, J. M. Pitarke, E. V. Chulkov, and P. M. Echenique. Acoustic surface plasmons in the noble metals Cu, Ag, and Au. Phys. Rev. B, 72:115435, 2005.

[19] G. Onida, L. Reining, and A. Rubio. Electronic excitations: Density functional versus many body Green's functions approaches. Rev. Mod. Phys., 74:601, 2002.

[20] S. Botti, A. Schindlmayr, R. D. Sole, and L. Reining. Time-dependent density-functional theory for extended systems. Rep. Prog. Phys., 70:357, 2007.

[21] B. Walker, A. M. Saitta, R. Gebauer, and S. Baroni. Efficient approach to time-dependent density-functional perturbation theory for optical spectroscopy. Phys. Rev. Lett., 96:113001, 2006.

[22] B. Walker and R. Gebauer. Ultrasoft pseudopotentials in time-dependent density-functional theory. J. Chem. Phys., 127:164106, 2007.

[23] O. B. Malcioglu, R. Gebauer, D. Rocca, and S. Baroni. TurboTDDFT - a code for the simulation of molecular spectra using the Liouville-Lanczos approach to time-dependent density-functional perturbation theory. Comput. Phys. Commun., 182:1744, 2011.

[24] D. Rocca, R. Gebauer, Y. Saas, and S. Baroni. Turbo charging time-dependent density-functional theory with Lanczos chains. J. Chem. Phys., 128:154105, 2008.

[25] I. Timrov, N. Vast, R. Gebauer, and S. Baroni. Electron energy loss and inelastic x-ray scattering cross sections from time-dependent density-functional perturbation theory. Phys. Rev. B, 88:064301, 2014.

[26] I. Timrov, N. Vast, R. Gebauer, and S. Baroni. turboEELS-A code for the simulation of the electron energy loss and inelastic x-ray scattering spectra using the Liouville-Lanczos approach to time-dependent density-functional perturbation theory. Computer Physics Communications, 196:460–469, 2015.

[27] S. Baroni, S. de Gironcoli, A. Dal Corso, and P. Giannozzi. Phonons and related crystal properties from density-functional perturbation theory. Rev. Mod. Phys., 73:515, 2001.

[28] E. K. U. Gross, J. F. Dobson, and M. Petersilka. Density Functional Theory of Time-Dependent Phenomena. Topics in Current Chemistry. Springer-Verlag, Berlin, 1996.

[29] T. Gorni, I. Timrov, and S. Baroni. Spin dynamics from time-dependent density functional perturbation theory. The European Physical Journal B, 91:249, 2018.

[30] L. Kleinman. Relativistic norm-conserving pseudopotentials. Phys. Rev. B, 21:2630, 1980.

[31] P. Giannozzi, S. Baroni, N. Bonini, M. Calandra, R. Car, C. Cavazzoni, D. Ceresoli, G.L. Chiarotti, M. Cococcioni, I. Dabo, A. Dal Corso, S. De Gironcoli, S. Fabris, G. Fratesi, R. Gebauer, U. Gerstmann, C. Gougoussis, A. Kokalj, M. Lazzeri, L. Martin-Samos, N. Marzari, F. Mauri, R. Mazzarello, S. Paolini, A. Pasquarello, L. Paulatto, C. Sbraccia, S. Scandolo, G. Sclauzero, A.P. Seitsonen, A. Smogunov, P. Umari, and R.M. Wentzcovitch. QUANTUM ESPRESSO: A modular and open-source software project for quantum simulations of materials. J. Phys.: Condens. Matter, 21:395502, 2009.

[32] P. Giannozzi, O. Andreussi, T. Brumme, O. Bunau, M. Buongiorno Nardelli, M. Calandra, R. Car, C. Cavazzoni, D. Ceresoli, M. Cococcioni, N. Colonna, I. Carnimeo, A. Dal Corso, S. de Gironcoli, P. Delugas, R. A. DiStasio Jr.and A. Ferretti, A. Floris, G. Fratesi, G. Fugallo, R. Gebauer, U. Gerstmann, F. Giustino, T. Gorni, J. Jia, M. Kawamura, H.-Y. Ko, A. Kokalj, E. Küçükbenli, M. Lazzeri, M. Marsili, N. Marzari, F. Mauri, N. L. Nguyen, H.-V. Nguyen, A. Otero de-la Roza, L. Paulatto, S. Poncé, D. Rocca, R. Sabatini, B. Santra, M. Schlipf, A. P. Seitsonen, A. Smogunov, I. Timrov, T. Thonhauser, P. Umari, N. Vast, X. Wu, and S. Baroni. Advanced capabilities for materials modelling with QUANTUM ESPRESSO. J. Phys.: Condens. Matter, 29:465901, 2017.

[33] S. LaShell, B. A. McDougall, and E. Jensen. Spin splitting of an Au(111) surface state band observed with angle resolved photoelectron spectroscopy. Phys. Rev. Lett., 77:3419–3422, 1996.

[34] R. Mazzarello, A. Dal Corso, and E. Tosatti. Spin-orbit modifications and splittings of deep surface states on clean Au(111). Surface Science, 602:893 – 905, 2008.

[35] J. E. Ortega, A. Mugarza, V. Repain, S. Rousset, V. Pérez-Dieste, and A. Mascaraque. One-dimensional versus two-dimensional surface states on stepped Au(111). Phys. Rev. B, 65:165413, 2002.

[36] U. Harten, A. M. Lahee, J. Peter Toennies, and Ch. Wöll. Observation of a soliton reconstruction of Au(111) by high-resolution helium-atom diffraction. Phys. Rev. Lett., 54:2619, 1985.

[37] N. Takeuchi, C. T. Chan, and K. M. Ho. Au(111): A theoretical study of the surface reconstruction and the surface electronic structure. Phys. Rev. B, 43:13899, 1991.

[38] H. Ibach. Physics of Surfaces and Interfaces. Springer Berlin Heidelberg, 2006.

[39] H. Lüth. Surfaces and interfaces of solid materials. Number 3 in Springer Study Edition. Springer, 1995.

[40] P. Hohenberg and W. Kohn. Inhomogeneous electron gas. Phys. Rev., 136:B864, 1964.

[41] W. Kohn and L.J. Sham. Self-consistent equations including exchange and correlation effects. Phys. Rev., 140:A1133, 1965.

[42] A. Mugarza and J.E. Ortega. Electronic states at vicinal surfaces. Journal of Physics: Condensed Matter, 15:S3281, 2003.

[43] G. Prévot, Y. Girard, V. Repain, S. Rousset, A. Coati, Y. Garreau, J. Paul, N. Mammen, and S. Narasimhan. Elastic displacements and step interactions on metallic surfaces: Grazing-incidence x-ray diffraction and ab initio study of Au(332). Phys. Rev. B, 81:075415, 2010.

[44] S. Rousset, V. Repain, G. Baudot, Y. Garreau, and J. Lecoeur. Self-ordering of Au(111) vicinal surfaces and application to nanostructure organized growth. Journal of Physics: Condensed Matter, 15:S3363, 2003.

[45] V. Repain, J. M. Berroir, B. Croset, S. Rousset, Y. Garreau, V. H. Etgens, and J. Lecoeur. Interplay between atomic and mesoscopic order on gold vicinal surfaces. Phys. Rev. Lett., 84:5367–5370, 2000.

[46] A. Mugarza, A. Mascaraque, V. Pérez-Dieste, V. Repain, S. Rousset, F. J. García de Abajo, and J. E. Ortega. Electron confinement in surface states on a stepped gold surface revealed by angle-resolved photoemission. Phys. Rev. Lett., 87:107601, 2001.

[47] L. C. Davis, M. P. Everson, R. C. Jaklevic, and Weidian Shen. Theory of the local density of surface states on a metal: Comparison with scanning tunneling spectroscopy of a Au(111) surface. Phys. Rev. B, 43:3821–3830, 1991.

[48] J E Ortega, M Ruiz-Osés, J Cordón, A Mugarza, J Kuntze, and F Schiller. One-dimensional versus two-dimensional electronic states in vicinal surfaces. New Journal of Physics, 7(1):101, 2005.

[49] R. F. Egerton. Electron Energy-Loss Spectroscopy in the Electron Microscope. Plenum, New York and London, 2nd edition, 1996.

[50] N. W. Ashcroft and N. D. Mermin. Solid State Physics. Holt-Saunders, Philadelphia, 1976.

[51] C.B. Wilson. A phenomenological theory of the characteristic energy losses of fast electrons in metals. Proceedings of the Physical Society, 76:481, 1960.

[52] A. Alkauskas, S.D. Schneider, C. Hébert, S. Sagmeister, and C. Draxl. Dynamic structure factors of Cu, Ag, and Au: Comparative study from first principles. Phys. Rev. B, 88:195124, 2013.

[53] J.M. Pitarke, V.M. Silkin, E.V. Chulkov, and P.M. Echenique. Theory of surface plasmons and surface-plasmon polaritons. Rep. Prog. Phys., 70:1, 2007.

[54] F. Stern. Polarizability of a two-dimensional electron gas. Phys. Rev. Lett., 18:546–548, 1967.

[55] I.G. Gurtubay, J.M. Pitarke, I. Campillo, and A. Rubio. Dynamic structure factor of gold. Computational Materials Science, 22:123 – 128, 2001.

[56] E.D. Palik. Handbook of Optical Constants of Solids, volume 4. Academic Press, 1998.

[57] W. Werner, K. Glantschnig, and C. Ambrosch-Draxl. Optical constants and inelastic electron-scattering data for 17 elemental metals. J. Phys. Chem. Ref. Data, 38:1013, 2009.

[58] J. Yan, K.W. Jacobsen, and K.S. Thygesen. Conventional and acoustic surface plasmons on noble metal surfaces: A time-dependent density functional theory study. Phys. Rev. B, 86:241404(R), 2012.

[59] A. Marini, R. Del Sole, and G. Onida. First-principles calculation of the plasmon resonance and of the reflectance spectrum of silver in the GW approximation. Phys. Rev. B, 66:115101, 2002.

[60] A. Tararan, S. di Sabatino, M. Gatti, T. Taniguchi, K. Watanabe, L. Reining, L.H.G. Tizei, M. Kociak, and A. Zobelli. Optical gap and optically active intragap defects in cubic BN. Physical Review B, 982121, 2018.

[61] S. J. Park and R. E. Palmer. Acoustic plasmon on the Au(111) surface. Phys. Rev. Lett., 105:016801, 2010.

[62] V. M. Silkin, J. M. Pitarke, E. V. Chulkov, B. Diaconescu, K. Pohl, L. Vattuone, L. Savio, Ph. Hofmann, D. Farías, M. Rocca, and P. M. Echenique. Band structure effects on the Be(0001) acoustic surface plasmon energy dispersion. Physica Status Solidi (a), 205:1307–1311, 2008.

[63] A. Liebsch. Electronic Excitations at Metal Surfaces. Physics of Solids and Liquids. Springer, 1997.

[64] B. N. J. Persson and E. Zaremba. Electron-hole pair production at metal surfaces. Phys. Rev. B, 31:1863–1872, 1985.

[65] O. Motornyi, M. Raynaud, A. Dal Corso, and N. Vast. Simulation of electron energy loss spectra with the turboEELS and thermo_pw codes. J. Phys.: Conf. Ser., 1136:012008, 2018.

[66] A. Dal Corso, A. Pasquarello, and A. Baldereschi. Density-functional perturbation theory for lattice dynamics with ultrasoft pseudopotentials. Phys. Rev. B, 56:R11369–R11372, 1997.

[67] A. Dal Corso. Density-functional perturbation theory with ultrasoft pseudopotentials. Phys. Rev. B, 64:235118, 2001.

[68] J. Tóbik and A. Dal Corso. Electric fields with ultrasoft pseudo-potentials: Applications to benzene and anthracene. The Journal of Chemical Physics, 120:9934–9941, 2004.

[69] A. Dal Corso. Spin-orbit coupling with ultrasoft pseudopotentials: Application to Au and Pt. Phys. Rev. B, 71:115106, 2005.

[70] A. Dal Corso. Density functional perturbation theory for lattice dynamics with fully relativistic ultrasoft pseudopotentials: Application to fcc-Pt and fcc-Au. Phys. Rev. B, 76:054308, 2007.

[71] D. Vanderbilt. Soft self-consistent pseudopotentials in a generalized eigenvalue formalism. Phys. Rev. B, 41:7892, 1990.

[72] L. Kleinman and D.M. Bylander. Efficacious form for model pseudopotentials. Phys. Rev. Lett., 48:1425, 1982.

[73] X. Qian, J. Li, X. Lin, and S. Yip. Time-dependent density functional theory with ultrasoft pseudopotentials: Real-time electron propagation across a molecular junction. Phys. Rev. B, 73:035408, 2006.

[74] I. Timrov, M. Markov, T. Gorni, M. Raynaud, O. Motornyi, R. Gebauer, S. Baroni, and N. Vast. *Ab initio* study of electron energy loss spectra of bulk bismuth up to 100 eV. Phys. Rev. B, 95:094301, 2017.

[75] B. Himmetoglu, A. Floris, S. Gironcoli, and M. Cococcioni. Hubbard-corrected DFT energy functionals: The LDA+U description of correlated systems. International Journal of Quantum Chemistry, 114:14–49, 2014.

[76] The code can be obtained from `https://dalcorso.github.io/thermo_pw/`.

[77] P.V.C. Medeiros, S. Stafström, and J. Björk. Effects of extrinsic and intrinsic perturbations on the electronic structure of graphene: Retaining an effective primitive cell band structure by band unfolding. Phys. Rev. B, 89:041407, 2014.

[78] Paulo V. C. Medeiros, Stepan S. Tsirkin, Sven Stafström, and Jonas Björk. Unfolding spinor wave functions and expectation values of general operators: Introducing the unfolding-density operator. Phys. Rev. B, 91:041116, 2015.

[79] K. Glantschnig and C. Ambrosch-Draxl. Relativistic effects on the linear optical properties of Au, Pt, Pb and W. New J. Phys., 12:103048, 2010.

[80] L. Vattuone, G. Vercelli, M. Smerieri, L. Savio, and M. Rocca. Acoustic surface plasmon dispersion on nanostructured Cu(111). Plasmonics, 7:323, 2012.

[81] J. Osma, I. Sarría, E. V. Chulkov, J. M. Pitarke, and P. M. Echenique. Role of the intrinsic surface state in the decay of image states at a metal surface. Phys. Rev. B, 59:10591–10598, 1999.

[82] M. Schlipf and F.r Gygi. Optimization algorithm for the generation of ONCV pseudopotentials. Computer Physics Communications, 196:36 – 44, 2015.

[83] P. Scherpelz, M. Govoni, I. Hamada, and G. Galli. Implementation and validation of fully relativistic GW calculations: Spin˘orbit coupling in molecules, nanocrystals, and solids. Journal of Chemical Theory and Computation, 12:3523–3544, 2016.

[84] A. Dal Corso. Pseudopotentials periodic table: From H to Pu. Computational Materials Science, 95:337 – 350, 2014.

université PARIS-SACLAY

ÉCOLE DOCTORALE
INTERFACES
Approches Interdisciplinaires :
Fondements, Applications et Innovation

Titre : Etude *ab initio* des états électroniques de surface et des plasmons de l'or: rôle du couplage spin-orbite et de la géométrie de surface.

Mots clés : l'or, TDDFPT, EELS, couplage spin-orbite, plasmon acoustique de surface, surface vicinale

Résumé : Cette thèse de doctorat est dédiée à l'étude, avec des méthodes de calcul *ab initio*, des plasmons de surface et des états de surface de surfaces d'or, plates ou vicinales, par la simulation numérique de spectres de perte d'énergie électronique (EEL) au moyen de la théorie de la fonctionnelle de la densité (DFT) et de la théorie de perturbation de la fonctionnelle de la densité dépendant du temps (TDDFPT). L'influence du couplage spin-orbite (CSO) et celle de la géométrie de la surface ont été étudiées. J'ai réalisé des développements méthodologiques pour la TDDFPT avec CSO couplé à l'emploi de pseudopotentiels ultradoux, qui ont permis l'implémentation pratique de cette approche dans les algorithmes de Liouville-Lanczos et de Sternheimer. J'ai utilisé ces approches qui m'ont permis de traiter des systèmes à plusieurs centaines d'atomes. J'ai montré que l'inclusion du CSO a un effet petit mais détectable sur le spectre EEL et le pic de plasmon, donnant un meilleur accord avec l'expérience à $\mathbf{q} = \mathbf{0}$. J'ai trouvé que la dispersion du plasmon acoustique de surface (PAS) de Au (111) est légèrement modifiée par le CSO. Pour étudier les effets de géométrie, j'ai étudié les surfaces vicinales (322), (455) et (788) de l'or. J'ai mené l'étude théorique des états électroniques de surface, et analysé l'évolution de l'état de surface de Shockley entre la surface plate Au(111) et les surfaces ayant des marches dont les terrasses avaient différentes largeurs. J'ai montré la transition d'un état de surface résonant pour Au(322) à un état localisé pour Au(455) et pour Au(788), ainsi que le passage d'un état 2D étendu à travers la marche pour Au(322) à un état quasi-1D confiné dans la terrasse de la marche pour Au(455) et pour Au(788). Ces résultats sont en accord avec l'expérience, et avec ceux du modèle de potentiel périodique de Kronig-Penney. J'ai calculé le spectre EELS pour la surface d'or (455) et identifié la signature du plasmon acoustique de surface. J'ai montré que, pour un moment transféré perpendiculaire à la marche de la surface, la dispersion du PAS n'est pas modifiée par rapport à celle du PAS de la surface plate Au(111) pour $q < 0.125\ \mathring{A}^{-1}$. Cependant, pour $q > 0.125\ \mathring{A}^{-1}$le pic du PAS a une énergie plus basse que celle du PAS de Au(111), montrant la signature du confinement du PAS.

Title : *Ab initio* study of electronic surface states and plasmons of gold: role of the spin-orbit coupling and surface geometry.

Keywords : gold, TDDFPT, EELS, spin-orbit coupling, acoustic surface plasmon, vicinal surface

Abstract : The PhD thesis is devoted to the *ab initio* study of surface plasmons and surface states of flat and vicinal surfaces of Au through the simulation of electron energy loss (EEL) spectra by means of the density functional theory (DFT) and the time-dependent density functional perturbation theory (TDDFPT). The influence of the spin-orbit coupling (SOC) and of the surface geometry has been investigated. I have made methodological developments for TDDFPT with SOC in the ultrasoft pseudopotential scheme that led to the implementation of SOC in the Liouville-Lanczos and Sternheimer approaches that allowed me to model systems with hundreds of atoms. I have demonstrated that SOC has a small but noticeable effect on the Au EEL spectrum and plasmon peak, bringing the calculated spectrum into a better agreement with experimental results at $\mathbf{q} = 0$. I have observed that the dispersion of the acoustic surface plasmon (ASP) on the Au(111) surface is slightly modified by SOC.To investigate the effect of geometry I have studied the vicinal (322), (455) and (788) surfaces of Au. In particular I have performed the theoretical study of the surface states, analyzing the evolution of the Shockley surface state from the flat Au(111) surface towards the surfaces with terraces of different width. I have shown the surface-resonance to surface-state transition and the average-surface-modulated to the terrace-modulated state transition from (322) to (455) and to (788) surfaces, as well as the transition from the extended 2D state to the quasi-1D state confined within the terrace. These results are in agreement with experiments and results obtained with the Kronig-Penney periodic potential model. I have performed the EEL spectrum calculations for the Au(455) surface and identified signatures of the ASP in these spectra, showing that for the case of the transferred electron wavevector momentum perpendicular to the step, the ASP dispersion is not changed with respect to the ASP dispersion of the Au(111) surface for $q < 0.125\ \mathring{A}^{-1}$. For $q > 0.125\ \mathring{A}^{-1}$, however, the ASP peak has a lower energy compared to the ASP peak of the Au(111) surface, showing signs of the ASP confinement.

Université Paris-Saclay
Espace Technologique / Immeuble Discovery
Route de l'Orme aux Merisiers RD 128 / 91190 Saint-Aubin, France